

Refining the transit timing and photometric analysis of TRAPPIST-1: Masses, radii, densities, dynamics, and ephemerides.

E. Agol,^{1*} K. Barkaoui,^{6,18} Z. Benkhaldoun,¹⁸ E. Bolmont,² A. Burgasser,³ A. Burdanov,⁴ S. Carey,⁵ L. Delrez,^{6,7,2} B.-O. Demory,⁸ J. de Wit,⁴ C. Dorn,¹⁶ E. Ducrot,⁶ D. Fabrycky,⁹ D. Foreman-Mackey,¹⁷ M. Gillon,⁶ S. L. Grimm,⁸ D. M. Hernandez,¹⁰ J. Ingalls,⁵ E. Jehin,⁷ Z. Langford,¹ J. Leconte,¹¹ S. M. Lederer,¹² R. Malhotra,¹³ V. Meadows,¹ B. M. Morris,⁸ F. J. Pozuelos,^{6,7} D. Queloz,¹⁴ S. N. Raymond,¹¹ F. Selsis,¹¹ M. Sestovic,⁸ A. H.M.J. Triaud,¹⁵ M. Turbet,² and V. Van Grootel⁷

¹Astronomy Department and Virtual Planetary Laboratory, University of Washington, Seattle, WA 98195 USA

²Observatoire de Genève, Université de Genève, 51 Chemin des Maillettes, CH-1290 Sauverny, Switzerland

³Center for Astrophysics and Space Science, University of California San Diego, La Jolla, CA, 92093, USA

⁴Department of Earth, Atmospheric and Planetary Science, Massachusetts Institute of Technology, 77 Massachusetts Avenue, Cambridge, MA 02139, USA

⁵IPAC, California Institute of Technology, 1200 E California Boulevard, Mail Code 314-6, Pasadena, California 91125, USA

⁶Astrobiology Research Unit, Université de Liège, Allée du 6 Août 19C, B-4000 Liège, Belgium

⁷Space Sciences, Technologies and Astrophysics Research (STAR) Institute, Université de Liège, Allée du 6 Août 19C, B-4000 Liège, Belgium

⁸Center for Space and Habitability, University of Bern, Gesellschaftsstrasse 6, CH-3012, Bern, Switzerland

⁹Department of Astronomy & Astrophysics, University of Chicago, 5640 S. Ellis Ave., Chicago, IL 60637 USA

¹⁰Harvard-Smithsonian Center for Astrophysics, 60 Garden St., MS 51, Cambridge, MA 02138, USA

¹¹Laboratoire d'astrophysique de Bordeaux, Univ. Bordeaux, CNRS, B18N, Allée Geoffroy Saint-Hilaire, F-33615 Pessac, France

¹²NASA Johnson Space Center, 2101 NASA Pkwy., Houston TX, 77058, USA

¹³Lunar and Planetary Laboratory, The University of Arizona, Tucson, AZ 85721 USA

¹⁴Cavendish Laboratory, JJ Thomson Avenue, Cambridge, CB3 0H3, UK

¹⁵School of Physics & Astronomy, University of Birmingham, Edgbaston, Birmingham B15 2TT, UK

¹⁶University of Zurich, Institute of Computational Sciences, Winterthurerstrasse 190, CH-8057, Zurich, Switzerland

¹⁷Center for Computational Astrophysics, Flatiron Institute, Simons Foundation, 162 5th Ave., New York, NY 10010, USA

¹⁸Oukaimeden Observatory, High Energy Physics and Astrophysics Laboratory, Cadi Ayyad University, Marrakech, Morocco

Accepted XXX. Received YYY; in original form ZZZ

ABSTRACT

We have collected transit times for the TRAPPIST-1 system with the Spitzer space telescope over three years. We add to these ground-based, HST and K2 transit time measurements, and revisit a transit-timing N-body dynamical analysis of the seven-planet system using our complete set of times. From the transit timing analysis, we refine the mass ratios of the planets to the star. We next carry out a photodynamical analysis of the Spitzer light curves to derive the density of the host star and the planet densities. We find that all seven planets' densities may be described with a single rocky mass-radius relation which is depleted in iron relative to Earth, with Fe 17 wt% versus 32 wt% for Earth, and otherwise Earth-like in composition. Alternatively, the planets may have an Earth-like composition, but with volatile enhancement, such as an surface water layer or a core-free structure with oxidized iron in the mantle. We measure planet masses to a precision of 3-5%, equivalent to a radial-velocity (RV) precision of 2.5 cm/sec, or two orders of magnitude more precise than current RV capabilities. We find the eccentricities of the planets are very small; the orbits are extremely coplanar; and the system is stable on Myr timescales. We find evidence of infrequent timing outliers; however, additional planets cannot explain these, which we attribute to systematic errors using a robust likelihood function. We forecast JWST timing observations, and speculate on possible implications of the planet densities for the formation, migration and evolution of the planet system.

Key words: infrared: planetary systems – planets and satellites: terrestrial planets – planets and satellites: compositions – planets and satellites: fundamental parameters

CONTENTS

- 1 Introduction
- 2 New TRAPPIST-1 observations
 - 2.1 Spitzer Observations
 - 2.2 Ground-based observations
 - 2.3 K2 and HST observations
 - 2.4 Transit time measurements and analysis
- 3 Excess of outliers and robust likelihood model
- 4 Transit-timing analysis
 - 4.1 N-body integration
 - 4.2 Uncertainty analysis
 - 4.3 Prior
 - 4.4 Markov chain sampler
 - 4.5 Results
 - 4.6 Independent N-body TTV analysis
- 5 Photodynamical analysis
 - 5.1 Mutual inclinations and stellar density
- 6 Planet densities and mass-radius relation
- 7 Stellar parameters
- 8 Planet detection
 - 8.1 Search for an eighth planet
- 9 Interior compositions
 - 9.1 Initial analysis of planet densities across the system
 - 9.2 Range of possible interior compositions and volatile contents
- 10 Discussion
 - 10.1 Timing uncertainties
 - 10.2 Planet masses and radii
 - 10.3 Comparison with radial velocities
 - 10.4 Possible systematic errors
 - 10.5 Planetary dynamics
 - 10.6 Forecasts for JWST
 - 10.7 Stellar parameters
- 11 Conclusions
 - 11.1 Expectations for the compositions of the TRAPPIST-1 planets from formation scenarios
 - 11.2 Future work
- A Approximate Hessian matrix
- B Tables

1 INTRODUCTION

The TRAPPIST-1 planetary system took the exoplanet community by surprise thanks to the high multiplicity of small transiting planets orbiting a very-low-mass star ($\sim 0.09M_{\odot}$; Gillon et al. 2016, 2017; Luger et al. 2017a; Van Grootel et al. 2018). The unexpected nature stems from the fact that this system was found through a survey of only 50 nearby ultracool dwarf stars (Jehin et al. 2011; Gillon et al. 2013), suggesting either a high-frequency of such systems around the latest of the M-dwarfs (He et al. 2016), or perhaps this discovery was fortuitous (Sestovic & Demory 2020; Sagar et al. 2019). The proximity of the host star (~ 12 pc) makes it brighter in the infrared ($K = 10.3$) than most ultracool dwarfs. Its small size ($\sim 0.12R_{\odot}$) means that its planets' masses and radii are large relative to those of the star, which enables precise characterization of the planets' properties. The system provides the first opportunity for a detailed study of potentially rocky, Earth-sized exoplanets with incident fluxes similar to the terrestrial planets in our Solar System. As such, it has galvanized the exoplanet community to study this system in detail, both observationally and theoretically, and has fueled hopes that atmospheric signatures (or even biosignatures) might be detected with the James Webb Space Telescope (Barstow & Irwin 2016; Morley et al. 2017; Batalha et al. 2018; Krissansen-Totton et al. 2018; Wunderlich et al. 2019; Fauchez et al. 2019; Lustig-Yaeger et al. 2019).

More conservatively, the system provides a potential laboratory for comparative planetology of terrestrial planets, and may provide insight and constraints on the formation and evolution of terrestrial planets around the lowest-mass stars. In particular, transiting multi-planet systems afford an opportunity to constrain the interior compositions of exoplanets. Sizes from transit depths combined with masses from transit-timing variations yield the densities of the planets (e.g. Agol & Fabrycky 2017). In the case of rocky planets with a thin atmosphere, the bulk density can constrain the core-mass fraction and/or Mg/Fe mass-ratio (Valencia et al. 2007), although for any given planet there is still a degeneracy between a larger core-mass fraction and a volatile envelope (Dorn et al. 2018). In a multi-planet system, the bulk density as a function of planet orbital distance may be used to partly break the compositional degeneracy by assuming a common refractory composition and a water composition which increases with orbital distance (Unterborn et al. 2018).

The TRAPPIST-1 system was found with a ground-based pilot survey using a 60-cm telescope, revealing two short-period transiting planets, and two additional orphan transits (Gillon et al. 2016; Burdanov et al. 2018). Subsequent study of the system revealed several additional orphan transits, leading to an incomplete picture of the number of planets and the architecture of the system. A 20-day observation run with Spitzer resolved the confusion, revealing the periods of six of the seven transiting planets (Gillon et al. 2017), but only a single transit observed of the outermost planet left its orbit in question. A subsequent observation campaign of the system with the K2 spacecraft included four additional transits of the outer planet, identifying its period, and reveals a series of generalized three-body Laplace relations (GLR)¹ between adjacent triplets of planets (Luger et al. 2017a). Additional observations with Spitzer continued to monitor the transit times of the seven planets at higher precision than afforded by ground-based observations. An initial

analysis of the Spitzer data to determine planetary radii and masses was presented in Delrez et al. (2018b) and Grimm et al. (2018). In total, Spitzer observed TRAPPIST-1 for more than 1000hrs, and the resulting time-series photometry includes 188 transits (Ducrot et al. 2020).

Although the planets in the TRAPPIST-1 system have short orbital periods, ranging from 1.5 to 19 days, the dynamical interactions accumulate gradually with time, which requires longer-timescale monitoring to accurately constrain the orbital model. The GLR also cause adjacent pairs of planets to reside near mean-motion resonances, for which $jP_i^{-1} \approx kP_{i+1}^{-1}$ for integers j and k for the i th and $i + 1$ th planets. This proximity causes a resonant timescale given by

$$P_{TTV} = \frac{k - j}{jP_i^{-1} - kP_{i+1}^{-1}}. \quad (1)$$

The period of the resonant terms for each of these pairs of planets is $P_{TTV} \approx 487 \pm 24$ days (ranging from 453 to 519 days for each pair). This timescale has two consequences for measuring the masses of the planets from transit-timing variations: 1) the transit times for each planet need to be sampled on this timescale, preferable covering two cycles so that the amplitude and phase of the cycles may be distinguished from the planets' orbital periods; 2) this resonant period also sets the timescale for the amplitude variability of "chopping" (short-timescale transit-timing variations), which can help to break a degeneracy between mass and eccentricity for the resonant terms (Lithwick et al. 2012; Deck & Agol 2015). As a consequence, we expect the measurements of the masses of the system to require sampling on a timescale of $t_{min} \approx 2P_{TTV} \approx 2.7$ years. Consequently, the current paper is the first with a survey time, t_{survey} , such that $t_{survey} > t_{min}$ for the TRAPPIST-1 system.

Prior studies used the data available at the time, with $t_{survey} < t_{min}$, causing ample degeneracy in the dynamical model, and hence larger uncertainties in the masses of the planets (Gillon et al. 2017; Grimm et al. 2018). Even so, these papers were groundbreaking as they enable the first density determinations of temperate, Earth-sized planets exterior to the Solar System. Both papers indicated densities for the planets which are lower than the value expected for an Earth-like composition (with the exception of planet e), indicating that these planets might have a significant volatile content. However, these conclusions were subject to significant uncertainty in the planet masses, making the determination of the compositions less definitive as the uncertainties were still consistent with rocky bodies at the $1 - 2\sigma$ level. In addition, the masses of all of the planets are highly correlated due to the fact that the dynamical state of all of the planets needs to be solved together, so model comparisons with individual planets are not independent.

In this paper we revisit a transit-timing and photometric analysis with the completed Spitzer program using the more extensive transit dataset we now have in hand. The goal of this program is to provide a more precise understanding of the masses, radii, and densities of the planets. These measurements may be used for planetary science with the extrasolar planets in the TRAPPIST-1 system, whose similarity to the sizes, masses and effective insolation range of the terrestrial planets in our Solar System is the closest match known. In addition, we refine the dynamical state of the system, revisiting some of the questions explored in Grimm et al. (2018). Our final goal is to prepare for upcoming observations with the James Webb Space Telescope (JWST). More precise constraints on the parameters of the planets will not only improve the precision with which we can schedule observations, but also provide the best possible predictions of potential environmental characteristics that could

¹ This refers to the condition $pP_1^{-1} - (p + q)P_2^{-1} + qP_3^{-1} \approx 0$, which is a generalization of the Laplace resonance with $p = 1$ and $q = 2$ (Papaloizou 2014).

be discriminated observationally. This work will therefore help to optimize both the acquisition and interpretation of observations of the TRAPPIST-1 system with JWST.

In §2 we summarize the observational data which are analyzed in this paper. In §3 we discuss the nature of transit timing outliers, and the robust likelihood function we use for characterizing the system. This is followed by a description of our N-body transit-timing analysis in §4. With the improved N-body model, we revisit the photometric fit to the Spitzer data, providing a photodynamical model in §5. The results of these two analyses are combined to obtain the planet bulk properties in §6. In §7 we derive revised parameters for the host star. In §8 we search for an eighth planet with transit-timing. In §9 we interpret the mass-radius measurements for the planets in terms of interior and atmospheric structure models. Discussion and conclusions are given in §10 and 11.

2 NEW TRAPPIST-1 OBSERVATIONS

Since the work described in [Grimm et al. \(2018\)](#) based on 284 transits, we have added an additional 163 transit times from a combination of Spitzer (§2.1) and ground-based observations (§2.2). Based on preliminary transit-timing fits, we find evidence for outliers amongst the measured times (§3), which we account for with a robust likelihood model. Each transit time is measured as a Barycentric Julian Date (BJD), correcting for the location of the Earth/spacecraft relative to the Solar System barycenter ([Eastman et al. 2010](#)).

2.1 Spitzer Observations

The dataset used in this work includes the entire photometry database of TRAPPIST-1 observations by Spitzer/IRAC since the discovery of its planetary system. This represents all time series observations gathered within the DDT programs 12126 (PI: M. Gillon), 13175 (PI: L. Delrez) and 14223 (PI: E. Agol). This gives a total of 188 transits observed from Feb 2016 to Oct 2019 and includes 64, 47, 23, 18, 16, 13, and 7 transits of planets b, c, d, e, f, g, and h, respectively ([Ducrot et al. 2020](#)). All these data can be accessed through the online Spitzer Heritage Archive database². Observations were obtained with Spitzer Space telescope's Infrared Array Camera (IRAC; [Carey et al. 2004](#)) in subarray mode (32×32 pixels windowing of the detector) with an exposure time of 1.92 s and a cadence of 2.06 min. In order to minimize the pixel-phase effect ([Knutson et al. 2008](#)) the peak-up mode was used ([Ingalls et al. 2016](#)) to fine tune the positioning of the target on the detector following the IRAC Instrument Handbook.³ Finally, calibration was performed using Spitzer pipeline S19.2.0 to output data as cubes of 64 subarray images of 32×32 pixels (the pixel scale being 1.2 arcsec). Each set of exposures was summed over the 2.06 minute cadence to allow for a tractable data volume for carrying out the photometric analysis, which is described in detail in [Delrez et al. \(2018b\)](#) and [Ducrot et al. \(2020\)](#).

2.2 Ground-based observations

In addition to the new Spitzer times, 125 transits were observed by the SPECULOOS-South Observatory (SSO, [Burdanov et al.](#)

[2018](#); [Jehin et al. 2018](#), [Gillon 2018](#), [Delrez et al. 2018a](#)) at Cerro Paranal, Chile, TRAPPIST-South at La Silla Chile, (TS; [Jehin et al. 2011](#); ?), and TRAPPIST-North at Oukaimeden Morocco, (TN; ?). These observations were carried out in an I+z filter with exposure times 23s, 50s and 50s, respectively; characteristics of this filter are described in [Murray et al. \(2020\)](#). Observations were also performed with the Liverpool Telescope (LT, [Steele et al. 2004](#)) and the William-Herschel Telescope (WHT), both installed at the Roque de los Muchachos observatory, La Palma. Only one transit of planet b and one of d were targeted with the WHT whereas 15 transits of several planets were targeted with LT. For LT observations, the IO:O optical wide field camera was used in Sloan z band with 20s exposure time. One transit of b was observed with the Himalayan Chandra Telescope (HCT). Finally, a total of 26 transits were observed in the near-IR (1.2 -2.1 μm) with the WFCAM near-IR imager of the the United Kingdom Infra-Red Telescope (UKIRT) ([Casali et al. 2007](#)), the IRIS2IR-imager installed on the the Anglo-Australian Telescope (AAT) ([Tinney et al. 2004](#)), and the HAWK-I cryogenic wide-field imager installed on Unit Telescope 4 (Yepun) of the ESO Very Large Telescope (VLT) ([Siebenmorgen et al. 2011](#)). These observations are summarized in Table 1, and additional information may be found in [Gillon et al. \(2016\)](#) for WHT and TRAPPIST, in [Ducrot et al. \(2018\)](#) for SSO and LT, and in [Gillon et al. \(2017\)](#) and [Burdanov et al. \(2019\)](#) for AAT, UKIRT and VLT.

For all ground-based observations, a standard calibration (bias, dark and flat-field corrections) was applied to each image, and fluxes were measured for the stars in the field with the DAOPHOT aperture photometry software ([Stetson 1987](#)). Differential photometry was then performed after a careful selection of comparison stars, followed by an MCMC analysis to retrieve transit parameters.

2.3 K2 and HST observations

The K2 mission ([Howell et al. 2014](#)) observed the TRAPPIST-1 system over campaigns 12 and 19 ([Luger et al. 2017a](#)), in both long- and short-cadence imaging modes. We only use the short-cadence data from campaign 12 for this analysis, with ~ 1 minute sampling. We use our own photometric pipeline to track the star and produce a light curve from the Target Pixel Files (TPF). To model and correct TRAPPIST-1's stellar variability and K2's pointing-drift-correlated systematic noise, we use a Gaussian process with a quasi-periodic kernel, following the procedure described in [Grimm et al. \(2018\)](#). The campaign 12 data contains 48, 30, 19, 12, 7, 6 and 4 transits of planets b, c, d, e, f, g and h, respectively.

Transit times for Hubble Space Telescope observations were utilized, as described in [Grimm et al. \(2018\)](#); [de Wit et al. \(2016, 2018\)](#); [Wakeford et al. \(2018\)](#).

2.4 Transit time measurements and analysis

Assembling the heterogeneous sample of transits which were obtained from a variety of ground- and space-based telescopes, these observations were analyzed together with a global photometric analysis of transits, as described in [Ducrot et al. \(2020\)](#), with a separate analysis of the overlapping transits once the single-transit analysis was completed. For each planet a fixed time of transit for epoch zero (T_0) and fixed period (P) were used, but with timing offset ("TTV") as a fitted parameter for each transit as described by [Ducrot et al. \(2020\)](#). The timing offsets are added back to the ephemeris to obtain the measured transit times and uncertainties.

The final observed dataset for the transit-timing analysis is

² <http://sha.ipac.caltech.edu>

³ IRAC Instrument Handbook

Planet	HCT	SSO/TS/TN	LT	WHT	VLT/AAT/UKIRT	HST	Spitzer	K2	Duplicates	Total
b	1	45	7	1	10	1	64	48	16	161
c	0	28	8	0	7	1	47	30	14	107
d	0	11	1	1	5	2	23	19	9	53
e	0	18	4	0	3	2	18	12	8	49
f	0	9	2	0	4	2	16	7	7	33
g	0	11	0	0	3	2	13	6	5	30
h	0	3	2	0	0	0	7	4	2	14
Total	1	125	24	2	32	10	188	126	61	447

Table 1. Number of transits from ground-based and space-based observations. Duplicates stand for transits observed simultaneously with distinct observatories. Details on the corresponding observations can be found in [Gillon et al. \(2016, 2017\)](#); [Grimm et al. \(2018\)](#); [de Wit et al. \(2016, 2018\)](#); [Delrez et al. \(2018b\)](#); [Ducrot et al. \(2018\)](#); [Burdanov et al. \(2019\)](#); [Ducrot et al. \(2020\)](#).

given by: $\mathbf{y} = \{t_{\text{obs},i,j}, \sigma_{i,j}; i = 1, \dots, 7; j = 1, \dots, N_i\}$, where i labels each of the seven planets, N_i is the number of transits for the i th planet (Table 1), and j labels each transit for the i th planet, so that $t_{\text{obs},i,j}$ is the j th observation of the i th planet, and $\sigma_{i,j}$ is the corresponding measurement error. The total number of transits is $N_{\text{trans}} = \sum_{i=1}^7 N_i = 447$.

Table B2 lists the complete set of transit times and uncertainties which were utilized in the present analysis.

With this sample of transit times collected, we proceed to describe our dynamical analysis, starting with the likelihood function and evidence for outliers.

3 EXCESS OF OUTLIERS AND ROBUST LIKELIHOOD MODEL

We first carried out a preliminary 7-planet, plane-parallel N-body model fit to the transit times using a χ^2 log likelihood function, i.e. assuming a Gaussian uncertainty for each transit time given by the derived timing uncertainty, which was optimized using the Levenburg-Marquardt algorithm. We found that the residuals of the fit have many more outliers than is probable assuming a Gaussian distribution for the timing uncertainties.

Figure 1 shows the cumulative distribution function (CDF) and a histogram of the normalized residuals versus a single Gaussian probability distribution function (PDF) with unit variance (orange line). This CDF distribution function disagrees with the Gaussian CDF in the wings for $P(>z) \lesssim 0.1$ and $P(>z) \gtrsim 0.9$, where $z = (t_{\text{obs},i,j} - t_{ij}(\mathbf{x}_{\text{dyn}}))/\sigma$ are the normalized residuals, with the model time, $t_{ij}(\mathbf{x}_{\text{dyn}})$, as a function of the dynamical model parameters, \mathbf{x}_{dyn} , described below. This indicates that there is a significant excess of outliers with large values of $|z|$ relative to a Gaussian distribution. The histogram in Figure 1 also demonstrates this clearly: there are 8 data points with $z < -3$ and 7 with $z > 3$. With 447 transit time measurements, we would only have ≈ 1.2 data points with $|z| > 2$ if the distribution were Gaussian with accurately estimated uncertainties. This excess is even more apparent at $|z| > 4$.

We have examined the individual transits that show these discrepancies, and there is nothing unusual about their light curves, such as flares, overlapping transits, or other anomalies. The outliers appear for each of the planets, in both ground- and space-based data, and for measurements with different sizes of uncertainties. We do not think that our N-body model is in error (and we have tried to fit with an extra planet, without a significant improvement in the number of outliers; see below). Consequently, we believe that these

outliers are due to variations in the measured times of transits which are not associated with dynamics of the system.

We suspect instead that these outliers are a consequence of some systematic error(s) present in the data. There are a variety of possibilities: uncorrected instrumental/observational systematics; time-correlated noise due to stellar variability; stellar flares (which may be too weak to be visible by eye, but might still affect the times of transit); or stellar spots. Again, our examination of the light curves did not point to a single culprit, so we are unable to model and/or correct for any of these effects. Our data are not unique in this respect: similar outliers have been seen in other transit-timing analyses, as described in [Jontof-Hutter et al. \(2016\)](#).

Consequently, our transit-timing model will be affected by these timing outliers, which make an excessive contribution to the χ^2 of the model, and thus can affect the inference of the model parameters. This can cause both the parameters *and* the uncertainties to be mis-estimated. To make progress, we have modified the likelihood model to account for outliers.

We examined two approaches to creating a heavy-tailed likelihood function, which better describes the data: a mixture model ([Hogg et al. 2010](#); [Foreman-Mackey 2014](#)) and a Student's t-distribution ([Jontof-Hutter et al. 2016](#)). In both cases we fit the normalized residuals to a model in which the width of the distribution was allowed to vary, which we parameterize with an additional factor multiplying the variance, which we refer to below as V_1 . In the case of the mixture model, there are two additional parameters: the relative probability of the background, and the variance of the background. In the Student's t-distribution case there is only one additional free parameter: the number of degrees of freedom, ν (we treat this as a continuous parameter).

Figure 1 shows a histogram of the outliers of the best-fit transit-timing model (described below), and shows that the Student's t-distribution gives a much higher probability for outliers. Given that i) the Student's t-distribution has one fewer free-parameter than a mixture model, ii) the mixture-model can have a bimodal probability (the background and foreground can interchange, which causes the posterior probability distribution to be multiply-peaked), and iii) the Student's t-distribution has been used in a prior transit-timing study ([Jontof-Hutter et al. 2016](#)), we settled on using this distribution to describe the increased probability of the outlier data points.

With the description of the dataset complete, we next describe our efforts to model the data.

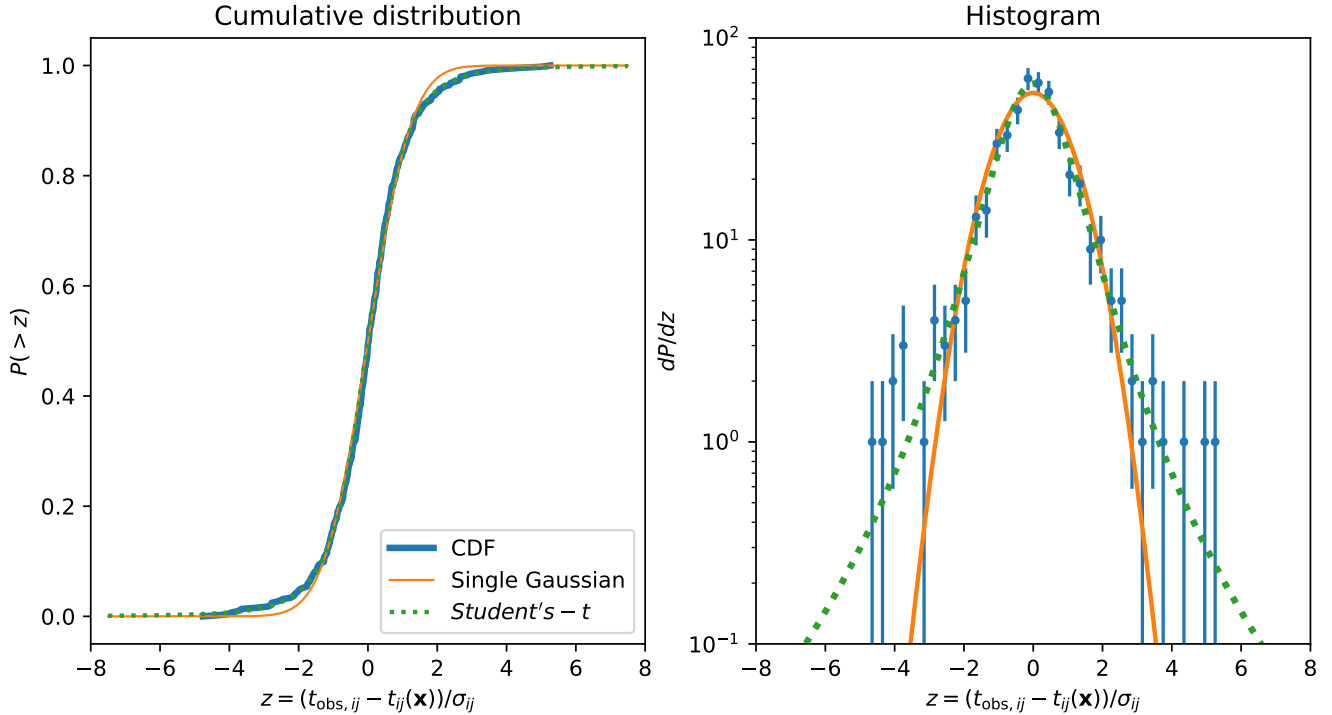


Figure 1. Probability distribution of outliers. Left: Cumulative distribution function of the normalized residuals, z . Blue line is a sequence of normalized residuals. Orange line is the CDF of a Gaussian distribution. Dashed green line is the CDF of a Student's t -distribution. Right: Histogram of the normalized residuals. Blue data points are a histogram of the normalized residuals with Poisson uncertainties. The other lines have the same meaning as the left panel for the probability distribution function (PDF), scaled to match the histogram.

4 TRANSIT-TIMING ANALYSIS

In this section we describe our transit-timing analysis in detail, starting first with a description of our dynamical model.

4.1 N-body integration

We integrate the N-body dynamics in Cartesian coordinates with a novel symplectic integrator, NbodyGradient, which is based on the algorithm originally described in [Hernandez & Bertschinger \(2015\)](#), derived from the non-symplectic operator of [Gonçalves Ferrari et al. \(2014\)](#).⁴ The time-evolution operator of the integrator is a succession of Kepler 2-body problems and simple "kick" and "drift" operators. The advantage over traditional symplectic methods ([Wisdom & Holman 1991](#)) is that the dominant error is due to three-body interactions, while in the standard methods, the dominant error is due to two-body interactions, meaning close encounters between non-stellar bodies are treated poorly ([Hernandez & Dehnen 2017](#)). The Kepler problem for each pair is solved with an efficient universal Kepler solver ([Wisdom & Hernandez 2015](#)). The symplectic integrator is made to be time-symmetric to yield second-order accuracy ([Hernandez & Bertschinger 2015](#)). Then, a simple operator can be introduced to double the order of the method ([Dehnen & Hernandez 2017](#)). We have found that numerical cancellations occur between Kepler steps and negative drift operators, and so we have introduced an analytic cancellation of these terms

to yield an algorithm which is numerically stable, which converges for small time steps ([Agol & Hernandez 2020](#)).

The initial conditions are specified with Jacobi coordinates and we use a set of orbital elements for each planet given by $\mathbf{x}_{\text{dyn}} = (\{m_i, P_i, t_{0,i}, e_i \cos \omega_i, e_i \sin \omega_i\}; i = 1, \dots, N_p)$ where N_p is the number of planets for a total of $5N_p$ dynamical parameters. In addition we take the star to have a mass, $m_0 = M_*/M_\odot$, which we fix to one. The units of time for the code are days, while the length scale of the code is taken to be $m_0^{1/3}$ AU.⁵ The initial orbital ephemeris, $(P_i, t_{0,i})$, consists of the period and initial time of transit which each planet *would* have if it orbited a single body with the mass of the star and the interior planets, and was not perturbed by the exterior planets. We use these variables (in lieu of initial semi-major axis and mean longitude) as they are well constrained by the times of transits. We convert these analytically to the time of periastron passage, once the Kepler equation is solved to yield the initial eccentric anomaly for each initial Keplerian. Finally, the eccentricity, e_i , and longitude of periastron, ω_i , for each Keplerian we parameterize in terms of $e_i \cos \omega_i$ and $e_i \sin \omega_i$ to avoid the wrapping of the angle ω_i . We transform from Jacobi coordinates to Cartesian coordinates to complete the initial conditions.

For our transit-timing analysis, we assume that the planets are plane-parallel and edge-on in their orbits, allowing us to neglect the inclination and longitude of nodes for each planet.

A symplectic integration time step, h , is selected to be small,

⁵ Note that as we take $m_0 = 1$ in our simulations, we need to multiply the output of positions and velocities from the code by $(M_*/M_\odot)^{1/3}$ to scale to a stellar mass M_* .

⁴ The code may be found at <https://github.com/ericagol/NbodyGradient>

<5%, compared with the orbital period of the innermost planet (Wisdom & Holman 1991). For most of our integrations we use a time step of $h = 0.06$ days, or about 4% of the orbital period of planet b.

The transit times are found by tracking the positions of each planet relative to the star across a time step. Then, when the dot product of the relative velocity of the planet and star with the relative position goes from positive to negative, we flag a routine which iterates with Newton's method to find the transit time, which is taken to be when this dot product equals zero (Fabrycky 2010), corresponding to the mid-point of the transit if acceleration is negligible over the duration of the transit. The resulting model we obtain is for the j th transit of the i th planet, giving each transit time as a function of the initial conditions, $t_{ij}(\mathbf{x}_{\text{dyn}})$, which can then be compared to the observed times, $t_{\text{obs},ij}$.

Once the transit times have been found for every planet over the duration of the time integration, these are then matched with the observed transit times to compute the likelihood using the Student's t probability distribution. The log likelihood function which we optimize for each data point is given by

$$\begin{aligned} \log \mathcal{L}_{ij}(\mathbf{x}_{\text{dyn}}, \nu, V_1) = & -\frac{\nu+1}{2} \log \left(1 + \frac{(t_{\text{obs},ij} - t_{ij}(\mathbf{x}_{\text{dyn}}))^2}{\nu \sigma_{ij}^2 V_1} \right) \\ & - \frac{1}{2} \log(\pi \nu V_1) + \log \Gamma \left(\frac{\nu+1}{2} \right) - \log \Gamma \left(\frac{\nu}{2} \right), \end{aligned} \quad (2)$$

where $\Gamma(x)$ is the Gamma function (Fisher 1925).

The total log likelihood function is given by

$$\log \mathcal{L}(\mathbf{x}_{\text{dyn}}, \nu, V_1) = \sum_{i=1}^{N_p} \sum_{j=1}^{N_i} \log \mathcal{L}_{ij}(\mathbf{x}_{\text{dyn}}, \nu, V_1), \quad (3)$$

where N_p is the number of planets; we use $N_p = 7$ for most of our analysis.

Note that we assume that the timing errors are uncorrelated. Most transits are well separated in time, and thus this is an accurate assumption as the noise should be uncorrelated on these timescales. There are a small number of transits (about 6%) that overlap in time, and thus may have correlated uncertainties; we do not account for this in the likelihood function.

4.2 Uncertainty analysis

We carried out the uncertainty analysis on the model parameters with three different approaches:

- (i) Laplace approximation.
- (ii) Likelihood profile.
- (iii) Markov-chain Monte Carlo.

First, in our Laplace approximation analysis, we assume a uniform prior on the model parameters and expand the likelihood as a multi-dimensional normal distribution. We maximize the likelihood model using the Levenberg-Marquardt algorithm, which requires the gradient and Hessian of the log likelihood. Once the maximum likelihood is found, we compute an approximate Hessian at the maximum log likelihood (see Appendix A). The inverse of the Hessian matrix yields an estimate of the covariance amongst the parameters at the maximum likelihood, whose diagonal components provide an initial estimate for the parameter uncertainties; we will also use the Hessian for more efficient sampling of the Markov chain.

The second approach we use is to compute the likelihood profile for each model parameter. In this case each parameter is varied over a grid of values over a range given by $\pm 3\sigma_{x_i}$, where σ_{x_i} equals the square root of the diagonal component for the i th model parameter from the covariance matrix. At each value along the grid for each parameter we optimize the likelihood with a constraint which keeps the parameter pinned at the grid point. This results in a profile of the maximum likelihood of each parameter, optimized with respect to all other parameters, which yields a second estimate for the uncertainties on the parameters. The likelihood profile approach does not assume a normal distribution and is useful for checking for a multi-modal probability distribution which can trip up Markov-chain analysis.

However, both of these error estimates are incomplete as they do not account for non-linear correlations between parameters, for the non-Gaussian shape of the posterior probability, nor for the prior probability distribution.⁶ Nevertheless, the agreement between the two estimates gives a starting point for evaluating our Markov chain analysis, and for gauging the convergence of the chains, which we describe below.

In our initial Markov chain sampling, we found that the parameters of the Student's t -distribution, ν and V_1 , were strongly non-linearly correlated and displayed a likelihood profile which was non-Gaussian. After experimenting with reparameterization, we found that $\log \nu$ and $V_1 e^{1/(2\nu)}$ gave a parameterization which showed a nearly Gaussian likelihood profile in each parameter, and also showed more linear correlations between these two parameters. Accordingly we chose to sample in these transformed parameters.

With this likelihood distribution defined, we can then sample the probability distribution of the model parameters given a prior, which we describe next.

4.3 Prior

We use a uniform prior for each mass and orbital element, with bounds on each, with the exception of the initial eccentricity vectors. Since we sample in the eccentricity vector of each planet, $\mathbf{e}_i = (e_i \cos \omega_i, e_i \sin \omega_i)$, the volume of parameter space scales $\propto e_i$, and so an $1/e_i$ prior is needed to yield a posterior which has a uniform probability with eccentricity, e_i , for the i th planet (Eastman et al. 2013).

In addition to the eccentricity prior, we place broad, uniform priors on each parameter, and we require that the prior boundaries have an edge to the probability which varies smoothly from 1 to 0. For each parameter we choose two bounds for which the prior starts to transition from 1 to 0 with a cubic dependence at both the upper and lower bound. For the bound on a parameter of value ξ we specify

$$\Pi_{\text{bound}}(\xi) = \begin{cases} 0 & \xi \leq \xi_1 \\ 3y^2 - 2y^3; y = \frac{\xi - \xi_1}{\xi_2 - \xi_1} & \xi_1 < \xi < \xi_2 \\ 1 & \xi_2 \leq \xi \leq \xi_3 \\ 3y^2 - 2y^3; y = \frac{\xi_4 - \xi}{\xi_4 - \xi_3} & \xi_3 < \xi < \xi_4 \\ 0 & \xi \geq \xi_4 \end{cases}, \quad (4)$$

⁶ In principle we could include a prior in the Laplace and likelihood profile analyses.

so that the total prior is given by

$$\Pi(\mathbf{x}) = \prod_{i=1}^{N_p} e_i^{-1} \times \prod_{j=1}^{N_{\text{param}}} \Pi_{\text{bound}}(x_j), \quad (5)$$

where the values of ξ_1 – ξ_4 for each parameter $\mathbf{x} = \{x_j; j=1, \dots, N_{\text{param}}\}$ are given in Table B1, where $N_{\text{param}} = 5N_p + 2$. The prior probability, then, is given by $\Pi(\mathbf{x})$, which we multiply by the likelihood function before sampling. This completes the specification of the posterior probability distribution, $P(\mathbf{x}) \propto \Pi(\mathbf{x}) \times \mathcal{L}(\mathbf{x})$, so that we can proceed to discussing the Markov chain sampling of the posterior probability of the model parameters given the data.

4.4 Markov chain sampler

We sample our posterior probability, $P(\mathbf{x})$, with a Markov chain sampler. Given the high dimensionality of our model - 37 free parameters - we chose to use a Markov chain sampler which efficiently samples in high dimensions: Hamiltonian Monte Carlo (HMC; Duane et al. 1987; Neal 2011; Betancourt 2017; Monnahan et al. 2016).⁷ This sampler requires the *gradient* of the likelihood function with respect to the model parameters. The gradient of the likelihood requires the gradient of each transit time with respect to the initial conditions of the N-body integrator.

We have written a module for our N-body integrator which computes the gradient of each transit time by propagating a Jacobian for the positions and velocities of all bodies across every time step throughout the N-body integration (Agol & Hernandez 2020), which is multiplied by the Jacobian of the coordinates at the initial timestep computed with respect to the initial Keplerian elements and masses, which specify the initial conditions and comprise the N-body model parameters.

When a transit time is found during the N-body integration with NbodyGradient, we compute the derivative of each transit time with respect to the coordinates at the preceding time step, which we multiply times the Jacobian at that step to obtain the derivatives of each transit time with respect to the initial conditions. The gradient of the prior with respect to the model parameters, and the gradient of the likelihood with respect to the model times and the Student's t-distribution parameters, are each computed with automatic differentiation, using forward-mode derivatives (Revels et al. 2016). The gradient of the likelihood with respect to the dynamical model parameters is found by applying the chain rule to the automatic derivatives of the likelihood with respect to the model times with the derivatives computed in the N-body model (from NbodyGradient).

For our HMC analysis, we augment the simulation parameters with a set of conjugate momenta, \mathbf{p} , with the same dimension. We sample from the probability distribution, $e^{-H(\mathbf{x}, \mathbf{p})}$, where H is a Hamiltonian given by the negative log posterior,

$$H(\mathbf{p}, \mathbf{x}) = \frac{1}{2} \mathbf{p}^T \mathbf{M}^{-1} \mathbf{p} - \log \mathcal{L}(\mathbf{x}) - \log \Pi(\mathbf{x}), \quad (6)$$

where \mathbf{p} is defined from Hamilton's equations,

$$\dot{\mathbf{p}} = -\frac{\partial H}{\partial \mathbf{x}}. \quad (7)$$

⁷ aka "Hybrid Monte Carlo." Note that the "Hamiltonian" referred to in HMC is not a physical Hamiltonian, but an artificial one used for treating the negative log probability as a potential energy function, and adding a kinetic energy term, with an artificial momentum conjugate to each model parameter ("coordinate").

We take the inverse mass matrix, \mathbf{M}^{-1} , to be the approximate Hessian matrix evaluated at the maximum likelihood, $\mathbf{M}^{-1} = \mathcal{H}(\mathbf{x}_0)^{-1}$ (eqn. A5). Similarly, the Hamiltonian can be used to compute the evolution of the parameter "coordinates,"

$$\dot{\mathbf{x}} = +\frac{\partial H}{\partial \mathbf{p}}. \quad (8)$$

The dot represents the derivative with respect to an artificial "time" coordinate which can be used to find a trajectory through the (\mathbf{x}, \mathbf{p}) phase space which conserves the "energy" defined by this Hamiltonian.

We carry out a Markov chain using the standard approach for HMC. First, we draw the initial momentum from the multi-variate Gaussian distribution defined by the kinetic energy term in the Hamiltonian,

$$\mathbf{p} = \mathbf{M}^{1/2} \mathbf{Z}, \quad (9)$$

where $Z_n \sim N(0, 1)$ is an element of a vector of random normal deviates for $n = 1, \dots, N_{\text{param}}$. We then carry out a leapfrog integration of Hamilton's equations for N_{leap} steps from the starting point with a "time" step ϵ to obtain a proposal set of parameters $(\mathbf{x}_{\text{prop}}, \mathbf{p}_{\text{prop}})$. Since energy is not conserved precisely due to the finite differencing of the leapfrog integration, we then apply a Metropolis rejection step to accept the proposal step with probability

$$P_{\text{accept}} = \min(\exp(-(H(\mathbf{x}_{\text{prop}}, \mathbf{p}_{\text{prop}}) - H(\mathbf{x}, \mathbf{p}))), 1), \quad (10)$$

to determine whether to accept the proposed step and add it to the Markov chain, or to reject it and copy the prior step to the chain.

We carried out some trial integrations to tune two free parameters: ϵ_0 and $N_{\text{leap},0}$. We draw the "time"-step, ϵ , for each integration from the absolute value of a Normal distribution with width ϵ_0 , i.e. $\epsilon \sim |N(0, \epsilon_0)|$. The number of leapfrog steps for each integration we draw from a uniform probability, $N_{\text{leap}} \sim \text{round}(N_{\text{leap},0} \mathcal{U}(0.8, 1.0))$. We found that a choice of $\epsilon_0 = 0.1$ and $N_{\text{leap},0} = 20$. Every integration yields a proposal for which the Metropolis rejection gives a high acceptance rate of 70%.

We ran 112 HMC chains for 2000 steps each (i.e. 2000 leapfrog integrations). Each leapfrog integration averaged about 7 minutes, and so the chains took nine days and four hours to complete on four Broadwell Xeon Processors with 28 cores and 128 GB of memory (each processor is a node in the Hyak Mox cluster at the University of Washington). We found a minimum mean effective sample size of 57 over all chains, for a total number of independent samples of 6409.

4.5 Results

The transit-timing variations are shown in Figure 2, along with our best-fit model. The model is a very good description of the data, although outliers are clearly visible by eye. Given the large range of the sizes of the uncertainties on the data points, we have created a second figure in which a polynomial with an order between 5-30 is fit to the data (shown as a green line in Fig. 2). The polynomial has been subtracted from the model and data, and the resulting differences are shown in Fig. 3. The result shows high-frequency variations which are associated with the synodic periods of pairs of adjacent planets, typically referred to as "chopping." The chopping TTVs encode the mass-ratios of the companion planets to the star without the influence of the eccentricities, and thus provide a constraint on the planet-star mass ratios which is less influenced by degeneracies with the orbital elements (Deck & Agol 2015). The chopping variations are clearly detected for each planet (except

planet d), which contributes to the higher precision of the measurements of the planet masses in this paper.

The results of the posterior distribution of our transit-timing analysis are summarized in Table 2. There are 35 parameters which describe the planets, in addition to two parameters for the Student's t-distribution, $\log \nu = 1.3609 \pm 0.2337$ and $V_1 e^{1/(2\nu)} = 0.9688 \pm 0.1166$ (Figure 6). The posterior mass-ratios and ephemerides are consistent with nearly Gaussian distributions, while the eccentricity vectors show deviations from a Gaussian distribution for the inner two planets b and c, as shown in Figure 5. Hence, the $1 - \sigma$ uncertainties on the eccentricity vector components for these inner two planets should not be used to extrapolate to higher-order significance without using the full distribution.

The posterior distribution of the *ratio* of the planet masses to the star, scaled to a stellar mass of $0.09 M_\odot$, are given in Table 2 and shown in Figure 4. The likelihood profile of the mass-ratios of the planets is also plotted in Figure 4 and appears to be well-behaved. These likelihood profiles are also approximately Gaussian in shape, and track the inverse Hessian evaluated at the maximum likelihood to estimate the covariance (also plotted), albeit with a stronger tail for planet e at lower mass. Compared with the prior masses estimated by Grimm et al. (2018), the masses of each planet have increased with the exception of planet e which has decreased and planet h which remains the same (Table 3). The mass ratios of the posterior distribution from the Markov chain are slightly shifted to smaller values than the likelihood profile and Laplace approximation probabilities for all planets save b and g.

Figure 5 shows the probability distributions for the eccentricity vector components of each of the planets. Each of the eccentricity vector likelihood profile components has a nearly Gaussian shape. Likewise, the Laplace approximation covariance uncertainty estimates are overplotted as Gaussian distributions very closely match the likelihood profile for each parameter. This agreement is reassuring: it indicates that the likelihood distribution is closely approximated by a multi-dimensional normal distribution near the maximum likelihood. In the eccentricity-vector coordinates, the *prior* probability distribution is peaked at zero to ensure that the volume of phase-space at larger eccentricities does not dominate the probability distribution, as shown in the lower right panel of Figure 5. For the planets which have a likelihood distribution which overlaps strongly with zero, the prior distribution causes the Markov chain posterior to have a significantly different distribution from the likelihood profile. This is not due to the prior favoring small eccentricities; rather it is simply a correction for the bias which results by using $e_i \cos \omega_i$ and $e_i \sin \omega_i$ as Markov chain parameters which favors higher eccentricities.

The Student's t-distribution parameters show a posterior distribution which is shifted from the likelihood profile/Laplace probability distribution (Fig. 6). This bias is due to the fact that the likelihood distribution of these parameters shifts upwards whenever the transit-timing model parameters deviate from their maximum-likelihood values. The peak of the posterior distribution of these parameters corresponds to $\nu = 3.9$ and $V_1 = 0.85$, which indicates that the core of the distribution is narrower than the transit-timing uncertainties indicate, while the wings of the distribution are close to $\nu = 4$, which was the value used by Jontof-Hutter et al. (2016).

4.6 Independent N-body TTV analysis

In addition to the N-body code described above, we use the GPU hybrid symplectic N-body code GENGA (Grimm & Stadel 2014) with a Differential Evolution Markov Chain Monte Carlo Method

(DEMC; ter Braak 2006) as described in Grimm et al. (2018) to perform an independent TTV analysis. The parameters for the MCMC analysis are $\mathbf{x} = (\{m_i, P_i, t_{0,i}, e_i, \omega_i\}; i = 1, \dots, N_p)$. The mass of the star is taken to be $M_\star = 0.09 M_\odot$, and the time step of the N-body integration is set to $h = 0.05$ days. The likelihood is assumed to be a normal distribution with the timing errors derived from the timing analyses. For comparison, we have re-run the likelihood-profile computation described above using a normal distribution in place of a Student's t-distribution. The derived masses from the two different analyses agree well with a maximal deviation of the median masses of better than 0.4%, and in all cases less than 13% of the mass-ratio uncertainty. The eccentricities and longitudes of periastron at the initial time agree as well. We interpret this as a validation of the numerical techniques being employed in this paper.

With the transit-timing analysis completed, we now use the N-body model to improve the estimate of the stellar density and the radius-ratios of the planets. To do so we create a photodynamic model, described next.

5 PHOTODYNAMICAL ANALYSIS

With the mass-ratios and orbital parameters derived from the transit-timing analysis, we wish to improve our derivation of the planet and stellar parameters from the Spitzer photometry. The transit depth, transit duration, and ingress/egress duration combined with orbital period constrain the impact parameters and density of the star for each planet (Seager & Mallen-Ornelas 2003). Combining these constraints for each of the planets enables a more precise constraint upon the density of the star (Kipping et al. 2012). The transit durations are affected by the (small) eccentricities, but to a lesser extent. We account for the dynamical constraints on the transit-timing model to improve the photometric constraints upon these parameters, albeit with the dynamical parameters fixed at the maximum likelihood.

We fit a "photo-dynamical" model (Carter et al. 2012) to the data with the following procedure. From the best-fit plane-parallel, edge-on transit time model, we compute the sky velocity, v_{sky} , at each of the mid-transit times, t_0 , from the model (in N-body code units). We then convert the code units to physical units using the density of the star, obtaining the sky velocity in units of R_\star/day . We account for quadratic limb-darkening of the star with parameters ($q_1, \text{Ch1}, q_2, \text{Ch1}, q_1, \text{Ch2}, q_2, \text{Ch2}$) in the two Spitzer channels, and for each planet we specify a planet-star radius ratio (R_p/R_\star) and we assume mid-transit impact parameter (b_0), which is constant for all transits of a given planet. We assume that the limb-darkening parameters are a function of wavelength for the two Spitzer channels, while we treat the planet radius ratios as identical in both wavebands, giving a total of 19 free parameters for the photodynamical model.

We ignore acceleration during the transits, treating the impact parameters as a function of time as

$$b(t) = \sqrt{(v_{\text{sky}}(t - t_0))^2 + b_0^2}. \quad (11)$$

Although this expression ignores the curvature and inclination of the orbits, as well as the acceleration of the planet, the star is so small compared with the orbital radii that this approximation is extremely accurate. The transit model is integrated with an adaptive Simpson rule over each Spitzer exposure time (which has a uniform duration binned to 2.15 minutes), as described in Agol et al. (2019), yielding a light curve computed with a precision of better than 10^{-7} for all cadences.

We compute a photometric model for all seven planets for all

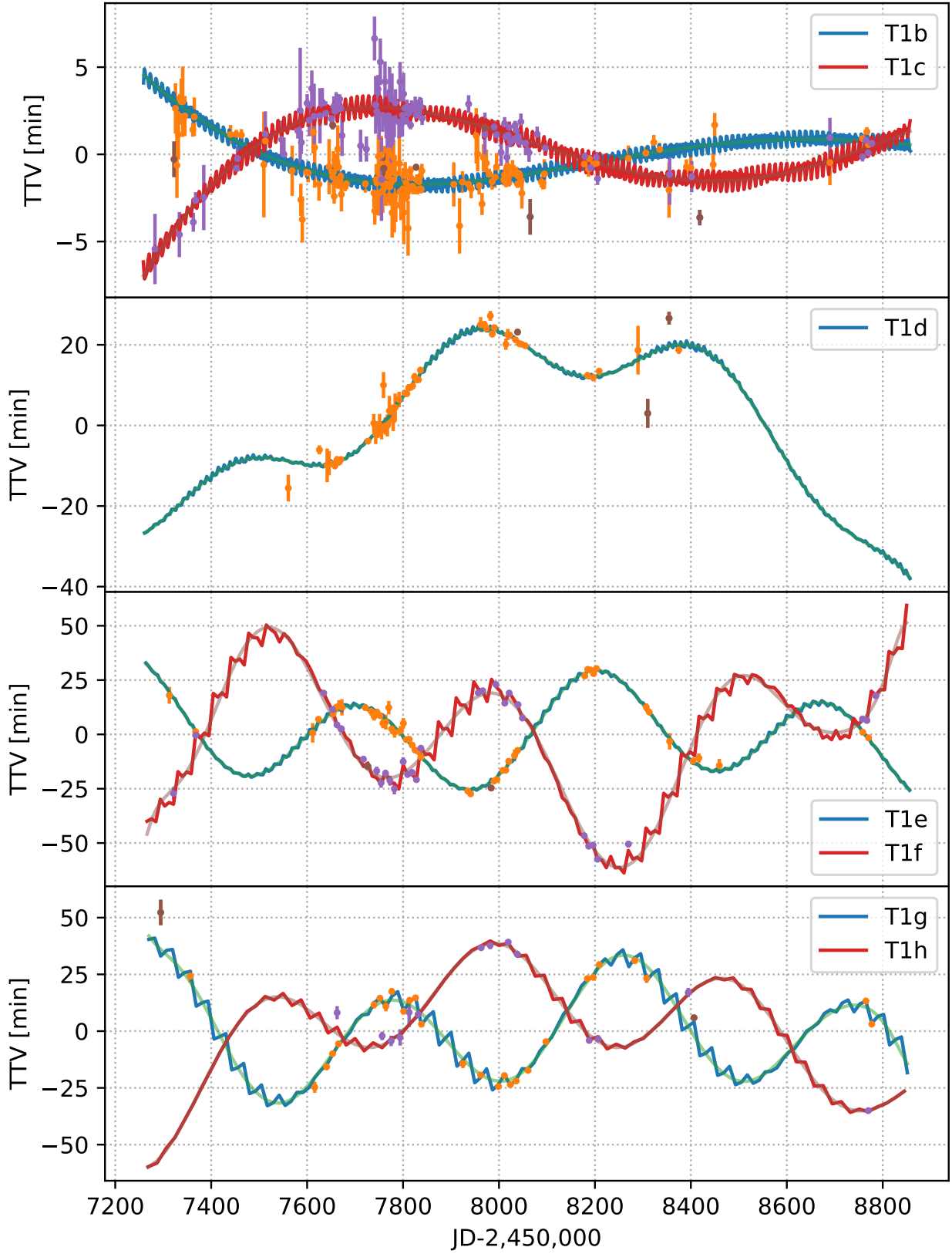


Figure 2. Transit time variation measurements (orange/purple error bars) and best-fit transit-time model (blue/red lines) for a subset of our Spitzer/K2/ground-based data set. The TTVs are the transit times for each planet with a best-fit linear ephemeris removed. Brown error bars indicate $> 3\sigma$ outliers. The light green/brown curves are polynomial fits to each transit timing model used to remove the resonant transit-timing variations; the residuals of the fit ("chopping") are shown in Fig. 3.

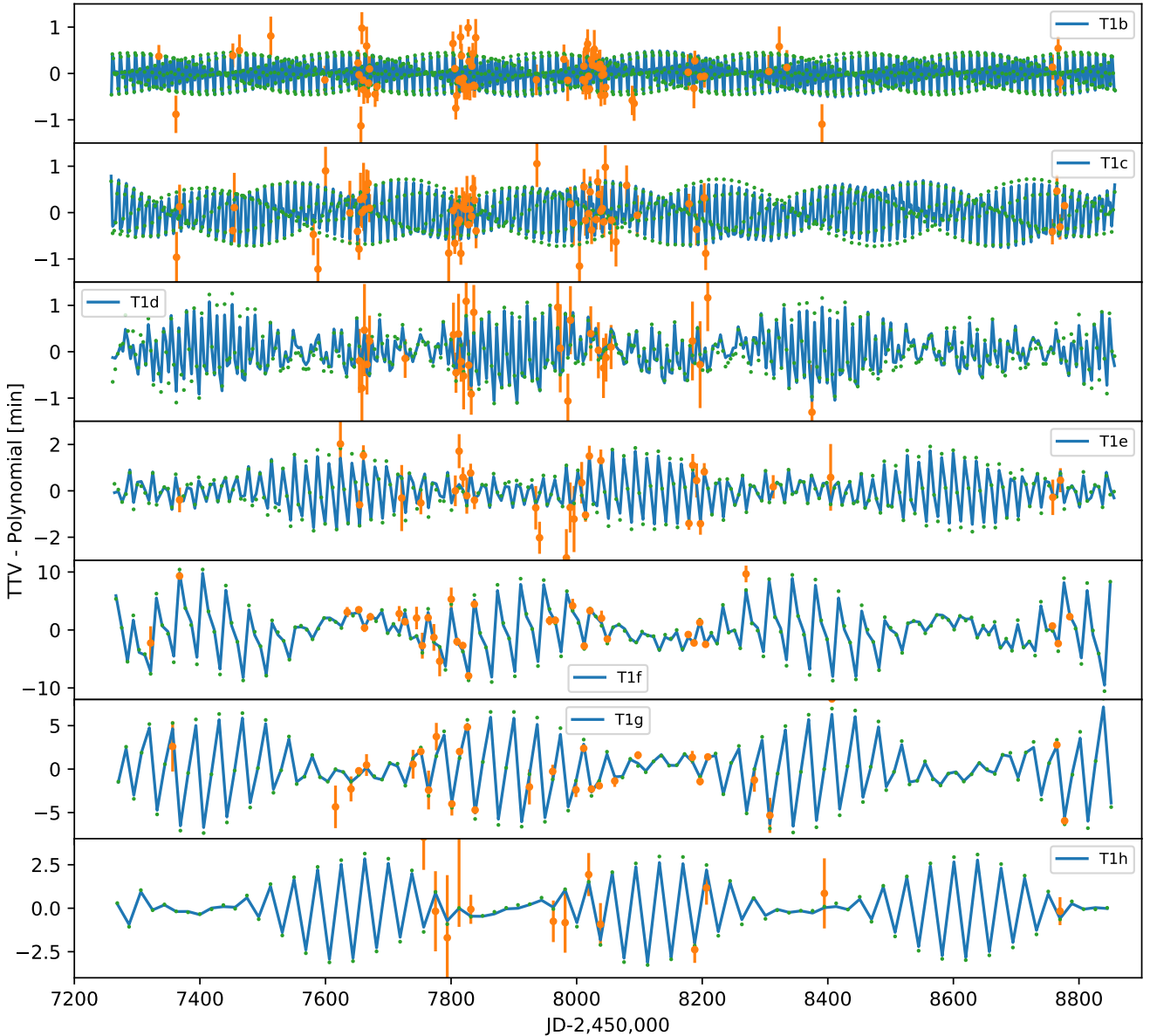


Figure 3. Transit times with a polynomial subtracted (orange error bars) to reveal short-timescale chopping variations (blue model). Green dots show the analytic chopping relation from Agol et al. (2005); Deck & Agol (2015) due to adjacent planets, also with a low-order polynomial removed. For the inner four planets we have only plotted data with uncertainties smaller than the chopping semi-amplitude (many observations have large uncertainties which would obscure the plot).

of the Spitzer data in selected windows around each of the observed transits. Starting with Spitzer photometric data which were already corrected for systematic variations based on the analysis by Ducrot et al. (2020), we fit each transit window with the transit model multiplied by a cubic polynomial, whose coefficients are solved for via regression at each step in the Markov chain. We chose a photometric uncertainty for each window to yield a reduced chi-square of unity in that window. We transform the q_1, q_2 limb-darkening parameters to u_1, u_2 using the formalism of Kipping (2013) for computing the transit model from Agol et al. (2019). After carrying out an initial optimization of the model, we take the photometric error to be the scatter in each observation window, σ_i . With this photometric scatter, we compute a χ^2 of the model with respect to the Spitzer

photometric data, and we optimize the model using a Nelder-Mead algorithm.

To compute the uncertainties on the photodynamical model parameters, we use an affine-invariant Markov chain Monte Carlo algorithm (Goodman & Weare 2010).⁸ The posterior distribution of the results of the fit are given in Table 5. We used a prior which places bounds on each parameter given in Table 4. We utilized 100 walkers run for 50,000 generations, discarding the first 1500 generations for burn-in. We computed the effective sample size using the integrated

⁸ As implemented in the package <https://github.com/madsjulia/AffineInvariantMCMC.jl>

Table 2. Parameters of the TRAPPIST-1 system from transit-timing analysis and their $1 - \sigma$ uncertainties. Note that the mass ratios, μ , of the planets are computed relative to a star, which is assumed to have a mass of $0.09 M_{\odot}$ (this is later combined with the estimate of stellar mass to give our estimate of the planet mass). We also report μ in units of 10^{-5} , and the fractional precision on the measurement of μ , σ_{μ}/μ . The parameters P , t_0 , $e \cos \omega$, and $e \sin \omega$ describe the osculating Jacobi elements at the start of the simulation, on date BJD $-2,450,000 = 7257.93115525$.

Planet	$\mu = \frac{M_P}{M_*}$ [$M_{\oplus} \left(\frac{0.09 M_{\odot}}{M_*} \right)$]	M_P [$10^{-5} M_*$]	$\frac{\sigma_{\mu}}{\mu}$ %	P [day]	t_0 [BJD-2,450,000]	$e \cos \omega$	$e \sin \omega$
b	1.3771 ± 0.0593	4.596 ± 0.198	4.31	1.510826 ± 0.000006	7257.55044 ± 0.00015	-0.00215 ± 0.00332	0.00217 ± 0.00244
c	1.3105 ± 0.0453	4.374 ± 0.151	3.46	2.421937 ± 0.000018	7258.58728 ± 0.00027	0.00055 ± 0.00232	0.00001 ± 0.00171
d	0.3885 ± 0.0074	1.297 ± 0.025	1.90	4.049219 ± 0.000026	7257.06768 ± 0.00067	-0.00496 ± 0.00186	0.00267 ± 0.00112
e	0.6932 ± 0.0128	2.313 ± 0.043	1.84	6.101013 ± 0.000035	7257.82771 ± 0.00041	0.00433 ± 0.00149	-0.00461 ± 0.00087
f	1.0411 ± 0.0155	3.475 ± 0.052	1.49	9.207540 ± 0.000032	7257.07426 ± 0.00085	-0.00840 ± 0.00130	-0.00051 ± 0.00087
g	1.3238 ± 0.0171	4.418 ± 0.057	1.29	12.352446 ± 0.000054	7257.71462 ± 0.00103	0.00380 ± 0.00112	0.00128 ± 0.00070
h	0.3261 ± 0.0186	1.088 ± 0.062	5.69	18.772866 ± 0.000214	7249.60676 ± 0.00272	-0.00365 ± 0.00077	-0.00002 ± 0.00044

Table 3. Mass-ratios of the planets to the star in units of $M_{\oplus}(0.09 M_{\odot}/M_*)$ from Grimm et al. (2018) compared with the results from this paper.

Planet	b	c	d	e	f	g	h
Grimm et al. (2018)	$1.017^{+0.154}_{-0.143}$	$1.156^{+0.142}_{-0.131}$	$0.297^{+0.039}_{-0.035}$	$0.772^{+0.079}_{-0.075}$	$0.934^{+0.080}_{-0.078}$	$1.148^{+0.098}_{-0.095}$	$0.331^{+0.056}_{-0.049}$
This paper	1.3771 ± 0.0593	1.3105 ± 0.0453	0.3885 ± 0.0074	0.6932 ± 0.0128	1.0411 ± 0.0155	1.3238 ± 0.0171	0.3261 ± 0.0186

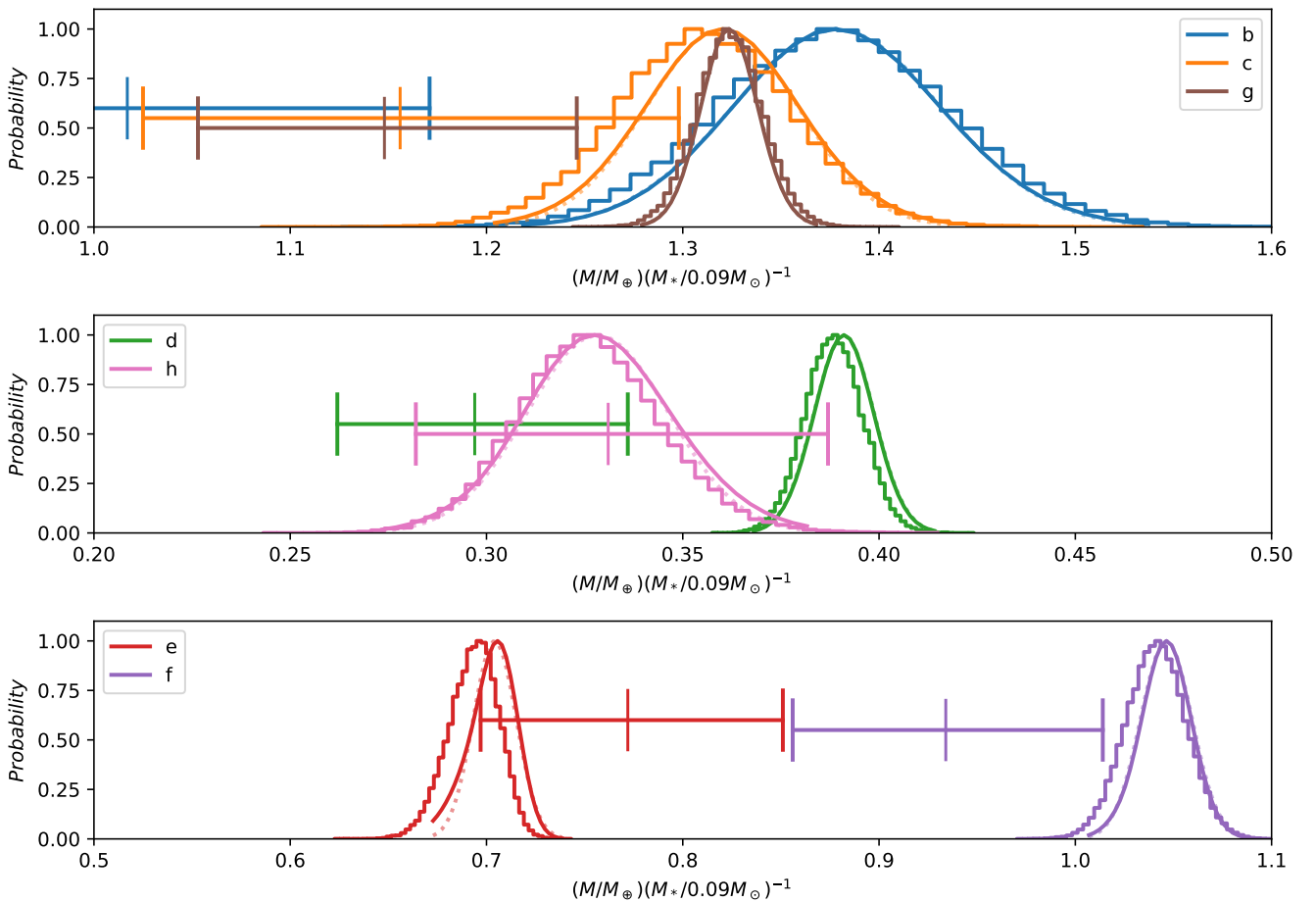


Figure 4. Probability distribution of the mass-ratios of each planet to the star, scaled to a stellar mass of $M_* = 0.09 M_{\odot}$. Thick histograms show the posterior probability distribution of the Markov chain analysis. Horizontal error bars show the $1 - \sigma$ mass-ratios from Grimm et al. (2018). Dark solid curve is the likelihood profile; light, dotted curve is the Laplace approximation.

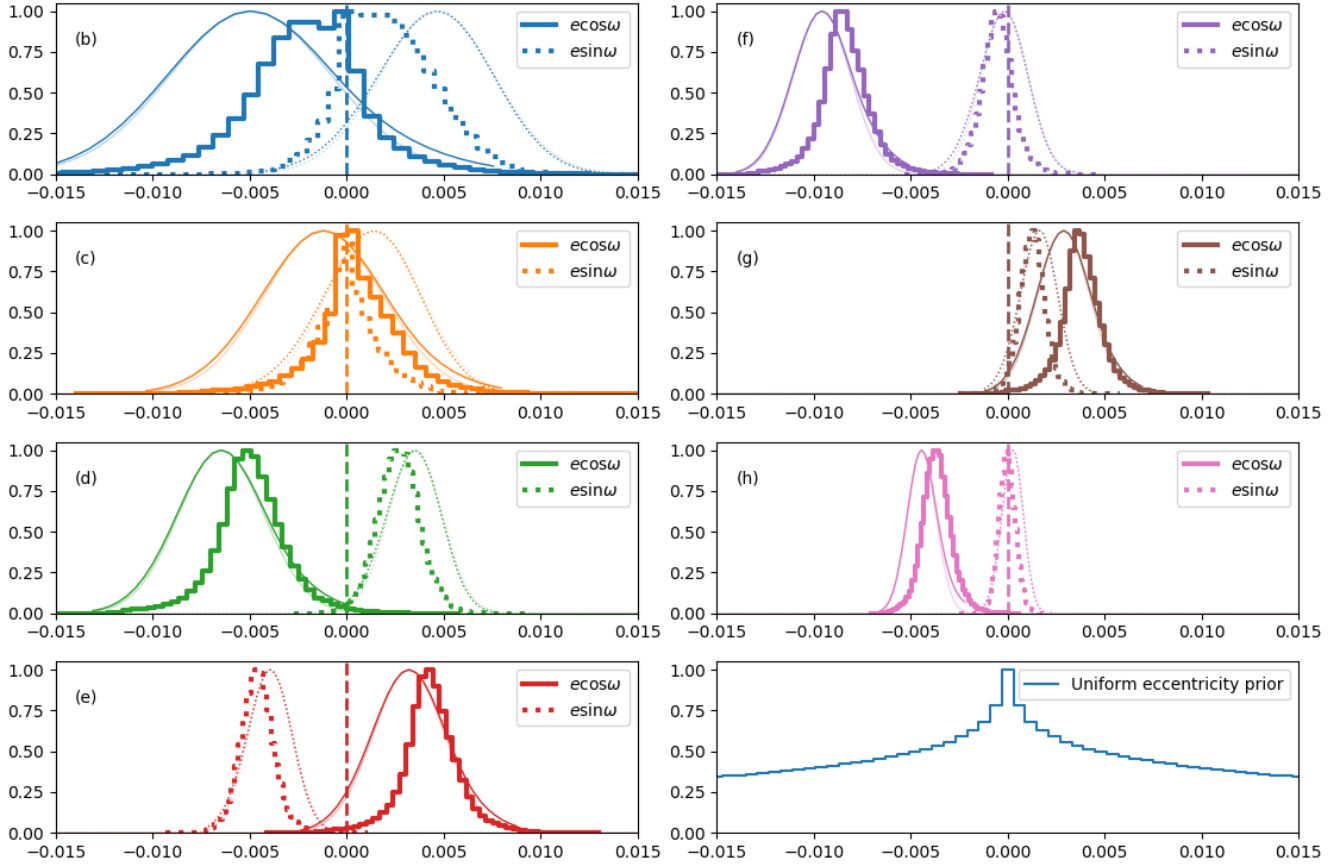


Figure 5. Eccentricity vector probability distribution for each planet (y-axes are relative probability). Thick histogram is the posterior distribution from the Markov chain analysis. Light, thin line is the Laplace approximation. Thin dark line is the likelihood profile. The lower right panel shows the distribution of $e \cos \omega$ or $e \sin \omega$ for a uniform prior on $e \in \mathcal{U}(0, 0.1)$ and $\omega \in \mathcal{U}(0, 2\pi)$.

Parameter	Units	Prior
b_0	R_*	$\mathcal{U}(0, 1)$
R_p	R_*	$\mathcal{U}(0, 0.2)$
ρ_*	ρ_\odot	$\mathcal{U}(0, 100)$
$(q_1, \text{Ch1}, q_2, \text{Ch1})$	—	$\mathcal{U}(0, 1)$
$(q_1, \text{Ch2}, q_2, \text{Ch2})$	—	$\mathcal{U}(0, 1)$

Table 4. Prior bounds on photodynamic parameters. Note that the same bounds on impact parameter, b_0 , and radius ratio, R_p/R_* , are placed on all seven planets.

auto-correlation length, finding a minimum effective samples size of 6000 over all 19 parameters⁹.

To help visualize the model, a photodynamical model with the best-fit parameters is shown in Figure 7 computed over 1600 days. Planets b and c have short periods, and are far from a $j : j + 1$ period ratio, which is necessary for strong TTVs (if the eccentricities are small). Hence both of these planets show weak TTVs, and straighter, but still slightly meandering, riverplots. The outer five planets are pairwise close to a series of $j : j + 1$ resonances, showing strong transit-timing variations on the timescale of the TTV period of

≈ 490 days. The other prominent feature for the outer 4 planets is the slight zig-zag of transits due to chopping (shown in Figure 3).

Figure 8 shows the posterior probability distribution of impact parameters in units of the stellar radius, b_0/R_* , derived from the photodynamical model. Figure 9 shows the probability distribution of stellar density. The density correlates with the impact parameters of each planet, reaching a tail of lower values for higher impact parameters of each planet. The tail of the density probability distribution has an approximately exponential scaling with the density below the peak, and cuts off as a normal distribution above. In table 5 we report the median and 68.3% confidence interval of the stellar density. The inferred density is both slightly larger and more precise than prior analyses (Delrez et al. 2018b), which we discuss below.

Combining the measured density with the measured orbital periods of the planets, we derive the semi-major axis of each planet in units of the stellar radius,

$$\frac{a}{R_*} = \left(\frac{P^2 G M_\odot}{4\pi^2 R_\odot^3} \frac{\rho_*}{\rho_\odot} \right)^{1/3}. \quad (12)$$

With the measured impact parameters, we compute the inclinations of the planets from

$$I = \cos^{-1} \left[\left(\frac{b}{R_*} \right) \left(\frac{a}{R_*} \right)^{-1} \right], \quad (13)$$

⁹ Using <https://github.com/tpapp/MCMCDiagnostics.jl>

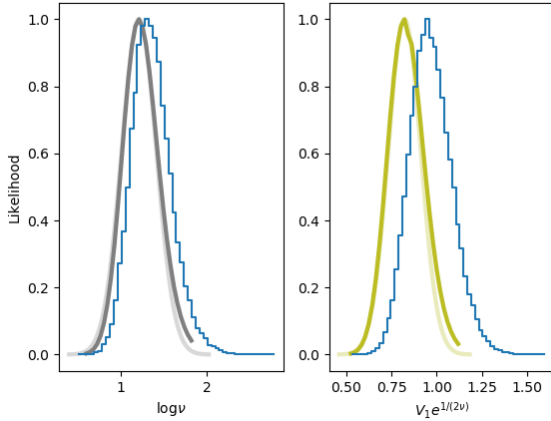


Figure 6. Likelihood profile (dark line) and Gaussian distribution with Laplace approximation uncertainty (light line) for $\log \nu$ (left) and $V_1 e^{1/(2\nu)}$ (right). The posterior probability distributions are shown with blue histograms.

where we have neglected the eccentricity in this formula due to the extremely small values of the eccentricities of the planets from the transit-timing analysis (cf Table 2). The resulting inclination posterior distribution is displayed in Figure 10. Although the inclination is derived from the impact parameters, which we constrain to be positive, in practice the photodynamical model cannot distinguish between inclinations of I and $180 - I$ (Fig. 10), and so we created a histogram of these two options with equal probability.

5.1 Mutual inclinations and stellar density

The outer four planets, e through h , have inclinations which are more precisely determined, and, remarkably, these are aligned very closely, to less than 0.1° , save for the degeneracy of I vs. $180 - I$. The inner three planets have poorer constraints upon their inclinations due to the larger uncertainty of their impact parameters (as seen in Figure 8). Yet, their inclination posteriors have significant overlap with the outer four planets.

As just mentioned, since each inclination may only be inferred relative to the center of the star, the derived distribution is reflected through $180 - I$. However, if some of the planets orbited above and some below the plane of disk of the star, it would be *very* improbable for the outer four planets to show such a precise alignment. We conclude that it is likely that all of the planets orbit on the same side of the star, and as shown in Luger et al. (2017b): the planets 3D orbital inclinations are likely precisely aligned. This also implies that their longitudes of ascending node are likely aligned as well, and so in principle we can place a prior on the scatter of the mutual inclinations of the planets. We have re-run a photodynamic Markov chain with an inclination prior such that the planets' inclinations are drawn from a Gaussian about their mean value, with a standard deviation of σ_θ which is allowed to freely vary in the chain. We find a very tightly aligned distribution of inclinations under this assumption, shown in Figure 11. We also find that very small values of σ_θ are preferred, with $\sigma_\theta = 0.041^{+0.031}_{-0.016}^\circ$. If the outer and inner planets are in fact derived from a common inclination distribution, this implies that the TRAPPIST-1 planetary orbits are *extremely*

flat, even flatter than the Galilean moons which have a dispersion in inclination of 0.25° .

The inclination prior also enables a more precise and symmetric estimate of the density of the star, $\rho_*/\rho_\odot = 53.22 \pm 0.53$. Why is this? Well, the inclination prior tightens the distribution of the impact parameters of planets b and c (as can be seen by comparing Figures 10 and 11). These inner two planets have deep and frequent transits and the sharpest ingress and egress, and hence they provide the tightest constraint upon the density of the star of all seven planets (Ducrot et al. 2020). Thus, given that the inclination prior tightens the distributions of inclinations of these two planets, the stellar density posterior is correspondingly tighter, and the low stellar density tail of the posterior is eliminated (see Figure 9). Despite this tighter constraint upon the stellar density, we decide to forego its use in computing the densities of the planets given the assumptions inherent in the inclination prior.

The coplanarity of the planets may be used to constrain the presence of a more distant, inclined planet given the scatter in their mutual inclinations induced by gravitational perturbations (Jontof-Hutter et al. 2018). Such an analysis should be carried out, but we leave this to future work.

6 PLANET DENSITIES AND MASS-RADIUS RELATION

With the completion of the transit-timing analysis and photodynamic analysis, we are now ready to revisit the mass-radius relation of the TRAPPIST-1 planets.

The only component missing is a constraint upon the mass of the host star. We use the recent analysis by Mann et al. (2019), who have constructed a sample of nearby M-dwarf binaries to calibrate the mass-luminosity ($M_* - M_{K_S}$) relation of M-dwarfs down to a mass of $0.075 M_\odot$.¹⁰ Given the precise parallax measurement available for TRAPPIST-1 thanks to GAIA, the relation yields an estimated mass of $M_* = (0.0898 \pm 0.0023)M_\odot$.

To derive the masses of the planets, we draw mass-ratios of the planets to the star from the posterior distribution of the transit-timing analysis (§4), which we multiply by the mass of the star drawn from a normal distribution with $M_* = (0.0898 \pm 0.0023)M_\odot$. We then draw the radius-ratios and stellar density from the posterior distribution from the photodynamic analysis (§5). With the same mass draw, we compute the stellar radius as

$$R_* = \left(\frac{M_*}{M_\odot} \frac{\rho_\odot}{\rho_*} \right)^{-1/3} R_\odot, \quad (14)$$

which we multiply by each of the radius ratios drawn from the same sample to obtain the planet radii. We carry this out for a large number of samples to derive the probability distribution of the masses and radii of the entire posterior probability sample of the planets.

The probability distribution for the masses and radii of the seven planets are shown in Figure 12. The maximum likelihood values and the posterior distributions (for 1- and 2- σ confidence) are both plotted in this figure. We postpone to §9 a detailed analysis of the densities and resulting constraints on the bulk compositions of the planets.

In addition to masses and radii, we also derive other planetary properties, given in Table 6. Each of the planets has a density intermediate between Mars ($\rho_\oplus = 3.9335 \text{ g/cc} = 0.713 \rho_\oplus$) and

¹⁰ Note that "M" is being used in three ways here: spectral category (M-dwarf), stellar mass (M_*), and absolute magnitude in the K_S band, M_{K_S} .

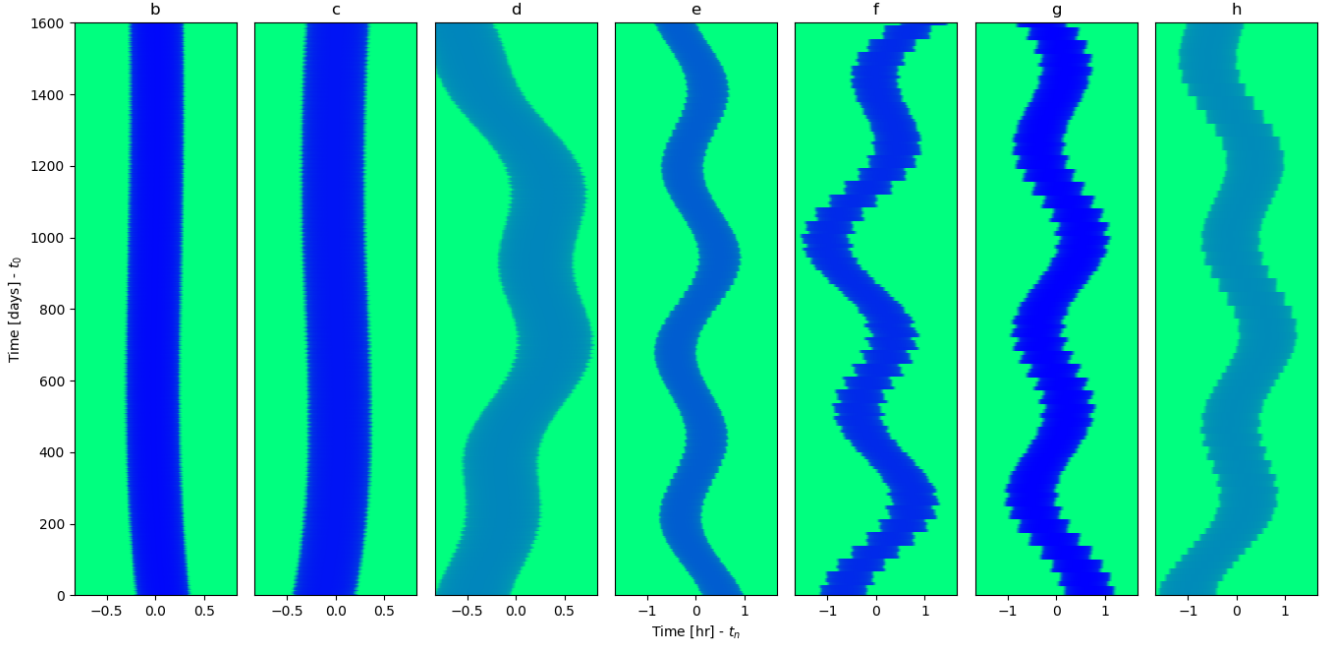


Figure 7. River plots showing every transit over 1600 days for one planet per panel (left to right are b-h, as labelled; the transits of companion planets are omitted from each panel). The x-axis ranges over 200/400x 30-second exposures centered on the mean ephemeris for the n th transit for b-d/e-h respectively (note the 30 sec exposures are higher resolution than the Spitzer time-resolution). Each row contains a transit model, with green being the out-of-transit, and blue in transit. There are (1059,661,395,262,173,129,85) transits of planets b-h, respectively. Planets d and h have the smallest sizes, and hence shallowest depths, causing a lighter color during transit.

Parameter:	ρ_*/ρ_\odot	$q_{1,Ch1}$	$q_{2,Ch1}$	$q_{1,Ch2}$	$q_{2,Ch2}$		
Value:	$53.1737^{+0.7235}_{-1.1758}$	0.1329 ± 0.0524	0.2573 ± 0.1934	0.0593 ± 0.0243	0.4941 ± 0.2037		
Parameter:	$\rho_* [\text{g}/\text{cm}^3]$	$u_{1,Ch1}$	$u_{2,Ch1}$	$u_{1,Ch2}$	$u_{2,Ch2}$		
Value:	$75.0471^{+1.0211}_{-1.6594}$	0.1614 ± 0.0933	0.1958 ± 0.1523	0.2183 ± 0.0563	0.0205 ± 0.0980		
Planet:	b	c	d	e	f	g	h
R_P/R_*	0.0859 ± 0.0004	0.0844 ± 0.0004	0.0606 ± 0.0005	0.0708 ± 0.0006	0.0804 ± 0.0005	0.0869 ± 0.0005	0.0581 ± 0.0009
Depth [%]	0.7378 ± 0.0064	0.7123 ± 0.0064	0.3676 ± 0.0063	0.5012 ± 0.0078	0.6465 ± 0.0076	0.7555 ± 0.0092	0.3375 ± 0.0101
T [min]	36.0632 ± 0.1127	42.0324 ± 0.1265	48.8745 ± 0.2436	55.7633 ± 0.2632	62.8473 ± 0.2502	68.2421 ± 0.2819	76.1617 ± 0.5625
τ [min]	2.8890 ± 0.0463	3.3200 ± 0.0544	2.8161 ± 0.0438	3.8253 ± 0.0708	5.1576 ± 0.0894	6.3098 ± 0.1093	4.8459 ± 0.1129
b/R_*	$0.0947^{+0.0649}_{-0.0607}$	$0.1087^{+0.0592}_{-0.0608}$	$0.0630^{+0.0627}_{-0.0435}$	$0.1907^{+0.0410}_{-0.0405}$	$0.3123^{+0.0231}_{-0.0185}$	$0.3786^{+0.0184}_{-0.0143}$	$0.3784^{+0.0235}_{-0.0229}$
a/R_*	$20.843^{+0.094}_{-0.155}$	$28.549^{+0.129}_{-0.212}$	$40.216^{+0.182}_{-0.299}$	$52.855^{+0.239}_{-0.392}$	$69.543^{+0.314}_{-0.516}$	$84.591^{+0.382}_{-0.628}$	$111.817^{+0.505}_{-0.830}$
I [°]	89.728 ± 0.165	89.778 ± 0.118	89.896 ± 0.077	89.793 ± 0.048	89.740 ± 0.019	89.742 ± 0.012	89.805 ± 0.013

Table 5. Parameters derived from the photodynamic model. Top: Stellar density (in units of solar density), limb-darkening parameters (q_1/q_2) in Spitzer Channel 1 and 2. Bottom: Radius-ratio of planet to star, R_P/R_* ; transit depth, $(R_P/R_*)^2$; transit duration, T (from first to fourth contact); ingress duration, τ (from first to second contact and third to fourth contact); impact parameter in units of stellar radius, b/R_* ; and ratio of semi-major axis to stellar radius, a/R_* .

Earth ($\rho_\oplus = 5.514 \text{ g/cc}$). The surface gravities span a range from 57% of Earth (planet h) to 110% of Earth (planet b).

7 STELLAR PARAMETERS

A byproduct of our analysis is a revision of the properties of the host star. We adopted the empirically-based mass estimated of the star based on Mann et al. (2019), which is consistent with the mass derived by Van Grootel et al. (2018), who first proposed that the mass of the TRAPPIST-1 star is $\approx 0.09 M_\odot$ based upon stellar evolution models and a ground-based parallax measurement. Ducrot et al. (2020) find a luminosity for the star of $L = (5.53 \pm 0.19) \times 10^{-4} L_\odot$,

which, when compared with stellar evolution models, yields a mass of $M = (0.09016 \pm 0.0010) M_\odot$, which is also consistent with the Mann et al. (2019) value. Burgasser & Mamajek (2017) found an older age for the host star, $7.6 \pm 2.2 \text{ Gyr}$, which implies an inflated radius for the star compared with evolutionary models.

Our analysis differs slightly from our prior Spitzer analyses (Delrez et al. 2018b; Ducrot et al. 2020) in that we do not place a prior upon the limb-darkening coefficients of the TRAPPIST-1 host star. This is motivated by the fact that late M dwarf atmospheres are very complex to model and have yet to match observed spectra precisely (Allard et al. 2011, 2012; Juncher et al. 2017), and thus it is possible that limb-darkening predictions may not be reliable.

The TRAPPIST-1 system has the advantage that the planets

Planet:	b	c	d	e	f	g	h
$R [R_{\oplus}]$	$1.116^{+0.014}_{-0.012}$	$1.097^{+0.014}_{-0.012}$	$0.788^{+0.011}_{-0.010}$	$0.920^{+0.013}_{-0.012}$	$1.045^{+0.013}_{-0.012}$	$1.129^{+0.015}_{-0.013}$	$0.755^{+0.014}_{-0.014}$
$M [M_{\oplus}]$	1.374 ± 0.069	1.308 ± 0.056	0.388 ± 0.012	0.692 ± 0.022	1.039 ± 0.031	1.321 ± 0.038	0.326 ± 0.020
$\rho [\rho_{\oplus}]$	$0.987^{+0.048}_{-0.050}$	$0.991^{+0.040}_{-0.043}$	$0.792^{+0.028}_{-0.030}$	$0.889^{+0.030}_{-0.033}$	$0.911^{+0.025}_{-0.029}$	$0.917^{+0.025}_{-0.029}$	$0.755^{+0.059}_{-0.055}$
$g [g_{\oplus}]$	1.102 ± 0.052	1.086 ± 0.043	0.624 ± 0.019	0.817 ± 0.024	0.951 ± 0.024	1.035 ± 0.026	0.570 ± 0.038
$v_{\text{esc}} [v_{\text{esc}, \oplus}]$	1.109 ± 0.026	1.092 ± 0.022	0.701 ± 0.010	0.867 ± 0.012	0.997 ± 0.012	1.081 ± 0.013	0.656 ± 0.020
$S [S_{\oplus}]$	$4.153^{+0.161}_{-0.159}$	$2.214^{+0.086}_{-0.085}$	$1.115^{+0.043}_{-0.043}$	$0.646^{+0.025}_{-0.025}$	$0.373^{+0.015}_{-0.014}$	$0.252^{+0.010}_{-0.010}$	$0.144^{+0.006}_{-0.006}$
$a [10^{-2} \text{AU}]$	1.154 ± 0.010	1.580 ± 0.013	2.227 ± 0.019	2.925 ± 0.025	3.849 ± 0.033	4.683 ± 0.040	6.189 ± 0.053
$R [10^8 \text{ cm}]$	$7.119^{+0.087}_{-0.077}$	$6.995^{+0.086}_{-0.077}$	$5.026^{+0.071}_{-0.066}$	$5.868^{+0.082}_{-0.075}$	$6.664^{+0.085}_{-0.077}$	$7.204^{+0.094}_{-0.085}$	$4.817^{+0.091}_{-0.088}$
$M [10^{27} \text{ g}]$	8.211 ± 0.412	7.814 ± 0.335	2.316 ± 0.074	4.132 ± 0.130	6.205 ± 0.184	7.890 ± 0.226	1.945 ± 0.122
$\rho [g \text{ cm}^{-3}]$	$5.425^{+0.265}_{-0.272}$	$5.447^{+0.222}_{-0.235}$	$4.354^{+0.156}_{-0.163}$	$4.885^{+0.168}_{-0.182}$	$5.009^{+0.138}_{-0.158}$	$5.042^{+0.136}_{-0.158}$	$4.147^{+0.322}_{-0.302}$
$g [10^3 \text{ cm s}^{-2}]$	1.080 ± 0.051	1.065 ± 0.042	0.611 ± 0.019	0.801 ± 0.024	0.932 ± 0.024	1.015 ± 0.025	0.558 ± 0.037
$v_{\text{esc}} [\text{km s}^{-1}]$	12.400 ± 0.292	12.205 ± 0.241	7.839 ± 0.110	9.694 ± 0.133	11.145 ± 0.137	12.087 ± 0.142	7.335 ± 0.227
$S [10^6 \frac{\text{erg}}{\text{cm}^2}]$	$5.652^{+0.220}_{-0.216}$	$3.013^{+0.117}_{-0.115}$	$1.518^{+0.059}_{-0.058}$	$0.879^{+0.034}_{-0.034}$	$0.508^{+0.020}_{-0.019}$	$0.343^{+0.013}_{-0.013}$	$0.196^{+0.008}_{-0.008}$
$a [10^{11} \text{ cm}]$	1.726 ± 0.015	2.364 ± 0.020	3.331 ± 0.028	4.376 ± 0.037	5.758 ± 0.049	7.006 ± 0.060	9.259 ± 0.079

Table 6. Planetary parameters from combining the transit-timing and photodynamic analysis. The units are given with respect to Earth first, and cgs second.

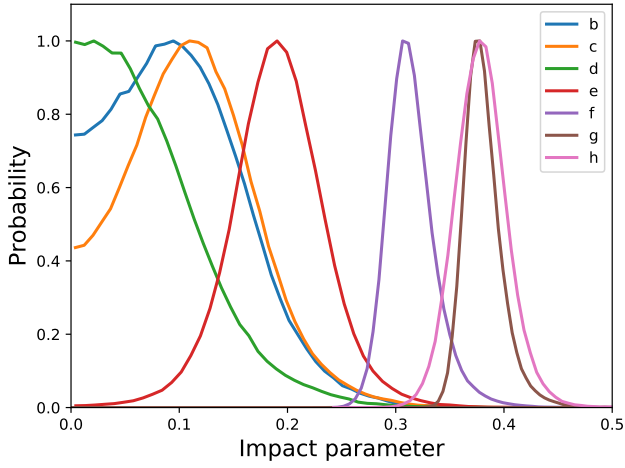


Figure 8. Probability of planet impact parameters using the photodynamic model described in the text.

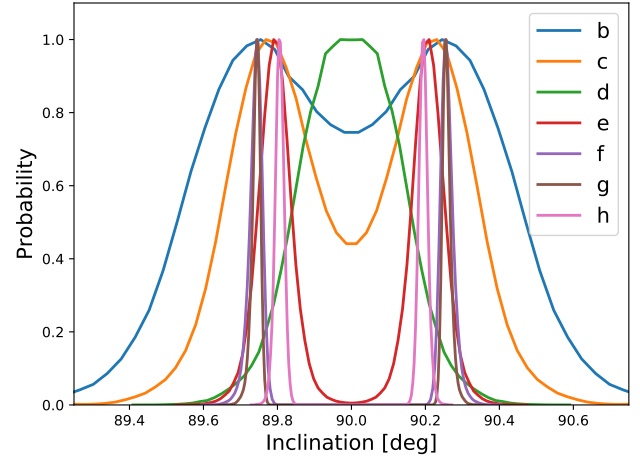


Figure 10. Posterior distribution of inclination angles of the planets given the photodynamical model.

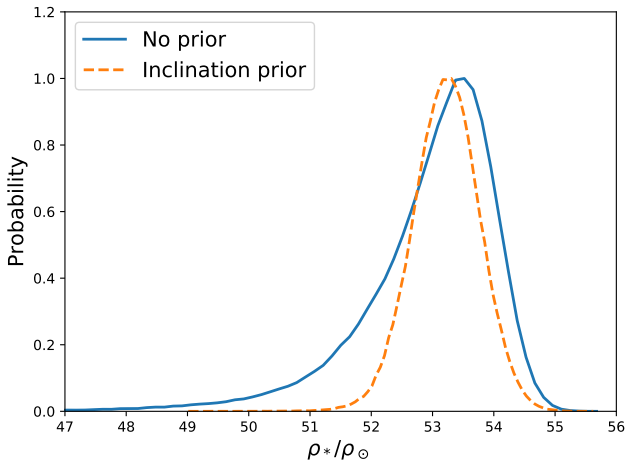


Figure 9. Stellar density derived from the photodynamic model relative to the solar density, with no prior (blue solid line) and with relative inclination prior (orange dashed line).

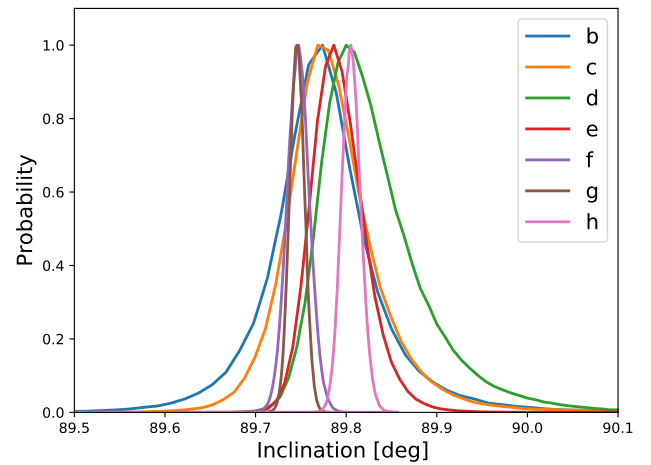


Figure 11. Posterior distribution of inclination angles of the planets from the photodynamical model assuming a prior on the mutual inclinations of $\Pi_i (2\pi\sigma_\theta^2)^{-1/2} e^{-(I_i - \langle I \rangle)^2 / (2\sigma_\theta^2)^{-1}}$.

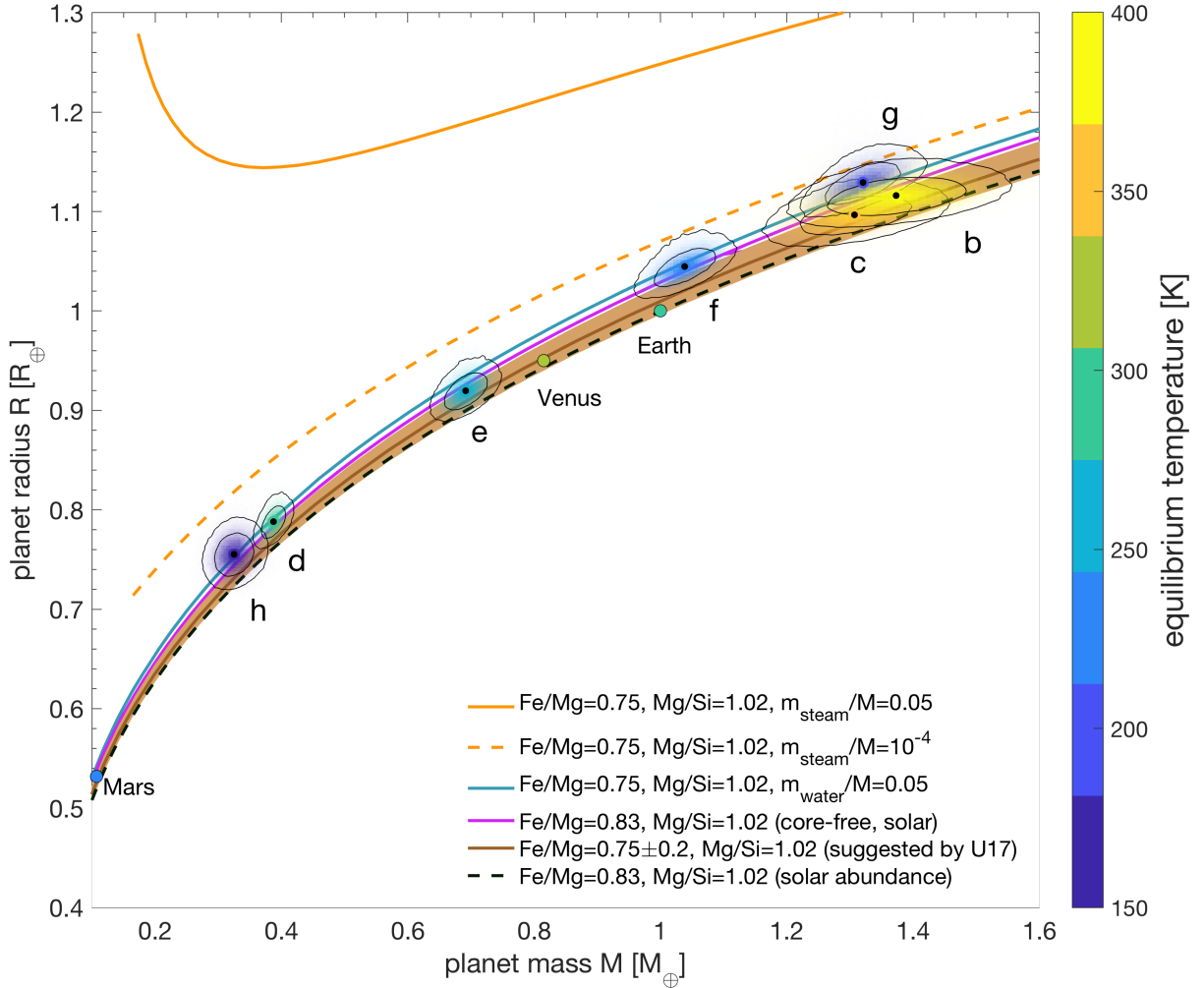


Figure 12. Mass-radius relation for the seven TRAPPIST-1 planets based on our transit-timing and photodynamic analysis. Each planet’s posterior probability is colored by the equilibrium temperature (see key), with the intensity proportional to probability, while the 1- and 2- σ confidence levels from the Markov chain posterior are plotted with solid lines. Theoretical mass-radius relations are overplotted using the model in [Dorn et al. \(2016\)](#). *U17* refers to [Unterborn et al. \(2018\)](#) (see text). The solid blue line was calculated for a 5% water composition, for irradiation low enough (i.e. for planets e, f, g and h) that water is condensed on the surface (assuming a surface pressure of 1 bar and a surface temperature of 300 K). The orange dashed and solid lines were calculated for a 0.01% and a 5% water composition, respectively, for irradiation high enough (i.e. for planets b, c and d) that water has fully evaporated in the atmosphere, with the U17 interior model ([Turbet et al. 2020](#)). The Earth, Venus and Mars are plotted as single points, also colored by their equilibrium temperatures.

Parameter	Value	Ref
$M[M_{\odot}]$	0.0898 ± 0.0023	Mann et al. (2019)
$R[R_{\odot}]$	0.1192 ± 0.0013	This paper
$L[L_{\odot}]$	0.000553 ± 0.000019	Ducrot et al. (2020)
T_{eff} [K]	2566 ± 26	This paper
$\log_{10}(g[\text{cm/s}^2])$	$5.2396^{+0.0056}_{-0.0073}$	This paper

Table 7. Updated stellar parameters based on the combined analysis.

sample different chords of the stellar disk (Figure 8), and given the large number of transiting planets, we are afforded multiple constraints upon the stellar limb-darkening parameters. Figure 13 shows our posterior constraints upon the limb-darkening parameters

of the star based on our photodynamical model, which are reported in Table 5.

Based on the updated stellar density, we have updated the physical parameters of the star. We adopt the luminosity from [Ducrot et al. \(2020\)](#) and the mass from [Mann et al. \(2019\)](#) given the complete and careful analysis from both of those papers. With our updated constraint upon the density of the star, we re-derive the other parameters of the star, which are summarized in Table 7.

8 PLANET DETECTION

With the measured transit times, we can examine whether each of the transiting planets can reveal the presence of its companions. In

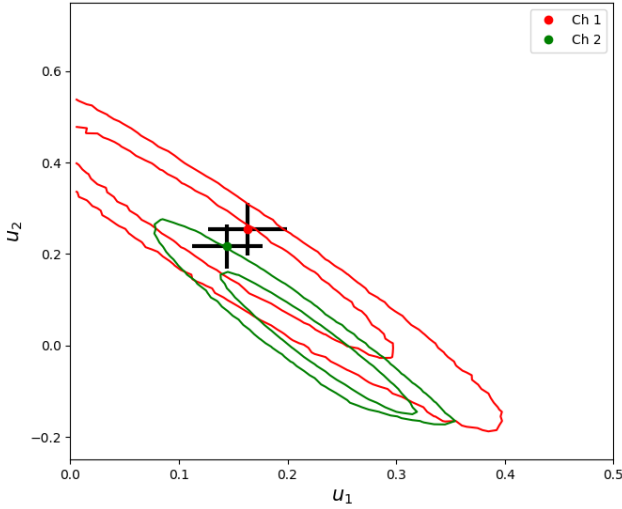


Figure 13. Limb-darkening constraints, 1- and 2- σ confidence contours. Red is Spitzer IRAC Channel 1 ($3.6\mu\text{m}$), while green is Channel 2 ($4.5\mu\text{m}$). Error bars indicate the limb-darkening parameters and uncertainties used as priors in [Ducrot et al. \(2020\)](#)

a transiting planet system, the fractional timing variations are to first order proportional to the mass of the *perturbing* planet ([Agol et al. 2005](#); [Lithwick et al. 2012](#)). Hence, an interesting question to address is whether the transit timing is solely due to the planets in the system.

We start with an exercise of measuring the masses for each of the known planets by examining the companion times of transit. We carried out a sequence of transit-timing analyses in which we masked all of the transits of one of the seven planets. We then re-fit the transiting planet model to the remaining six planets to determine if mass of the seventh "missing" planet could be measured from the timing variations of the other six. We seeded this at the correct value for the missing planets' orbital period and phase; as such, this does not constitute a blind search, but rather a search conducted at the suspected ephemeris of a planet.

Figure 14 shows the results of this experiment. The mass measurements correlate fairly well, although they lie lower than the values obtained from an analysis of all seven planets together (with the exception of planet c). This indicates that if we had, say, a single transit and an indication of the orbital period for a seventh planet, such as was the case for planet h ([Gillon et al. 2017](#); [Luger et al. 2017a](#)), we still could have detected the seventh planet through the transit timing variations of the remaining six planets. The uncertainty on each mass is small, indicating that a blind search over period and phase *might* have detected the missing planets; however, we did not carry out such a comprehensive search.

This brings up the question: could there be an eighth planet in the system which is perturbing the seven transiting planets?

8.1 Search for an eighth planet

With the detection of multiple transits of the six inner planets in TRAPPIST-1, and a single transit of planet h, a clue as to the orbital period of planet h was the series of GLR found between adjacent triplets of planets ([Papaloizou 2014](#)). This relation was then used

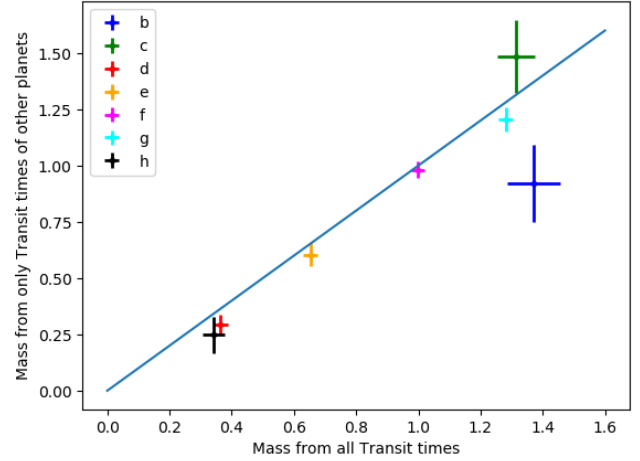


Figure 14. Mass estimate of each planet with a transit-timing analysis of the remaining planets. Mass estimates of each planet from an N-body fit to the transit times of the other six planets are plotted against the mass measurement from the N-body fit to the transit times of all seven planets. Both are in Earth masses and assume a stellar mass of $0.09 M_{\odot}$. The uncertainties are estimated from the likelihood profile.

p	q	P_i [day]	P_i/P_h	j
1	1	39.029	2.08	1
1	2	25.347	1.35	3
1	3	22.695	1.21	4
2	3	28.701	1.53	2

Table 8. Predictions for a GLR of planets g and h with an eighth planet, planet i, with period P_i . The ratio with the period of planet h is given, as well as the value of j for which $P_i/P_h \approx (j+1)/j$.

to predict candidate periods of planet h, based on different integer pairs for its commensurability with planets f and g, and a search through the prior data eliminated all but one possibility at 18.766 days. A subsequent observation of the TRAPPIST-1 system with the K2 spacecraft revealed four more transits of planet h occurring at precisely the period that was predicted ([Luger et al. 2017a](#)). The existence of the GLR amongst the known seven planets has been used to forecast the possible existence of an eighth planet interior ([Pletser & Basano 2017](#)) and exterior ([Kipping 2018](#)) to the seven known transiting planets. There is yet to be a definitive detection of an eighth transiting planet based upon the currently available data ([Ducrot et al. 2020](#)).

It may be possible to detect an exterior eighth planet via transit-timing variations induced on the inner seven planets. Planet h should experience the strongest perturbations by an exterior eighth planet due to the fact that transit-timing variations are a very strong function of the proximity of planets to one another, and also to resonance. Table 8 shows predictions for the period of planet "i", P_i , assuming a GLR configuration with planets g and h given by

$$P_i = q/(-pP_g^{-1} + (p+q)P_h^{-1}) \quad (15)$$

for a range of $1 \leq p, q \leq 3$, which is the same range of integers for the GLRs amongst the inner seven planets. Interestingly these cases are all close to a $j:j+1$ period ratio with planet h, and thus should strongly perturb planet h due to forcing at this frequency.

We carried out a transit-timing search for an eighth planet by placing planets with mass ratios between $2 \times 10^{-6} - 5 \times 10^{-5}$ at these

four trial orbital periods in a coplanar configuration with the other seven planets drawn from a random orbital phase at the initial time, and with eccentricity vector elements drawn from a random normal of width 0.005. We placed a Gaussian prior on the eccentricity vector elements of the eighth planet with a standard deviation of 0.14 to avoid unstable configurations. We then optimized the likelihood with the eight-planet model, carrying out 11,200 optimizations. This analysis was carried out on four Hyak nodes of 28 processors each with 100 optimizations per node, lasting seven days each for about 20,000 CPU hours.

We then carried out a search for evidence of perturbations by planet i by determining if the optimized likelihood of the transiting planets was improved by adding an eighth planet to the transit timing model, using the Bayesian Information Criterion (BIC) to penalize the additional degrees of freedom of the eight-planet model (?). We searched for a change to BIC for the eight-planet model over the seven-planet model with a difference of better than $5 \log N_{\text{trans}} = 30.5$. Given that the inner seven planets show orbital eccentricities with values $\lesssim 0.01$, we only considered an eighth planet candidate plausible if it shows an eccentricity less than this cutoff.

In all 11,200 trial optimization cases we found that only two of the eight-planet models did exceed the BIC criterion, but both significantly exceed an eccentricity of 0.01. Figure 15 shows the change in BIC versus orbital period and mass for planet "i", assuming a mass of the star of $M_* = 0.09 M_\odot$. These two cases with $\Delta \text{BIC} > 0$ do not appear to be plausible planet candidates: they only just exceed the BIC criterion; they both have large eccentricities; and they are not in close proximity to a GLR with planets g and h (even though the initial parameters of the optimization were started near GLR).

We also carried out a search for an eighth planet interior to planet b, and found even smaller improvements in the log likelihood than in the exterior case.

We have not carried out an exhaustive search for eight-planet models at other orbital periods due to the significant volume of parameter space to search. However, it is still possible that an exterior eighth planet is perturbing planet h, and may modify its transit times to a point that affects the posterior masses we infer from our seven planet model. In principle one could include the effect of an eighth planet on the mass inference by adding it to the Markov chain modeling; in practice this would be a challenging model to sample due to the multi-modal nature of the parameter space. We defer such analysis to future work.

9 INTERIOR COMPOSITIONS

In this section we present theoretical interpretation of the planets' interior properties based upon the mass-radius relation we inferred in §6. As there is significant degeneracy in the possible interior compositions, we present a menu of different possibilities in §9.2. However, we start with an approach which is less dependent upon the assumption of interior composition, which we term the "normalized density."

9.1 Initial analysis of planet densities across the system

The probability distribution for the masses and radii of the seven planets are shown in Figure 12 alongside several theoretical mass-radius relationships added for comparison. We have added three rocky mass-radius relationships with different bulk Fe/Mg compositions: (1) $\text{Fe/Mg} = 0.75 \pm 0.2$ as suggested by Unterborn et al.

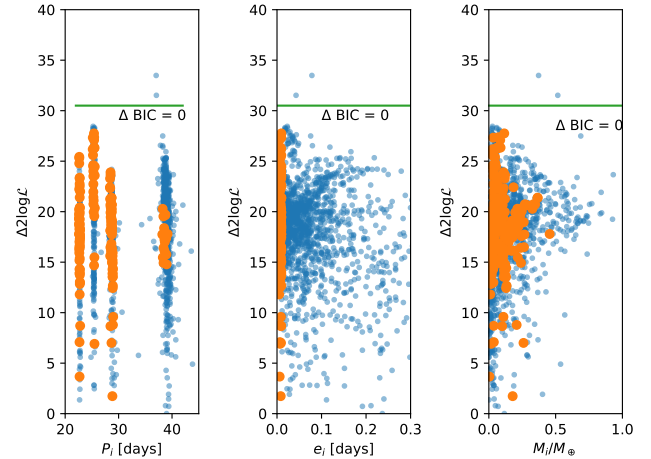


Figure 15. Limits on an eighth planet, "i", for a search near the periods in table 8. The 8-planet models are only plotted if they led to an improvement in log likelihood. Only two of the optimized likelihoods reach the difference in BIC > 0 indicated on the plots; however, these two cases have an eighth planet with a relatively large eccentricity and are distant from a GLR with g and h. Orange points have eccentricities smaller than 0.01; light blue points have larger eccentricities.

(2018) to represent the rocky interior of all TRAPPIST-1 planets with a $1-\sigma$ range of Fe/Mg ratios consistent with local stellar abundances; (2) the Earth-like value of $\text{Fe/Mg} = 0.83$ (Lodders et al. 2009); and (3) a core-free model with Earth-like refractory ratios, but in which all of the iron is oxidized in the mantle (Elkins-Tanton & Seager 2008). Rocky interiors are calculated using the models of Dorn et al. (2016). We have also added the theoretical mass-radius relationships for planets endowed with a water layer, both for planets which are irradiated less (blue line; water) and more (orange lines; steam) than the runaway greenhouse irradiation threshold (Turbet et al. 2020).

The comparison of measured masses and radii with theoretical mass-radius relationships reveals several striking results. First, all seven TRAPPIST-1 planets appear to be consistent with a line of interior isocomposition. There are multiple theoretical mass-radius curves that overlap with all seven planets' mass-radius probability distributions (Fig. 12), which may be a good indication that the composition varies little from planet to planet. Secondly, all of the TRAPPIST-1 planets have lower uncompressed densities than Solar System terrestrial planets. This likely means that the TRAPPIST-1 planets either have a lighter interior (e.g. lower iron content) or are enriched with volatiles (e.g. water).

We next searched for variations of density across the planets. For this, we normalized each planetary density calculated from 10^4 samples from the TTV/photodynamic posterior distribution by the local density of a fully differentiated 20 wt% iron, 80 wt% silicate (MgSiO_3) interior planet (Zeng et al. 2016), which is less iron rich than Earth. For each planetary density (i.e. each pair of mass and radius), the local density was taken to be that of the closest point on the theoretical mass-radius relationship of a 20wt% iron, 80 wt% silicate planet; we normalized each density by this value. Fig. 16 shows the resulting histograms of the posterior probability of the normalized TRAPPIST-1 planet densities. We then plotted in Fig. 17 the normalized densities (along with their 1σ uncertainty) as a function of the orbital periods of the planets. The normalized planet density appears very uniform across the seven planets, with

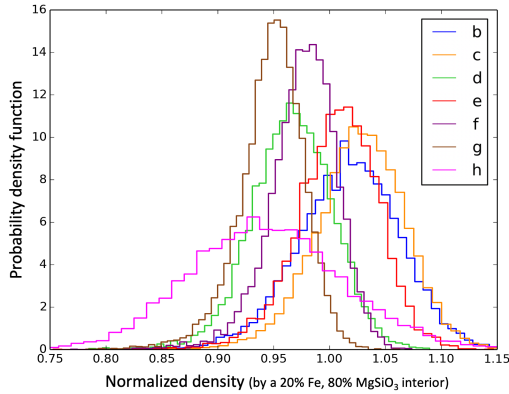


Figure 16. Probability density function of the normalized density of all seven planets in the system. The normalized densities were calculated by dividing the density of each pair of mass and radius of the TTV/photodynamic posterior distribution by the local density (i.e. of the closest pair of mass and radius) of a planet with an interior composition of 20 wt% iron and 80 wt% MgSiO₃. A planet with a normalized density of 1 has exactly the same density as a 20 wt% iron, 80 wt% MgSiO₃ planet. A normalized density >1 (or <1, resp.) is denser (or lighter, resp.) than a 20 wt% iron, 80 wt% MgSiO₃ planet.

perhaps a slight decrease with the increase of the orbital period (or the distance to the host star). We fit a line to the normalized density, y , versus orbital period, P , for 10^4 posterior samples, and found a relation of $y = (1.02 \pm 0.03) - (0.0045 \pm 0.0035)P$ where the coefficients are the 68.3% confidence interval. There is only weak evidence for a declining trend of normalized density with orbital period: 90% of the fits to the 10^4 posterior samples have slopes with a negative value, while 10% of the slopes fit have a *positive* value. If in the future more precise data strengthen this trend, then this indicates that either (i) the outer planets are depleted in heavy elements (e.g. iron) compared to the inner ones, or (ii) the outer planets are enriched in volatiles (e.g. water) compared to the inner ones. However, based on the current data we suggest that the planets compositions could be rather uniform in nature.

The interpretation of these observations in terms of internal compositions is discussed in more detail next.

9.2 Range of possible interior compositions and volatile contents

In this subsection, we discuss the range of possible compositions of the planets based on their measured densities, starting with a volatile-poor model in which the densities are fit by varying the core-mass fraction (§9.2.1), and followed by an analysis in which the solid planets are taken to have an Earth-like composition, to which is added a water fraction needed to create the observed densities (§9.2.2). Alternatively, the planets might be explained with an interior volatile content in which all of the iron is oxidized making the planets core-free (§9.2.3).

9.2.1 Core Mass Fraction

If we assume that the planets' atmospheres contribute a negligible amount to their total radius, and that the planets are fully differentiated, composed of rocky mantles (MgSiO₃) and iron cores only,

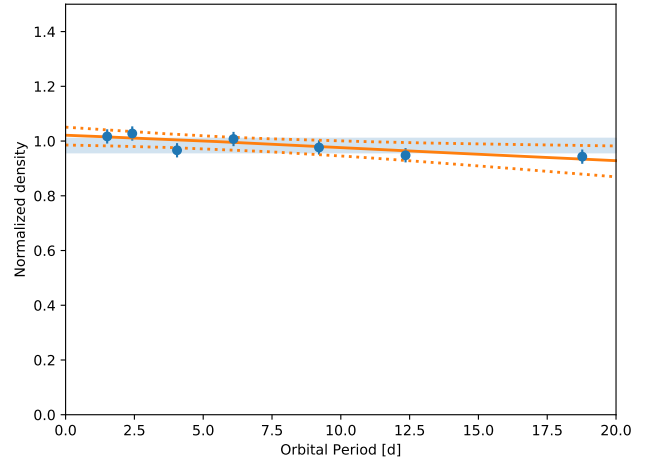


Figure 17. Normalized planet densities (with 1σ error-bars) versus planet orbital periods. The light blue band is the 68% confidence interval of the weighted mean normalized density of all seven planets. The orange lines show the 68.3% confidence intervals of linear fits to the normalized densities computed from 10^4 draws from the posterior. The mean fit to the normalized density versus period is $\rho_{\text{norm}} = aP + b$ where $a = 1.02 \pm 0.03$ and $b = -0.0045 \pm 0.0035$.

then the densities may be used to constrain the portion of the planets' mass which is contained within their cores.

We evaluated the core mass fractions of the TRAPPIST-1 planets as follows. For each mass/radius pair in our posterior distribution we have estimated the core-mass fraction by linearly interpolating between the mass-radius relationships of Zeng et al. (2016)¹¹. We arbitrarily set each mass/radius pair lighter than a pure silicate (MgSiO₃) planet to a CMF of 0. Alternatively, we repeated the same procedure but discarding all CMF values lower or equal to 0. However, we found that the estimate of the core mass fraction is only marginally changed (and only for planets g and h).

Our core mass fraction estimates are provided in Fig 18 and Table 9. Estimates range from 9^{+11}_{-9} wt% for planet h up to 22^{+5}_{-7} wt% for planet c, which, despite the different central values, have considerable overlapping probability distributions. Fig 18 shows that within the uncertainties, the CMF/iron fraction of the planets are very consistent with one another, with the mean of all planets of 17^{+3}_{-4} wt% (taking into account the correlations between the planets' core-mass fractions).

There may be a slight trend of the inferred CMF, which decreases with increasing orbital period. The trend is qualitatively similar to that reported on the normalized density (see Fig. 17), with similarly weak support: only 90% of the linear fits to the 10^4 posterior CMF values have a slope with orbital period which is negative, whilst 10% are positive.

9.2.2 Surface water content

The observed (weak) variation in the planet densities among all seven planets may instead be due to their differing volatile (e.g. water) inventories.

If we assume a rocky Earth-like interior and only allow an

¹¹ User-friendly data is provided on the personal website of Li Zeng (<https://www.cfa.harvard.edu/~lzeng/planetmodels.html>).

Planet:	b	c	d	e	f	g	h	Avg b-h	Avg b-e	Avg f-h
CMF [wt%]	22.3 ^{+6.85} _{-6.85}	24.3 ^{+5.1} _{-7.1}	14.2 ^{+6.1} _{-6.8}	20.7 ^{+5.8} _{-5.8}	16.2 ^{+4.4} _{-5.0}	11.2 ^{+4.7} _{-4.7}	9.3 ^{+11.4} _{-9.3}	17.2 ^{+3.4} _{-4.0}	20.6 ^{+4.5} _{-4.0}	12.6 ^{+4.8} _{-4.8}

Table 9. Core mass fraction inferred for each TRAPPIST-1 planet, as well as the weighted mean.

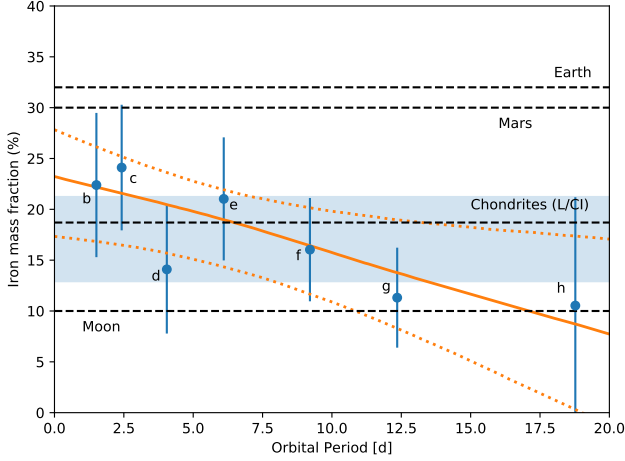


Figure 18. Iron core mass fraction versus the planetary orbital periods. The approximate values for Earth (McDonough 2014), Mars (Khan et al. 2018), the Moon (Barr 2016), and common chondrites (Palme et al. 2014) are indicated, as well as the 1σ confidence intervals of the TRAPPIST-1 planets. The light blue box is the 68.3% confidence region of the weighted mean of all seven planets. The orange lines show the median and 68.3% confidence interval for linear fits to the 10^4 posterior values for all seven planets.

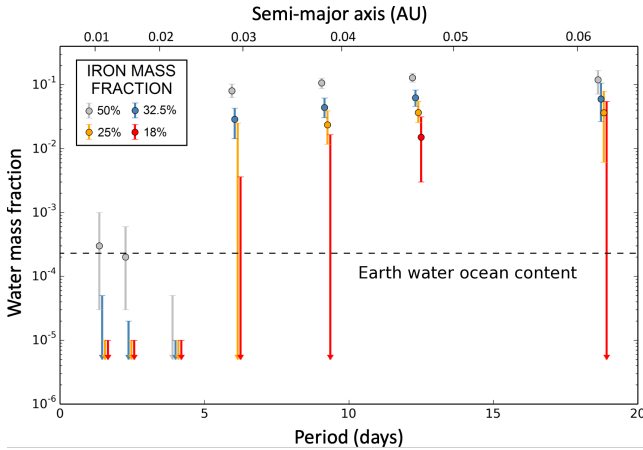


Figure 19. Theoretical water content (along with 1σ error bar) versus planetary orbital periods, for four distinct interior compositions (18, 25, 32.5 and 50 wt% iron content).

additional condensed¹² water layer to contribute to the total radius, we can estimate the water mass fractions of the seven planets (b: $2.8^{+2.0}_{-2.0}$ wt%, c: $2.1^{+1.7}_{-1.4}$ wt%, d: $4.6^{+2.1}_{-1.5}$ wt%, e: $2.9^{+1.4}_{-1.4}$ wt%, f: $4.4^{+1.8}_{-1.3}$ wt%, g: $6.2^{+2.1}_{-1.6}$ wt%, h: $6.0^{+4.4}_{-3.3}$ wt%). The lower densities

¹² Note that it is likely unwarranted to assume condensed surface water for the inner three planets given their location within the runaway greenhouse zone (Turbet et al. 2020).

of planets d, f, g, and h can allow for two to three times as much water than for planets b, c, and e. For this simple estimate we assumed a water layer with a surface temperature of 300 K at 1 bar.

Actual surface conditions can, however, lead to much larger differences in the estimated water budgets between the inner three and outer four planets. This stems from the fact that the inner three planets are more irradiated than the runaway greenhouse irradiation limit (Kopparapu et al. 2013; Wolf 2017; Turbet et al. 2018) for which all water is vaporized, forming a thick H_2O -dominated steam atmosphere. Taking into account the expectation that water should be vaporized for the three inner TRAPPIST-1 planets (Turbet et al. 2019, 2020), their water mass fractions drop drastically to less than 0.01 wt%, i.e. more than several times lower than the water ocean mass fraction of the Earth.

Figure 19 shows the expected water mass fractions for each of the TRAPPIST-1 planets, and for four distinct interior compositions (18, 25, 32.5 and 50 wt% iron content). It shows that the same trend of water versus orbital period is relatively robust across a large range of assumptions on the interior composition thanks to the transition from runaway greenhouse for planets b-d to surface liquid water for planets e-h. Note that the 18 wt% interior only requires a non-zero water fraction for planet g; as shown above, a 17 wt% iron core is consistent with all of the planets to 1σ confidence.

Higher estimated water budgets for the outer three or four planets could be a clue that they formed beyond the water condensation line at ≈ 0.025 AU (Unterborn et al. 2018). This could also be due to the significant differences in water loss (through atmospheric escape) arising from variations of irradiation and gravity among the TRAPPIST-1 planets (Lissauer 2007; Bolmont et al. 2017; Bourrier et al. 2017). However, again, we caution again that trends in the planetary volatile content are only weakly supported by the current data.

9.2.3 Core-free planets

Given that the data may be consistent with iso-composition mass-radius relation, we next consider another intriguing possibility: that the volatiles are contained entirely in the interior of the planets. For example, if, instead of forming a core, all of the iron is oxidised and remains in the mantle, the size of a planet may increase by a few percent (Elkins-Tanton & Seager 2008). This turns out to be about the amount of radius inflation necessary to match the TRAPPIST-1 planets when compared with our Solar system planets.

If we assume that the refractory ratios match a Solar composition, and that all seven planets lack an atmosphere, then it turns out that all seven planets are consistent with a core-free, oxidized composition (Fig. 12; magenta line). For this model the bulk mass abundances ratios for Fe/Si/Mg/O are 29.2/17.3/15.3/38.2 wt%, which is a significant increase in Oxygen compared to the bulk Earth with 29.7 wt% (McDonough 2014). Such a scenario would likely require formation of the planets at large distances from the star in a highly oxidizing environment (Elkins-Tanton & Seager 2008) and a lower devolatilization temperature intermediate between that of Earth and chondrites (?). Hence, although this hypothesis efficiently explains the TRAPPIST-1 data, it remains to be seen whether a geochemical

model can be constructed which results in high oxidation of iron throughout the processes of planet formation and evolution.

10 DISCUSSION

Here we discuss some of the implications of the results in the foregoing sections.

10.1 Timing uncertainties

As reported in §3, the transit timing measurements we have made show an excess of outliers with respect to the measurement uncertainties of each transit. We were unable to identify a culprit (or culprits) for these discrepancies, but wish to speculate on what may be the origin of these outliers. The cumulative distribution of these outliers (Fig. 1) indicates that about 10% of transits are affected at some level. It is also interesting to note that the core of the distribution has a slightly smaller width of about 80% of the measurement errors, indicating that for about 90% of the transits, the uncertainties may be overestimated. This may be a consequence of inflating the uncertainties to account for correlated noise rather than modeling the data with, for example, a Gaussian process; further re-analysis of the data will be needed to check this hypothesis.

Could the timing outliers be due to stellar flares? In [Vida et al. \(2017\)](#) and [Ducrot et al. \(2020\)](#), the frequency distribution of stellar flares is shown to be rising towards smaller flare energies. This could mean that the more frequent, but lower energy flares, occur at a level that is swamped by the photon noise, and thus not visible to an observer. We used the spectrum and energy calibration of Spitzer flares measured by [Ducrot et al. \(2020\)](#) to extrapolate the frequency of lower energy flares (which are not detected in Spitzer due to photon noise). As an example, for planet h the transit time can be affected by a flare which occurs at ingress or egress (duration $2\tau \approx 10$ min). We estimate that a flare of energy 10^{31} erg could cause a $1.5\text{-}\sigma$ timing outlier if it occurs during ingress or egress. This has a probability of only $\approx 0.3\%$ to occur during the 10 minutes of ingress or egress, and thus cannot be responsible for 10% of outliers for planet h. We carried out a similar estimate for the other planets, and we conclude that low-level flaring activity cannot be the cause of the timing outliers.

Other possible causes of the timing outliers are correlated stellar variability, star spots, or instrumental systematics. We don't yet have an estimate of the magnitudes of these effects, and so cannot reach a conclusion about where the origin of the timing outliers lies.

10.2 Planet masses and radii

In our current analysis of the transit-timing data for TRAPPIST-1, we have found larger mass ratios for all planets save planet e compared with our most recent analysis in [Grimm et al. \(2018\)](#). Even though most of the planets have shifted by $1\text{-}\sigma$ or more, this does not indicate that the prior analysis was in error. In fact, the masses of all of the planets are strongly correlated, and thus when one planet shifts in the transit-timing solution, they all shift. With the more extensive dataset analyzed here, we provide a better constraint over the transit-timing timescale, and can also better account for outliers thanks to some redundancy in our measurements, and thus we expect that our current analysis may remain the most reliable constraint upon the masses of the planets until the transit times can be measured with JWST.

In Figure 20 we compare the measured uncertainties for the

seven TRAPPIST-1 planets with our Solar System planets and with exoplanets with radii $< 1.7R_{\oplus}$ and masses measured to $> 5\text{-}\sigma$ retrieved from the NexSci database on 26 Feb 2020 ([Akeson et al. 2013](#); [Christiansen 2018](#)), as well as planet parameters reported in [Dai et al. \(2019\)](#) and Kepler-93b from [Dressing et al. \(2015\)](#).¹³ The uncertainties on the other planets' masses are the best available to date from radial-velocity measurements, and yet they are much larger than the uncertainties for the TRAPPIST-1 planets, whether considered in a relative or absolute sense. The larger uncertainties of the RV planets makes the core-mass fractions difficult to constrain for these more massive planets - core-free and cored models are consistent with most of these planets' parameters at the $1\text{-}\sigma$ level (Fig. 20). Nevertheless, it is notable that the rocky planets for which we currently have data look very similar in composition to the Earth, strengthening the assertion that rocky planets tend to form with a very narrow range of properties ([Dressing et al. 2015](#)). This also appears consistent with the observation that the evaporation valley requires rocky planets and their gaseous brethren to have a composition which is a mix of silicates and iron ([Owen & Wu 2017](#)).

10.3 Comparison with radial velocities

Given the measurements of the masses we have made with transit-timing, this begs the question: what radial-velocity precision would be required to make the same mass measurements?

The precision of the mass measurements may be placed in context by comparing with current radial-velocity capabilities. The predicted semi-amplitudes for the seven planets are given in Table 10. The predicted radial-velocity variation of the star induced by the TRAPPIST-1 planets is plotted in Figure 21, also based upon our mass measurements from transit timing. The sums of the semi-amplitudes of the planets equals ≈ 12.7 m/sec, which is close to the peak amplitude when the planets are all orbiting on the same side of the star (near 218 days in the plotted figure). How does this compare with current RV measurements?

Recently [Hirano et al. \(2020\)](#) were able to make high precision measurements of the radial velocity of the TRAPPIST-1 host star, achieving a constraint on the linear variation of the star to a precision of 2.5 m/sec (although they interpret this variation as being due to intrinsic stellar variability). To compare this with our transit-timing results, the semi-amplitude precision which would be needed to achieve the same mass error bars that we have achieved with transit-timing ranges from 2.4-19 cm/sec, over 100 times more precise than the radial-velocity measurements. Future observations may be able to achieve higher precision radial velocity measurements of TRAPPIST-1, but will also have to contend with stellar systematic variability ([Klein & Donati 2019](#)).

Were these planets orbiting a Sun-like star, the semi-amplitude measurement precision with radial-velocity would be even more stringent to achieve the same mass precision we have achieved with transit timing. Table 10 lists what semi-amplitudes precisions would be required if each one of these planets was placed around a Solar twin at one astronomical unit. The required precision range from 1-6 millimeters/second. This is nearly two orders of magnitude more precise than the highest precision radial velocity measurements for short-period exoplanets reported to date, such as Tau Ceti g, which has a reported RV semi-amplitude precision of 11 cm/sec ([Feng et al. 2017](#)).

¹³ Note: Kepler-105b has been corrected for a GAIA DR2 revised radius of the host star (cite: Berger & Huber and/or Petigura & Fulton).

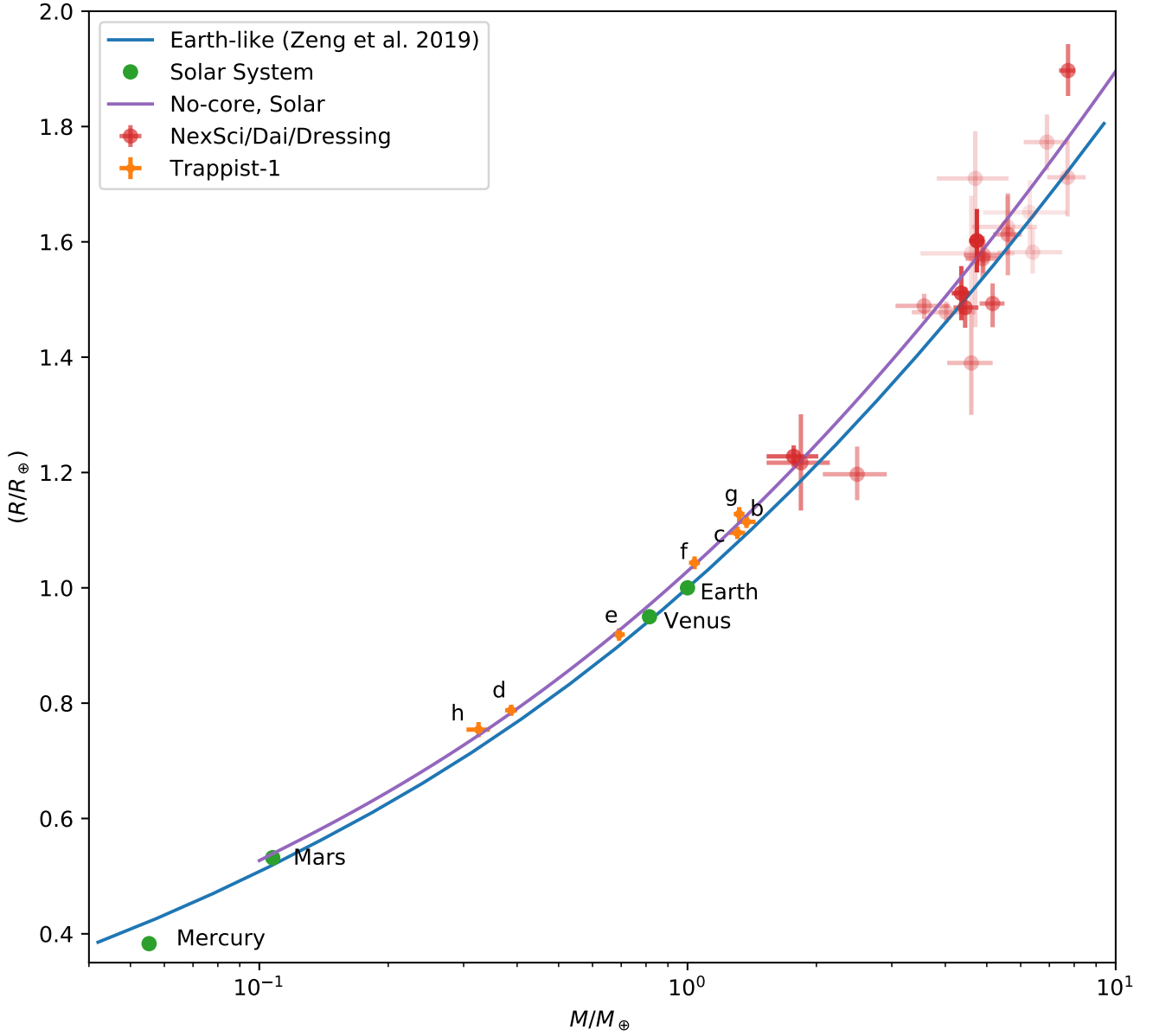


Figure 20. Radius versus mass for Solar-System terrestrial planets (green dots), TRAPPIST-1 (orange error bars), and other potentially rocky exoplanets from the NExSci database, Dressing et al. (2015), and Dai et al. (2019) (red error bars). Planets with smaller mass uncertainty are shown in a darker red color. Also plotted is a mass-radius relation with a core-mass fraction compatible with Earth (blue), and a core-free model in which the refractory elements retain the Solar abundance ratios (purple).

Planet	b	c	d	e	f	g	h
K_p [cm/sec]	382.0	310.7	77.6	120.7	158.1	182.2	39.1
RV equivalent precision for TRAPPIST-1 host [cm/sec]	19	13	2.5	3.8	4.7	5.2	2.4
RV equivalent precision for 1 M_\odot host at 1 AU [cm/sec]	0.62	0.50	0.11	0.20	0.28	0.34	0.18

Table 10. RV semi-amplitudes, K_p , for the TRAPPIST-1 planets predicted from our measured masses. Equivalent RV precision required to measure the masses to the same precision as measured with TTVs around TRAPPIST-1. Also, equivalent RV precision required *if* each planet were placed around a Solar twin at one astronomical unit.

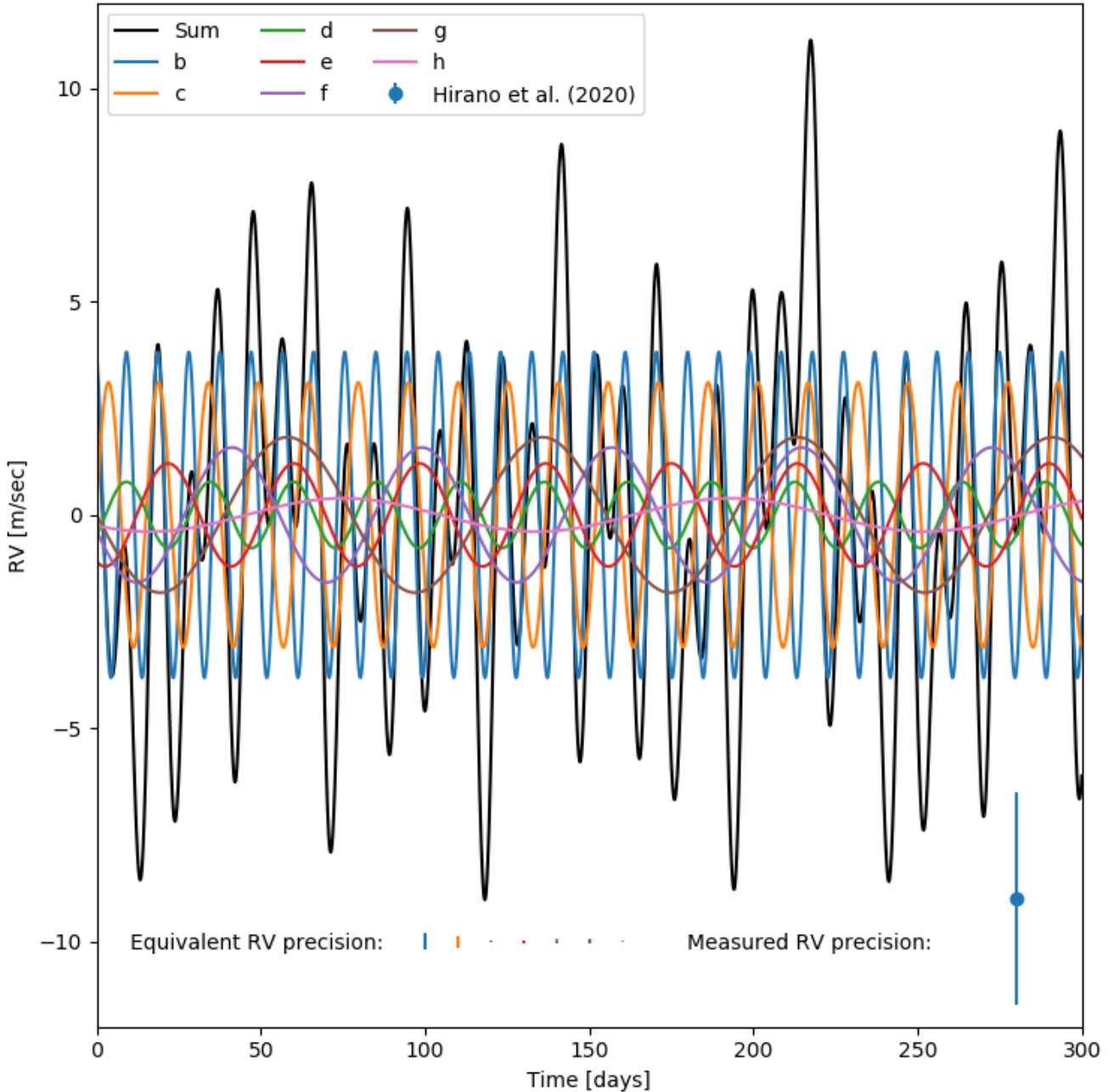


Figure 21. Predicted radial-velocity variation of the TRAPPIST-1 host star induced by its seven known transiting planets, as well as the current measurement error bar reported by [Hirano et al. \(2020\)](#), which they interpret as an upper limit, thanks to stellar variability. Also plotted are the equivalent semi-amplitudes for the seven planets which would be required to achieve the same mass precision as measured with TTVs.

10.4 Possible systematic errors

In this section we consider possible factors which might affect our inference of the densities of the planets. Simulated planetary densities predict core-mass-fractions which are similar to Earth, with a very small scatter ([Scora et al. 2020](#)). Hence, the fact that the TRAPPIST-1 planets have inferred planetary densities which are less than this could be due to systematic uncertainties which are not captured by our modeling.

The transit depths determine the radius-ratios of the planets

to the star, but these measurements are affected by the lack of uniform surface brightness of the star. Fortunately the multiple impact parameters of the planets yield a constraint upon the infrared limb-darkening, which is fairly weak compared with optical bands. However, star-spots can also affect the inferred transit depths ([Rackham et al. 2018](#); [Kipping 2012](#)). If spots are present on an active latitude which is not on the same hemisphere as the planetary transit chords, this can cause all of the planet radii to be mis-inferred by a similar factor.

TRAPPIST-1 may have complex surface inhomogeneities, in-

cluding regions brighter or darker than the mean photosphere (Morris et al. 2018b; Wakeford et al. 2019). It is possible that bright or dark regions could bias the apparent transit depths towards larger or smaller measurements, depending on which type of inhomogeneity dominates. We revisited the photodynamic simulations with a contamination parameter, ε , such that the effective transit depth (neglecting limb-darkening) is given by $(R_p/R_*)^2(1 - \varepsilon) + \varepsilon$ (Morris et al. 2018a,c). Re-running the Markov chains including ε as a free parameter in our fits, we find that $\varepsilon = 2 \pm 13\%$ at 68.3% confidence. Note that ε is assumed to be time-steady and to have the same value for all planets; in practice the value might vary between planets, say, if some traversed active latitudes. This constraint is not as tight as the analysis of planet b from Morris et al. (2018c), but our new constraint based on all seven planets does have a median value closer to zero. This indicates that from these data alone we cannot rule out a significant systematic error on the planets' radii caused by an inhomogeneous stellar photosphere. Improved constraints would likely require a wavelength-dependent analysis (e.g. Rackham et al. 2018; Wakeford et al. 2019).

Our mass precisions are predicated on a complete model of the dynamics of the system. Should an eighth planet be lurking at longer orbital periods, which has yet to reveal itself via significant transit-timing variations or transits, this may modify our timing solution and shift the masses slightly. In our timing search for an additional planet, however, we found that such a planet might only cause shifts at the $\approx 1 - \sigma$ level. This possibility begs for caution in interpreting the potential variation of iron fraction with orbital period: should an eighth planet be present beyond planet h, its timing impact would likely affect the masses of the exterior planets more significantly than the interior planets. Drawing stronger conclusions about the variation of planet iron/core mass fractions will likely require longer-term monitoring, especially of planet h, and/or higher precision timing measurements such as are expected with JWST.

10.5 Planetary dynamics

In this section we discuss some of the dynamical aspects of the planetary system: the eccentricities, the longitudes of periastron, and the GLR angles.

10.5.1 Eccentricities

The posterior distribution of eccentricities of the planets is shown in Figure 22. In prior analyses of the transit-timing variations of the TRAPPIST-1 system we found that the inner two planets, b and c, had significant eccentricities (Grimm et al. 2018). In the current analysis we find that the eccentricity probability distributions of these two planets are significant at zero eccentricity. This is consistent with N-body models which include tidal damping of the orbits, which predict that the planets should have low eccentricities, $\lesssim 10^{-3}$ (Luger et al. 2017a; Turbet et al. 2018). The other planets are all consistent with the predictions of the tidal evolution model (Luger et al. 2017b).

Figure 23 shows the posterior probability distribution for the eccentricity vectors of each planet. The only two planets consistent with zero eccentricity at 1- σ confidence are planets b and c (blue and orange contours). The other five planets have non-zero eccentricities.

Now, the eccentricity vectors plotted in Figure 23 show the values at the initial time. However, over time, the eccentricity vector of each planet can be decomposed into two components: the mean

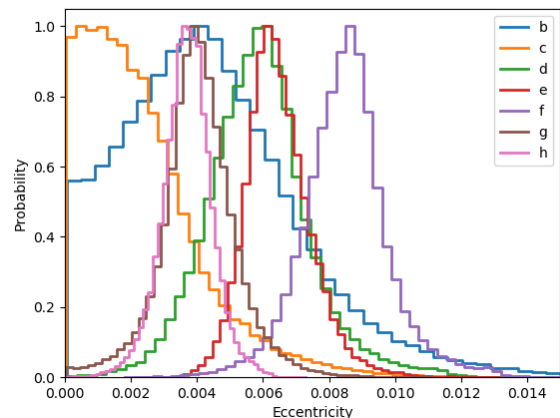


Figure 22. Probability distribution of the eccentricities of the planets at the initial time based upon the transit-timing model.

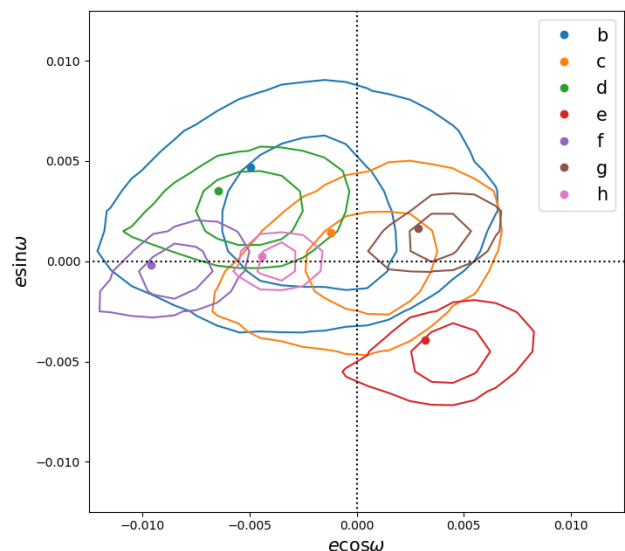


Figure 23. Posterior probability distribution for the eccentricity vectors at the initial time for each of the planets. Contours are 1- and 2- σ confidence limits. The maximum likelihood parameters are shown as solid points.

eccentricity vector (over some timescale) and the variable component (which is time variable, with multiple oscillation timescales driven by the mutual planetary perturbations). Figure 24 shows the eccentricity over a single oscillation for all seven planets. The outer five planets are close to first-order resonances with adjacent planets, and the super-period for each of these planets is close to 485 days thanks to the near GLR commensurability for all triplets of planets. This leads to a nearly circular oscillation over this timescale due to circulation of the first-order resonances driving oscillations in the eccentricity vectors of each of these planets. The inner two planets, b and c, are close to second and third order resonances with adjacent planets (b and c are close to 8:5, which is third order, while c and d are close to 5:3, which is second order). Since the strength of these interactions scales as a higher power of eccentricity, these planets show much smaller variation in the time-variable components of

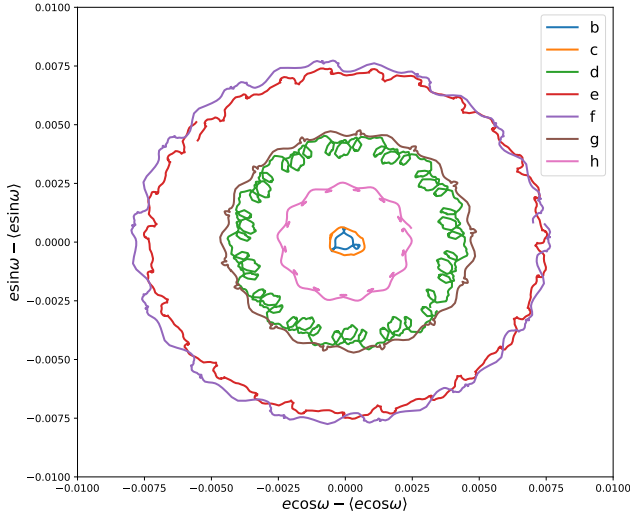


Figure 24. Variable component of the osculating eccentricity vectors plotted from a simulation over 12 days for planets b and c, and over ≈ 485 days for planets d-h, with initial parameters drawn from the posterior distribution.

their eccentricity vectors. Since planets b and c are close to a third order resonance, their eccentricity vectors show a three-fold symmetry. On longer timescales these patterns precess, filling a circular pattern over time. The time-variable eccentricity vector patterns are very similar over the range of posterior values, indicating that it is primarily this component which is constrained by the transit timing variations of the planets.

The total eccentricity vectors show a wider range of behavior, thanks to a wider variation of the mean eccentricity, as shown in Figure 25. It is clear from this figure that each planet executes an eccentricity-vector oscillation about a mean value (which was subtracted off for figure 24). Unfortunately the mean eccentricity is poorly constrained by the transit-timing variations, and so there is a much wider range of eccentricity vectors which is allowed.

10.5.2 Longitudes of periastron

The inner two planets, b and c, have an additional robust prediction from migration and damping: the longitudes of pericenter should be anti-aligned, or librate about anti-alignment.

Planets b and c are close to an 8/5 mean motion resonance, and planets c and d are close to a 5/3 mean motion resonance. These being third order and second order resonances, respectively, the resonance widths are approximately given by (Murray & Dermott 1999)

$$\frac{\Delta P}{P} = (12\mu\alpha|f(\alpha)|e^q)^{1/2} \quad (16)$$

where μ is the ratio of the perturbing planet's mass to the stellar mass, $\alpha = a_1/a_2 < 1$ is the ratio of planets' semi-major axes, $f(\alpha)$ is a coefficient of the resonant term in the interaction potential, e is orbital eccentricity, and q is the order of the resonance. For the resonances of interest here, we find that $\Delta P/P \lesssim 10^{-4}$. The observed period ratios are $\gtrsim 3 \times 10^{-3}$ wide of the exact resonance, i.e., more than 30 times the resonance width(s).

In these circumstances, the mean motion resonant perturbations are negligible, and the secular interactions of planets b and c provide a fair first approximation to their orbital dynamics. (We ac-

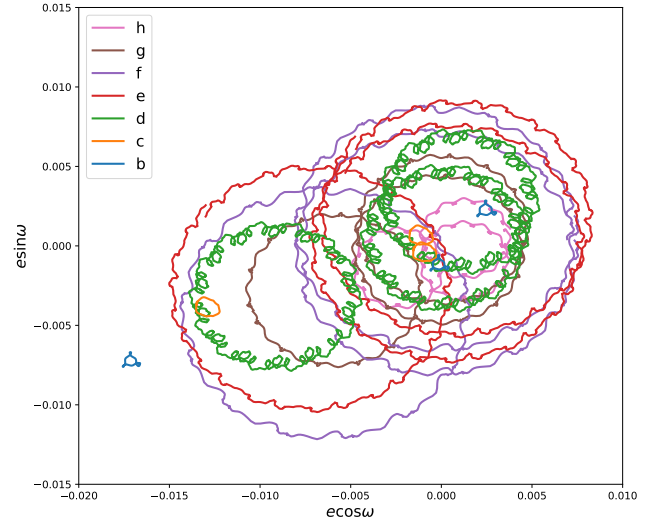


Figure 25. Osculating eccentricity vectors computed from a simulation for all seven planets shown for three different draws from the posterior: the first with eccentricities nearest the median of the posterior distribution; the second with eccentricities furthest from the median, and a third drawn randomly from the posterior. As with Figure 24, planets b and c are plotted over 12 days, while planets d-h are plotted over ≈ 485 days.

knowledge that in the following analysis we have neglected secular perturbations from the other planets in the system which will introduce some quantitative differences, not germane to the qualitative question of aligned or anti-aligned periastrons of planets b and c.) To leading order in the eccentricities, the orbit-averaged (secular) interaction potential of a pair of planets is given by

$$\begin{aligned} U^{(sec)} &= -\left\langle \frac{Gm_1m_2}{|\mathbf{r}_1 - \mathbf{r}_2|} \right\rangle \\ &\simeq -\frac{Gm_1m_2}{a_2} \left[\frac{1}{2}b_{1/2}^{(0)}(\alpha) + \frac{1}{8}b_{3/2}^{(1)}(\alpha)(e_1^2 + e_2^2) \right. \\ &\quad \left. - \frac{1}{4}b_{3/2}^{(2)}(\alpha)e_1e_2\cos(\varpi_1 - \varpi_2) \right], \end{aligned} \quad (17)$$

where $b_s^{(j)}(\alpha)$ are positive-definite Laplace coefficients. (We neglect post-Newtonian corrections to the potential, stellar oblateness, and stellar and planetary tides, all of which are negligible compared to the point-mass Newtonian gravitational interactions in the TRAPPIST-1 system.) It is evident from Eq. 17 that, in the secular approximation, the interaction energy is minimized when $\varpi_1 - \varpi_2 = \pi$, that is, when the periastrons are anti-aligned. Consequently, orbital energy dissipation (e.g., due to tides) is likely to evolve the innermost pair of planets, b and c, into anti-aligned periastrons as energy dissipation would tend to minimize the total orbital energy.

In more detail, we look to the secular variations for the eccentricity vectors, $(h_i, k_i) = e_i(\sin \varpi_i, \cos \varpi_i)$. With the leading order secular interaction potential, Eq. 17, the equations of motion for h_i and k_i are first order coupled differential equations with constant coefficients, which can be solved for $h_i(t), k_i(t)$ as a superposition of two linear modes (Murray & Dermott 1999). It can be shown that the faster mode corresponds to anti-aligned periastrons, while the slower mode corresponds to aligned periastrons. For general initial conditions, the solution is a linear superposition of the two secular modes.

Libration of the periastrons about the aligned state has been

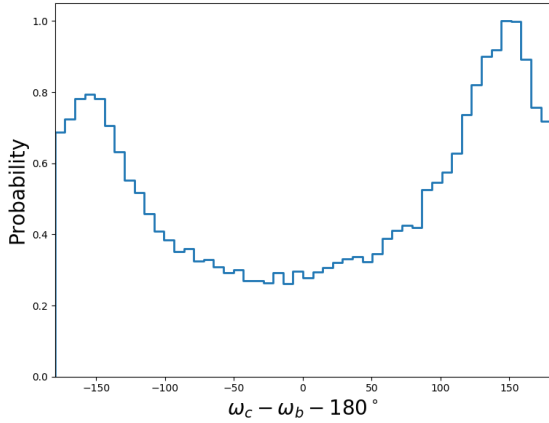


Figure 26. Difference in the longitudes of pericenter of planets b and c minus π .

observed for a pair of non-resonant planets in the ν Andromedae planetary system. Planets c and d in that system have substantial orbital eccentricities, ~ 0.2 – 0.3 . It has been suggested that eccentricity excitation of the outer planet of the pair would select the aligned mode (e.g. Chiang & Murray 2002; Malhotra 2002) as would a perturbing acceleration on the host star (Namouni 2005). In the case of the TRAPPIST-1 planets b and c, such mechanisms are not applicable as their eccentricities are very small.

In the case of TRAPPIST-1, Papaloizou et al. (2017) found that a model in which the TRAPPIST-1 planets underwent migration with damping, the inner two planets indeed end up with anti-aligned longitudes of pericenter.

Figure 26 shows the posterior probability distribution for $\omega_c - \omega_b - \pi$. The distribution has a similar probability at all angles due to the fact that both eccentricities are small, but favors *aligned* longitudes of pericenter. However, there is still a significant probability at anti-aligned angles (near zero in Fig. 26). We expect that the eccentricities of these two planets are poorly constrained as they are in proximity to higher order resonances, $P_c/P_b \approx 8/5$, while $P_d/P_c \approx 5/3$. The disturbing potential of a $j + k : j$ resonance has a dependence on eccentricity which scales as e^k (Deck & Agol 2016), and thus the low eccentricities of these planets only weakly affect the transit timing variations. Thus, at the current precision of the transit timing data, we can only place poor constraints on these planets' eccentricity vectors, and thus only poorly constrain the difference in longitude.

10.5.3 Laplace angles

A remarkable property of the TRAPPIST-1 system is the near-commensurability of adjacent triplets of planets (Luger et al. 2017b), akin to Laplace resonances, with GLR angles given by

$$\phi_{i,i+1,i+2} = p\lambda_i - (p+q)\lambda_{i+1} + q\lambda_{i+2}, \quad (18)$$

where λ_i is the mean longitude of the i th planet, and p and q are small integers. In the case of an isolated triplet of planets, a stable configuration takes on $\phi = 180^\circ$, but when planets are captured into

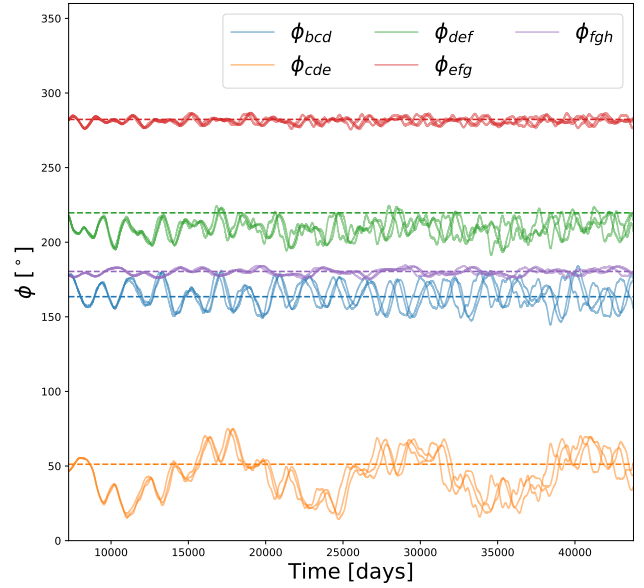


Figure 27. GLR angles plotted over 100 years for three draws from the posterior distribution: one with low eccentricities, one with high, and one randomly chosen. These are compared with the predictions from Mah (2018), shown by dashed horizontal lines, with the values for ϕ_{bcd} and ϕ_{cde} flipped about 180° (i.e. changed from ϕ to $360^\circ - \phi$).

a series of GLR commensurabilities, their mutual torques displace the stable configuration.

Long-term dynamical simulations show that these GLR angles can take on stable values for extended durations, and sometimes can quickly jump in value, flipping symmetrically about 180° (Mah 2018), resulting in two possible angles for each triplet of stars, ϕ and $360^\circ - \phi$. Based on the prior measured mass-ratios of the planets to the star, Mah (2018) predicted the value of the three-body resonance angles resulting from the values at the end of the simulation.

In Figure 27 we show the GLR angles for the following triples:

$$\begin{aligned} \phi_{bcd} &= 2\lambda_b - 5\lambda_c + 3\lambda_d, \\ \phi_{cde} &= \lambda_c - 3\lambda_d + 2\lambda_e, \\ \phi_{def} &= 2\lambda_d - 5\lambda_e + 3\lambda_f, \\ \phi_{efg} &= \lambda_e - 3\lambda_f + 2\lambda_g, \\ \phi_{fgh} &= \lambda_f - 2\lambda_g + \lambda_h. \end{aligned} \quad (19)$$

Differences between the predicted and observed angles agree within 0.5 – 10 degrees, where the predicted values for ϕ are taken from Mah (2018); Brasser et al. (2019), but allowing ϕ_{bcd} and ϕ_{cde} to be flipped about 180° . It is possible with the updated mass-ratios from our analysis that the predictions will be more accurate, which awaits further simulations.

10.5.4 Long-term stability

Prior studies of the TRAPPIST-1 system by Tamayo et al. (2017) found long-lived configurations for systems which had formed via migration. Quarles et al. (2017) examined the stability of the TRAPPIST-1 system, refining the large uncertainties from prior measurement (Gillon et al. 2017) to further constrain the masses of the system. Given the much tighter constraints we have placed upon the masses of the planets and the orbital eccentricities, here we re-examine the long-term stability of our posterior distribution.

planet	$\Delta\bar{a}$	$\Delta\bar{e}$	$\max(\Delta a)$	$\max(\Delta e)$
b	-6.52e-09	1.73e-04	7.12e-07	0.0020
c	-1.44e-08	1.62e-04	2.51e-06	0.0018
d	-1.06e-08	1.45e-05	4.07e-06	0.0009
e	2.05e-08	4.44e-05	8.53e-06	0.0008
f	2.45e-07	5.13e-05	3.00e-05	0.0012
g	8.24e-08	5.01e-05	2.19e-05	0.0011
h	-1.23e-07	2.11e-04	3.00e-05	0.0035

Table 11. Evolution of the semi-major axis a and eccentricities e from 10,000 samples over 10 Myr. For each sample and planet, the average of a and e over the first and last Myr, are compared. $\Delta\bar{a}$ and $\Delta\bar{e}$ are the differences between the first and the last Myr from the average values over all samples, while $\max(\Delta a)$ and $\max(\Delta e)$ are the maximal differences from the samples. The numbers show that all samples remain stable over 10 Myr.

We have used the GPU N-body integrator GENG (Grimm & Stadel 2014) to carry out long-term simulations of a set of 10^4 samples from the posterior probability distribution of the transit-timing analysis of the system. These simulations were carried out for 10^7 years, which corresponds to 2.4 billion orbital periods of planet b, and 2 million orbital periods of planet h. We used a time step of 0.06 days, which gives a total number of $6.1 \cdot 10^{10}$ integration steps. We find that 100% of these posterior samples are stable over this entire timescale. To check the stability of the samples, we analyzed the evolution of the semi-major axis a and eccentricity of all samples and planets. We compare the average values over the first Myr and the last Myr. In Table 11 are shown the averages over all samples and the maximal difference between the first and the last Myr.

These results suggest that the simulations could be stable even on a much longer time scale. More interesting than the evolution of the semi-major axis and the eccentricity, is the evolution of the five GLR resonant angles, shown in Figure 28. In order to describe the evolution of the GLR angles, we define three categories:

- Category I: remaining in GLR for 10 Myr, with a maximum difference to the initial value of less than 45°
- Category II: remaining in GLR for 10 Myr, with a maximum difference to the initial value of more than 45° . In this category, the GLR angles can jump between different states.
- Category III: not remaining in GLR for 10 Myr.

The threshold of 45° is chosen arbitrarily, but is found to be practical to distinguish simulations where the GLR angles jump between different states (Category II), or remain in the same state (Category I). Figure 28 shows the three different categories in different colors, as well as a histogram of all 10,000 simulations over 10 Myr for all five GLR angles. The exact number of simulations in the three categories are given in Table 12. The GLR angles from Planets b,c and d as well as Planets d,e,f show a unique resonant state. Planets c,d,e and Planets e,f,g have a dominant state and a subdominant state, while Planets f,g,h have a dominant state and two symmetric subdominant states. Our new samples show a better conservation of the GLR angles than was found in (Grimm et al. 2018), where the longest resonance time was found to be 2 Myr.

10.6 Forecasts for JWST

10.6.1 Forecast transit times

With the model we can forecast the probabilities of future transit times, and hence better help to plan transit observations with JWST. This is important for both optimizing the efficient use of

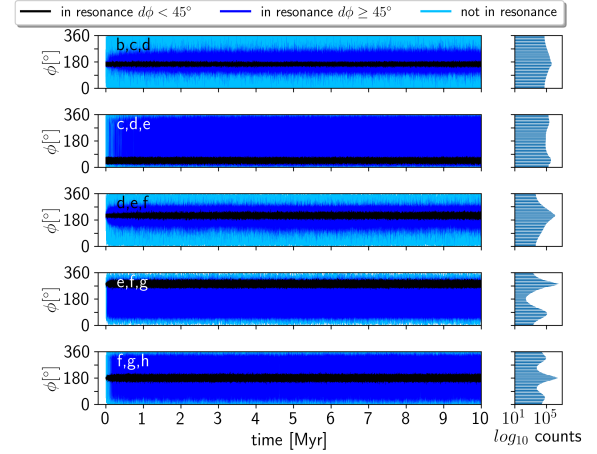


Figure 28. Evolution of the GLR angles ϕ for 10000 samples over 10 Myr. The simulations can be split into three categories: I remaining in resonance (black), II remaining in resonance but jump between states (dark blue), and III not remaining in resonance (light blue).

	bcd	cde	def	efg	fgh
Category I	130	178	755	7943	6462
Category II	1571	874	7653	1855	1578
Category III	8299	8948	1592	202	1960

Table 12. Number of posterior samples falling into the three resonant categories for the five GLR angles. The total number of posterior samples is 10000.

the telescope, and for determining when transits might overlap (i.e. two or more planets crossing the face of the star at the same time). This is especially important for transit transmission spectroscopy as the signal will be small, and hence many transits may need to be observed. With the observation of initial transits with JWST the ephemerides can be refined/updated; however, our current forecasts provide the starting point for planning JWST observations.

Table B3 gives our forecast for upcoming times of transit through September, 2022 to cover the first 1.5 years of JWST (through the end of Cycle 1, given the present launch date of March 2021).

10.6.2 Simulated JWST TTV analysis

Based on the measured properties of TRAPPIST-1, we have carried out a preliminary analysis forecasting future transit observations with the James Webb Space Telescope. Already there are several JWST Guaranteed Time Observation (GTO) programs which plan to observe the TRAPPIST-1 planetary system, primarily for the purposes of spectroscopic characterization (GTO programs 1177, 1201, 1279 and 1331).¹⁴ It is very likely that additional observations will be scheduled during guest observing time throughout the duration of the JWST mission as the detection of spectroscopic features requires observations of multiple transits for each of the planets (Morley et al. 2017; Barstow & Irwin 2016; Lustig-Yaeger et al. 2019; Fauchez et al. 2020). An effort to coordinate these

¹⁴ For specifications of these programs, see <https://www.stsci.edu/jwst/observing-programs/approved-gto-programs>.

observations amongst the exoplanet and planetary science communities is underway via the TRAPPIST-1 JWST Community Initiative (Gillon et al. 2020). All to say, long-term studies of TRAPPIST-1 for spectroscopy will also yield transit times for each transit observed, enabling a transit-timing analysis of the results.

To estimate the *maximum* possible precision of observations with JWST, we have simulated a five-year program in which *every* transit of every planet in TRAPPIST-1 is observed with NIRSPEC. The NIRSPEC instrument was chosen as its prism mode covers 0.5-5 microns, covering the peak of the SED of the star, and thus maximizing the number of photons detected, which is about two orders of magnitude per transit greater than collected by Spitzer. Although such a complete set of transits will be impossible to collect (thanks to limits due to scheduling and time-allocation), this analysis yields an estimate of the most optimistic results we might expect from JWST.

We have carried out simulations of transits of each of the planets as observed by NIRSPEC. We include realistic estimates of photon noise and correlated stellar variability based on the pattern of variations detected with the Spitzer Space Telescope, using a Gaussian Process model created with *celerite* (Foreman-Mackey et al. 2017). We do not include instrumental systematics under the assumption that over the timescales of ingress/egress, which are what limit the timing precision, that the noise contribution will be dominated by photon noise and stellar variations. From these simulations, we next found the posterior probabilities of the transit times. We found that the posterior timing precision ranges from 0.5-1 second per transit, much more precise than the measurements reported in the present paper.

Next, we created a simulated set of transit-timing observations at the two windows each year when the TRAPPIST-1 system is observable with JWST (Figure 29). For each transit time, we drew the time from the distribution of uncertainties from the posteriors of the simulated transit data. We did not include the presence of outliers in our analysis as we do not currently understand the origin of the outliers in our present data (and there is some hope that JWST will provide a stable platform for transit observations, and that the large number of photons collected with JWST over a range of wavelengths might enable the identification and removal of astrophysical sources of correlated noise).

Finally, we utilized our code for transit-timing analysis to optimize a plane-parallel model with seven planets. At the maximum likelihood of the fit, we computed the Hessian to estimate the uncertainties on the model parameters. Figure 29 shows the simulated transit-timing observations with JWST. This includes about 600 transits observed with the telescope (again, the maximum possible over the nominal 5-year JWST mission). Figure 30 shows the results of the mass measurements in the simulations. We find that the masses can be recovered to better than 0.02% for planets d-h, and to 0.05% for planets b and c.

Of course, it will be impossible to arrange such a large number of transit observations of this system. But, even if the number of observations is an order of magnitude smaller, we expect that the noise should scale with the square root of the number of measurements made, and thus most of the planets will still have mass measurements precise to the order of a part-per-thousand.

10.7 Stellar parameters

The stellar density we derive using the photodynamic model, $\rho_* = 53.17^{+0.72}_{-1.18}\rho_\odot$, is moderately higher and more precise than prior analyses. Most recently, Delrez et al. (2018b) found a density of

$\rho_* = (52.3 \pm 2.2)\rho_\odot$, twice as uncertain as our analysis. We feel that our approach yields a density of superior precision due to several factors. The transit times in the Spitzer data are constrained by *all* of the measured transits in the photodynamic model so that fewer degrees of freedom are needed to fit the times (37 free parameters in the N-body model versus 447 transit times fit to each transit).

The stellar mass we take from the analysis by Mann et al. (2019), $M_* = 0.0898 \pm 0.0023M_\odot$.¹⁵ This mass has a precision of 2.6%, which limits the mass precision for several of the planets. We are at the point that to improve the mass measurements of the planets we will need to improve the measurements of the star.

We used the luminosity estimate from Ducrot et al. (2020), which is slightly lower than that estimated by Gonzales et al. (2019) due to a difference in the measured bolometric flux. We are consistent with Gonzales et al. (2019) for the reported value of $R^2T_{eff}^4$ at 1σ , while our T_{eff} is more precise (28 K vs 42 K), R is 2.5 times more precise, and our $\log g$ is more precise by an order of magnitude.

11 CONCLUSIONS

The Spitzer discovery of seven transiting planets orbiting the TRAPPIST-1 star by Gillon et al. (2017) promised the determination of the interior compositions of these planets via dynamical analysis. We have now analyzed the complete set of transit time measurements of the TRAPPIST-1 planets from Spitzer, augmented by additional transits from the ground, K2, and HST. Our primary conclusions are:

- (i) We have measured the masses, radii and densities to high precision, 3-6%, based on an N-body model with seven planets. This improves upon RV constraints by two orders of magnitude.
- (ii) The pattern of masses and radii is consistent with a uniform planetary composition for all seven planets which have lower uncompressed densities than the Earth, Mars or Venus, with weaker evidence for a declining normalized density with orbital period (90% confidence). The planet properties may either be consistent with a core mass fraction of 17 ± 4 wt%, or an Earth-like core and mantle with a volatile content which varies from $<0.01\%$ for the inner three planets to $\approx 5\%$ for the outer four, or core-free planets with highly oxidized iron in the mantle which elevates the interior volatile content. These are not unique explanations.
- (iii) The planets appear to be dynamically-cold, with eccentricities lower than $\approx 1\%$, and inclinations which are coplanar to a fraction of a degree.
- (iv) The system is stable on long timescales, and shows a pattern of generalized Laplace resonances with angles which match predictions from migration simulations of Mah (2018).
- (v) We provide a forecast of the future times of transit for the planets (Table B3) to help in planning observations with JWST, which may yield more precise constraints upon the planets' masses.
- (vi) We have yet to find strong evidence for an eighth planet.

Based upon these properties, we next speculate on some possible scenarios for the formation and evolution of the system.

¹⁵ https://github.com/awmann/M_-M_K-

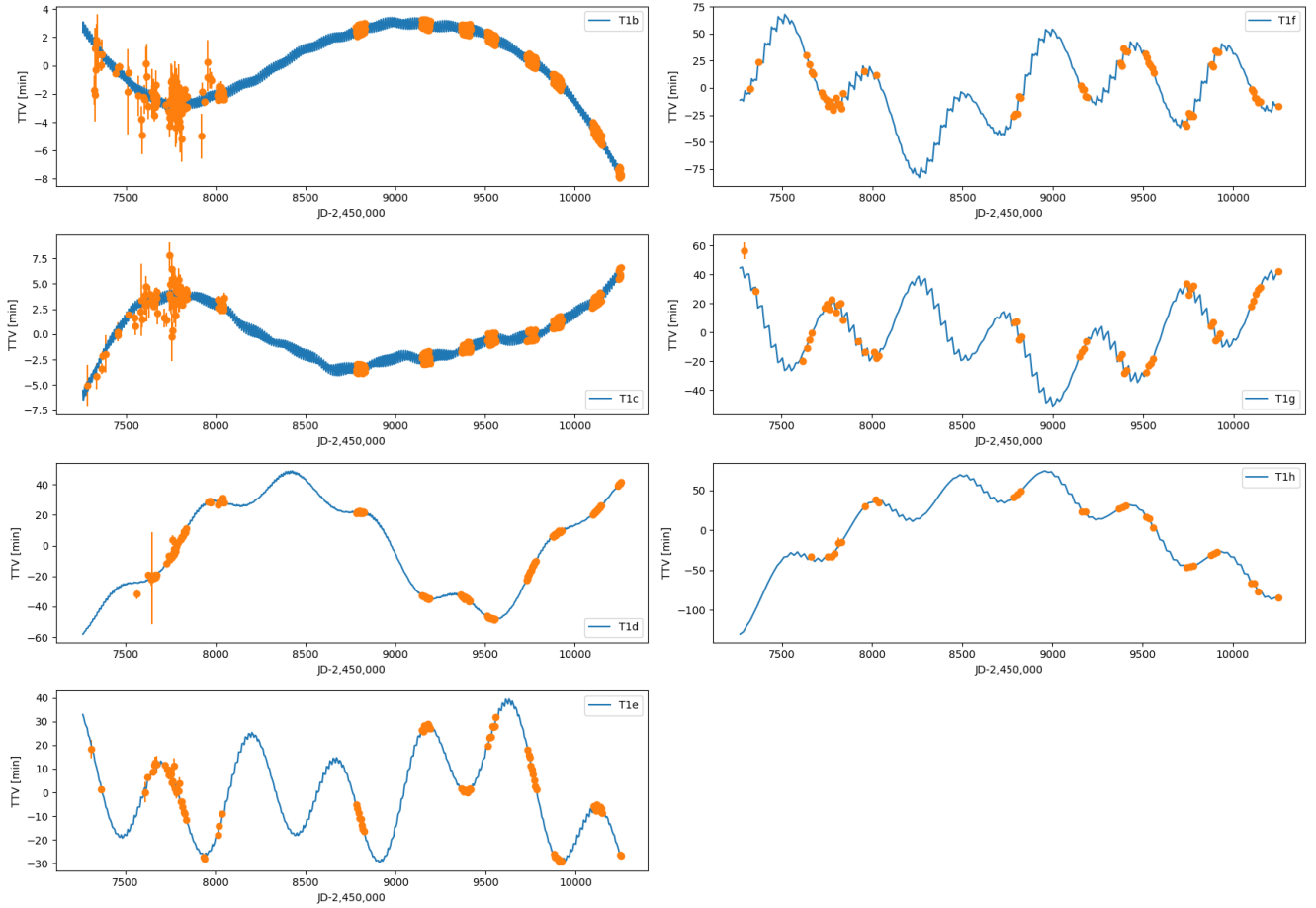


Figure 29. Simulated observations of all of the transits of TRAPPIST-1 detectable with JWST. Each transit has an uncertainty of $\approx 0.6 - 1.7$ seconds, assumed to be observed with NIRSPEC (which maximizes the number of photons collected of any JWST instrument). From retrieval, we obtain $\lesssim 0.1\%$ mass precision.

11.1 Expectations for the compositions of the TRAPPIST-1 planets from formation scenarios

As mentioned, our analysis suggests that the TRAPPIST-1 planets have somewhat lower uncompressed bulk densities than Earth (see Table 6 and Fig. 12). It is possible that these lower densities result from a deficit of high-density material (e.g., less iron) relative to Earth, or an excess of low-density material (e.g., having more water), or both; in this section we speculate about formation scenarios which may be consistent with these planets' bulk densities.

In general, planets which formed within the same protoplanetary disk have similar budgets in relative refractory elements (Bond et al. 2010; Elser et al. 2012) but can have very different volatile element budgets (Öberg & Bergin 2016). Similar relative refractory elements (Fe, Mg, Si) implies similar core mass fractions for all seven planets, assuming full differentiation. As suggested by Dorn et al. (2018), the refractory composition may best be described by studying the densest planet of the system, planet c with 17-30% CMF. Thus, with this assumption, all of the planets may likely have a 17-30% CMF but different volatile mass fractions (that may increase slightly with orbital period, Fig. 19).

Is an overall CMF of 17-30% realistic for terrestrial planet interiors? This range of CMF implies lower Fe/Mg and Fe/Si values compared to Earth (and the Sun). Elemental abundances of rocky interiors are expected to be reflected in the photospheric abundance

of the host star as argued by Unterborn et al. (2018) and Dorn et al. (2018). Unfortunately, measuring the photospheric abundances of this cool and active host star remains very challenging. However, Unterborn et al. (2018) estimated the stellar Fe/Mg number ratio to be 0.75 ± 0.2 by analysing Sun-like stars of similar metallicity to TRAPPIST-1, which may be slightly lower than the Solar value. The corresponding mass-radius curve for a rocky interior of this range of Fe/Mg value is plotted in Figure 12 (brown curve and shaded region). It overlaps well with the densest planets c and b. This means that the expected range of stellar abundances supports a possible overall CMF value of 17-30%, assuming full differentiation.

Could there be a variation of Fe/Mg ratios among the planets? Rocky planet accretion should preserve the integrated iron/rock ratio. Consider a population of planetary embryos and planetesimals that accrete into a system of rocky planets. Giant collisions between growing planetary embryos can change the iron/rock ratios of individual objects by preferentially stripping the outer, rock-dominated layers from differentiated embryos (e.g. Benz et al. 1988; Marcus et al. 2010; Asphaug & Reufer 2014). But from a system-wide perspective, it is a zero-sum game unless rock or iron is preferentially lost from all of the planets. Rock is the major component of loosely-bound impact debris and more likely to be lost either by differential aerodynamic drag (Weidenschilling 1977) or solar wind drag (Spalding & Adams 2020), and so the integrated iron/rock

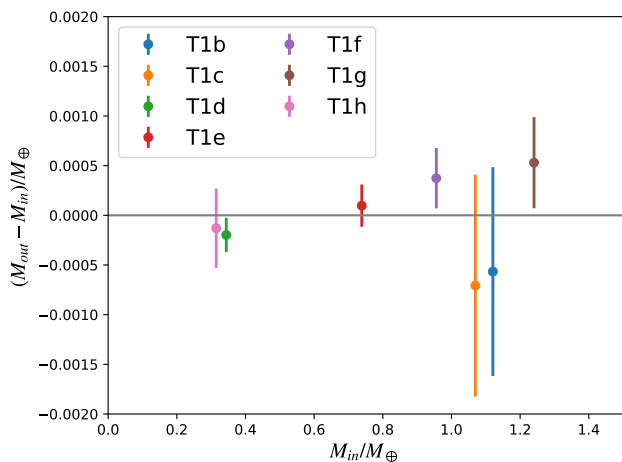


Figure 30. Simulated planet masses based on 5 years of JWST observations of every TRAPPIST-1 transit with NIRSPEC. The recovered minus the input mass versus the input mass. The masses can be recovered to better than 0.1% precision. [This figure needs updating]

ratio should only increase. Hypothetical variations in Fe/Mg can otherwise be caused if large portions of planetary building blocks condense at different high temperatures (>1200 K). During planet formation, such temperatures are only reached in a tiny region very close to the ultracool dwarf star. Consequently, both [Unterborn et al. \(2018\)](#) and [Dorn et al. \(2018\)](#) have assumed that all seven planets have similar refractory element ratios (i.e., Fe/Si, Fe/Mg).

Now let us instead suppose that the TRAPPIST-1 star has similar refractory abundance ratios as our Sun. Looking to our Solar system for analogs, this still implies an iron content which is far lower than Earth's, but may be more comparable to that of carbonaceous chondrite meteorites which have similar refractory abundances as Earth, but a higher volatile content, primarily in oxygen.

Carbonaceous chondrites may also be an appropriate analog for the compositions of the TRAPPIST-1 planets from a formation perspective. Planetesimals are thought to form preferentially just past the (evolving) snow line ([Armitage et al. 2016](#); [Drążkowska & Alibert 2017](#); [Schoonenberg & Ormel 2017](#)). Carbonaceous chondrites are spectrally associated with C-type asteroids ([Bus & Binzel 2002](#); [Burbine et al. 2002](#)), which are predominantly located in the outer main belt ([Gradie & Tedesco 1982](#); [DeMeo & Carry 2013](#)). Dynamical models suggest that carbonaceous chondrites were implanted from the Jupiter-Saturn region into the asteroid belt during the giants' growth and migration ([Walsh et al. 2011](#); [Raymond & Izidoro 2017](#); [Ronnet et al. 2018](#); [Raymond & Nesvorný 2020](#)). They are therefore likely to represent the compositions of the cores of the giant planets.

Orbital migration was a key ingredient in the assembly of the TRAPPIST-1 system ([Tamayo et al. 2017](#); [Ormel et al. 2017](#); [Papaloizou et al. 2017](#); [MacDonald & Dawson 2018](#); [Coleman et al. 2019](#)). Chains of orbital resonances are a signpost of migration ([Cresswell & Nelson 2008](#), e.g.). Models which invoke long-range migration can match the orbital spacing of the population of super-Earth systems ([Izidoro et al. 2017, 2019](#)). These models propose that resonant chains are ubiquitous but that most are destabilized during or after dissipation of the gaseous disk ([Terquem & Papaloizou 2007](#); [Ogihara & Ida 2009](#); [McNeil & Nelson 2010](#); [Cossou et al. 2014](#)). The first planetary embryos massive enough

to migrate are likely to form just past the snow line because of the increased efficiency of planetesimal formation and pebble accretion ([Lambrechts & Johansen 2014](#); [Ormel et al. 2017](#)). A model based on this assumption can match the orbital structure of the TRAPPIST-1 system ([Schoonenberg et al. 2019](#)). Given that these they are inferred to form at similar temperatures, one may expect that the building blocks of close-in planets have carbonaceous chondrite-like compositions.

The bulk densities of the outer four TRAPPIST-1 planets may be consistent with having formed from carbonaceous chondrite-like planetary embryos. Carbonaceous chondrites have 20-25% iron by mass (see values compiled in [Lodders & Fegley 1998](#)), primarily due to an enhance volatile inventory relative to Earth. Carbonaceous chondrites have ~ 1 -10% water by mass (and are thought to represent the source population of planetesimals that delivered water to Earth; see [Meech & Raymond 2019](#), for a review). This is similar to water contents inferred for super-Earths assuming that they grew from planetesimals just past the snow line ([Ormel et al. 2017](#); [Schoonenberg et al. 2019](#); [Bitsch et al. 2019](#); [Liu et al. 2020](#)). In contrast, Earth is only $\sim 0.1\%$ water by mass (e.g., [Hirschmann 2006](#); [Marty 2012](#), although uncertainties remain in the core's hydrogen content). The higher water content and lower iron content of carbonaceous chondrite planets relative to Earth would lower the bulk density of a carbonaceous planet, which is consistent with the measurements for the outer TRAPPIST-1 planets.

Ceres may be a more relevant analog to the outer TRAPPIST-1 planets than Earth. While it is far less massive than Earth or the TRAPPIST-1 planets ($M_{\text{Ceres}} \approx 1.5 \times 10^{-4} M_{\oplus}$), Ceres is likely carbonaceous in composition ([Bland et al. 2016](#); [McSween et al. 2018](#); [Marchi et al. 2019](#)) and is likely to have been implanted into the main belt during the giant planets' growth ([Raymond & Izidoro 2017](#)). While Ceres appears to have too much water (roughly 40% by mass) and its bulk composition would be too low-density to match the TRAPPIST-1 planets, interior models of scaled-up Ceres-like planets might provide a useful comparison for super-Earth bulk density measurements.

Can the TRAPPIST-1 planets' densities and core mass fractions be used to differentiate between formation scenarios? At present, the other viable model for super-Earth formation – sometimes called the *drift* model – invokes accretion close-in from a disk of solids that has been enriched by the inward drift of pebbles ([Chatterjee & Tan 2014, 2015](#); [Dawson et al. 2015](#)).¹⁶ After large embryos grow they are necessarily subject to migration and then follow the same general dynamical pathway as in the migration model (involving resonant capture and later breaking of resonant chains; see discussion in [Raymond et al. 2018](#)). Given that the outer disk represents the main source of drifting pebbles ([Lambrechts & Johansen 2014](#); [Ida et al. 2016](#)), one may thus expect the planets that form in the drift model could also be carbonaceous in composition. The main difference with regards to the migration model is that inward-drifting pebbles would lose their water but inward-migrating embryos would not.

Alternatively, the lower measured bulk densities of the TRAPPIST-1 planets relative to Earth-like composition might be explained by core-free interiors ([Elkins-Tanton & Seager 2008](#))

¹⁶ We note that any "in-situ" growth scenario that does not account for orbital migration is clearly ruled out using simple timescale arguments (i.e., because migration – and even aerodynamic drift – is far too fast to ignore; see [Ogihara et al. 2015](#); [Inamdar & Schlichting 2015](#); [Izidoro & Raymond 2018](#)).

in which the Oxygen content is high enough such that all iron is oxidised. If the refractory elements (Mg, Fe, Si) follow Solar abundances, a fully oxidised interior would contain about 38.2 wt% of Oxygen, which lies between the value for Earth (29.7 wt%) and CI chondrites (45.9 wt%). Such an interior scenario can easily describe the observed bulk densities (purple line in Fig. 12). And this may bolster the long-range migration scenario in which the planets formed in a highly oxidizing environment which enabled the iron to remain in the mantle even after migration.

However, the evidence for a core-free planet rests on knowing the refractory abundances of the TRAPPIST-1 host star, which have yet to be constrained. Alas, our interpretation of the planets' compositions may rest on our imprecise knowledge of the host star: its radius, its mass, its photospheric inhomogeneity, and its refractory abundances all affect our measurement and interpretation of the masses, radii, and compositions of the TRAPPIST-1 planets. In this paper our measurements of the relative planetary radii and masses have reached such a precision that the fault may now lie in the star.

11.2 Future work

We conclude by pointing out directions for building upon the work described in this paper:

- (i) We have yet to identify the origin of timing outliers which show an excess relative to a normal distribution. This may be addressed with higher precision measurements which may be able to identify a source of noise responsible for these outliers.
- (ii) Our analysis assumes a plane-parallel system with seven planets, and does not yet couple the dynamical and photometric analysis (our photodynamics held the dynamical model fixed). Future analysis with a fully-coupled photodynamical model with 3D orbits and more than seven planets may be warranted.
- (iii) We need more transits measured for planets d and h, in order to better measure the amplitude and phase on the transit-timing variation timescale, as well as to better constrain the presence of planets beyond h.
- (iv) The interpretation of the compositions of the planets is limited by the unknown composition of the host star. A measurement of the C/O ratio would validate the assumption we have made that composition is dominated by silicates rather than silicon carbide. A measurement of the Mg/Fe and Fe/Si ratios would help to interpret the core and mantle compositions. Both sets of constraints would help to limit the range and break degeneracies of possible interior compositions of the planets (Dorn et al. 2015; ?).
- (v) Without a constraint on the detailed abundance ratios of the host star, a Bayesian interpretation of the bulk densities of the planets should be warranted (Dorn et al. 2016) to better quantify the range of possible compositions. (vi) More detailed spectral analysis of the stellar photosphere to ascertain the impact of an inhomogeneous stellar atmosphere on the radius ratios would be warranted.

We anticipate that once JWST launches, we will obtain higher precision constraints upon the dynamics of the system, yielding much improved constraints upon the planets' bulk densities, which will further improve the interpretation of their interior compositions.

ACKNOWLEDGEMENTS

This work is based in part on observations made with the Spitzer Space Telescope, which is operated by the Jet Propulsion Laboratory, California Institute of Technology under a contract with NASA.

Support for this work was provided by NASA through an award issued by JPL/Caltech. EA was supported by a Guggenheim Fellowship. Additional support for this work was provided by the NASA Astrobiology Institutes Virtual Planetary Laboratory, supported by the National Aeronautics and Space Administration through the NASA Astrobiology Institute under solicitation NNA13ZDA002C and Cooperative Agreement Number NNA13AA93A. This work was facilitated through the use of the advanced computational, storage, and networking infrastructure provided by the Hyak supercomputer system at the University of Washington. Calculations were performed on UBELIX (<http://www.id.unibe.ch/hpc>), the HPC cluster at the University of Bern. This work has been carried out in the framework of the PlanetS National Centre of Competence in Research (NCCR) supported by the Swiss National Science Foundation (SNSF). This research has made use of NASA's Astrophysics Data System and of services produced by the NASA Exoplanet Science Institute at the California Institute of Technology. This project has received funding from the European Unions Horizon 2020 research and innovation program under the Marie Skłodowska-Curie Grant Agreement No. 832738/ES-CAPE and European Research Council (ERC; grants agreement n° 679030/WHIPLASH and 803193/BEBOP). M.T. thanks the Gruber Foundation for its generous support to this research. The research leading to these results has received funding from the European Research Council under the European Union's Seventh Framework Programme (FP/2007-2013) ERC Grant Agreement n° 336480, and from the ARC grant for Concerted Research Actions, financed by the Wallonia-Brussels Federation. CD acknowledges the support of the Swiss National Foundation under grant PZ00P2_174028. V.V.G. is a F.R.S.-FNRS Research Associate. M.G. and E.J. are F.R.S.-FNRS Senior Research Associates. R.M. acknowledges support for this research from NASA (grant 80NSSC18K0397). Z.L. acknowledges support from the Washington NASA Space Grant Consortium Summer Undergraduate Research Program.

We thank Trevor Branch for discussions about HMC and automatic differentiation. We thank Pramod Gupta, Diana Windemuth, and Tyler Gordon for help in using Hyak. We thank Rory Barnes, Jim Davenport and Dave Joswiak for useful discussions.

REFERENCES

- Agol E., Fabrycky D. C., 2017, in "Deeg H. J., Belmonte J. A., eds., "Handbook of Exoplanets". "Springer International Publishing", pp 1–20, doi:10.1007/978-3-319-30648-3_7-1, https://doi.org/10.1007/978-3-319-30648-3_7-1
- Agol E., Hernandez D. M., 2020, in preparation
- Agol E., Steffen J., Sari R., Clarkson W., 2005, *Monthly Notices of the Royal Astronomical Society*, 359, 567
- Agol E., Luger R., Foreman-Mackey D., 2019, arXiv e-prints, p. arXiv:1908.03222
- Akeson R. L., et al., 2013, *Publications of the Astronomical Society of the Pacific*, 125, 989
- Allard F., Homeier D., Freytag B., 2011, *Proceedings of the International Astronomical Union*, 7, 235
- Allard F., Homeier D., Freytag B., 2012, *Philosophical Transactions of the Royal Society A: Mathematical, Physical and Engineering Sciences*, 370, 2765
- Armitage P. J., Eisner J. A., Simon J. B., 2016, *ApJ*, 828, L2
- Asphaug E., Reufer A., 2014, *Nature Geoscience*, 7, 564
- Barr A. C., 2016, *Journal of Geophysical Research: Planets*, 121, 1573
- Barstow J. K., Irwin P. G. J., 2016, *MNRAS*, 461, L92
- Batalha N. E., Lewis N. K., Line M. R., Valenti J., Stevenson K., 2018, *The Astrophysical Journal*, 856, L34

- Benz W., Slattery W. L., Cameron A. G. W., 1988, *Icarus*, **74**, 516
- Betancourt M., 2017, arXiv preprint arXiv:1701.02434
- Bitsch B., Raymond S. N., Izidoro A., 2019, *A&A*, **624**, A109
- Bland M. T., et al., 2016, *Nature Geoscience*, **9**, 538
- Bolmont E., Selsis F., Owen J. E., Ribas I., Raymond S. N., Leconte J., Gillon M., 2017, *MNRAS*, **464**, 3728
- Bond J. C., Lauretta D. S., OBrien D. P., 2010, *Icarus*, **205**, 321
- Bourrier V., et al., 2017, *AJ*, **154**, 121
- Brasser R., Barr A. C., Dobos V., 2019, *Monthly Notices of the Royal Astronomical Society*, 487, 34
- Burbine T. H., McCoy T. J., Meibom A., Gladman B., Keil K., 2002, *Meteoritic Parent Bodies: Their Number and Identification*. University of Arizona Press, Tucson, Arizona, USA, pp 653–667
- Burdanov A., Delrez L., Gillon M., Jehin E., 2018, in , *Handbook of Exoplanets*. Springer International Publishing, pp 1007–1023, doi:10.1007/978-3-319-55333-7_130, https://doi.org/10.1007/978-3-319-55333-7_130
- Burdanov A. Y., et al., 2019, *Monthly Notices of the Royal Astronomical Society*
- Burgasser A. J., Mamajek E. E., 2017, *The Astrophysical Journal*, **845**, 110
- Bus S. J., Binzel R. P., 2002, *Icarus*, **158**, 146
- Carey S. J., et al., 2004, in Mather J. C., ed., *Optical, Infrared, and Millimeter Space Telescopes*. SPIE, doi:10.1117/12.550968, https://doi.org/10.1117/12.550968
- Carter J. A., et al., 2012, *Science*, **337**, 556
- Casali M., et al., 2007, *Astronomy & Astrophysics*, **467**, 777
- Chatterjee S., Tan J. C., 2014, *ApJ*, **780**, 53
- Chatterjee S., Tan J. C., 2015, *ApJ*, **798**, L32
- Chiang E. I., Murray N., 2002, *ApJ*, **576**, 473
- Christiansen J., 2018, in , *Handbook of Exoplanets*. Springer International Publishing, pp 1933–1947, doi:10.1007/978-3-319-55333-7_150, https://doi.org/10.1007/978-3-319-55333-7_150
- Coleman G. A. L., Leleu A., Alibert Y., Benz W., 2019, *A&A*, **631**, A7
- Cossou C., Raymond S. N., Hersant F., Pierens A., 2014, *A&A*, **569**, A56
- Cresswell P., Nelson R. P., 2008, *Astronomy & Astrophysics*, **482**, 677
- Dai F., Masuda K., Winn J. N., Zeng L., 2019, *The Astrophysical Journal*, **883**, 79
- Dawson R. I., Chiang E., Lee E. J., 2015, *MNRAS*, **453**, 1471
- DeMeo F. E., Carry B., 2013, *Icarus*, **226**, 723
- Deck K. M., Agol E., 2015, *The Astrophysical Journal*, **802**, 116
- Deck K. M., Agol E., 2016, *The Astrophysical Journal*, **821**, 96
- Dehnen W., Hernandez D. M., 2017, *MNRAS*, **465**, 1201
- Delrez L., et al., 2018a, SPECULOOS: a network of robotic telescopes to hunt for terrestrial planets around the nearest ultracool dwarfs (arXiv:1806.11205)
- Delrez L., et al., 2018b, *Monthly Notices of the Royal Astronomical Society*, **475**, 3577
- Dorn C., Khan A., Heng K., Connolly J. A. D., Alibert Y., Benz W., Tackley P., 2015, *Astronomy & Astrophysics*, **577**, A83
- Dorn C., Venturini J., Khan A., Heng K., Alibert Y., Helled R., Rivoldini A., Benz W., 2016, *Astronomy & Astrophysics*, **597**, A37
- Dorn C., Mosegaard K., Grimm S. L., Alibert Y., 2018, *The Astrophysical Journal*, **865**, 20
- Dressing C. D., et al., 2015, *The Astrophysical Journal*, **800**, 135
- Drążkowska J., Alibert Y., 2017, *A&A*, **608**, A92
- Duane S., Kennedy A., Pendleton B. J., Roweth D., 1987, *Physics Letters B*, **195**, 216
- Ducrot E., et al., 2018, *The Astronomical Journal*, **156**, 218
- Ducrot E., et al., 2020, *Astronomy & Astrophysics*
- Eastman J., Siverd R., Gaudi B. S., 2010, *Publications of the Astronomical Society of the Pacific*, **122**, 935
- Eastman J., Gaudi B. S., Agol E., 2013, *Publications of the Astronomical Society of the Pacific*, **125**, 83
- Elkins-Tanton L. T., Seager S., 2008, *The Astrophysical Journal*, **688**, 628
- Elser S., Meyer M. R., Moore B., 2012, *Icarus*, **221**, 859
- Fabrycky D. C., 2010, in Seager S., ed., *Exoplanets*. pp 217–238
- Faucher T. J., et al., 2019, *The Astrophysical Journal*, **887**, 194
- Faucher T. J., et al., 2020, *Geoscientific Model Development*, **13**, 707
- Feng F., Tuomi M., Jones H. R. A., Barnes J., Anglada-Escudé G., Vogt S. S., Butler R. P., 2017, *The Astronomical Journal*, **154**, 135
- Fisher R. A., 1925, *Metron*, **5**, 90
- Foreman-Mackey D., 2014, Blog Post: Mixture Models, doi:10.5281/zenodo.15856, https://zenodo.org/record/15856
- Foreman-Mackey D., Agol E., Ambikasaran S., Angus R., 2017, *The Astronomical Journal*, **154**, 220
- Gillon M., 2018, *Nature Astronomy*, **2**, 344
- Gillon M., Jehin E., Fumel A., Magain P., Queloz D., 2013, in *European Physical Journal Web of Conferences*. p. 03001, doi:10.1051/epjconf/20134703001
- Gillon M., et al., 2016, *Nature*, **533**, 221
- Gillon M., et al., 2017, *Nature*, **542**, 456
- Gillon M., et al., 2020, arXiv e-prints, p. arXiv:2002.04798
- Gonçalves Ferrari G., Boekholt T., Portegies Zwart S. F., 2014, *MNRAS*, **440**, 719
- Gonzales E. C., Faherty J. K., Gagné J., Teske J., McWilliam A., Cruz K., 2019, *The Astrophysical Journal*, **886**, 131
- Goodman J., Weare J., 2010, *Communications in Applied Mathematics and Computational Science*, **5**, 65
- Grady J., Tedesco E., 1982, *Science*, **216**, 1405
- Grimm S. L., Stadel J. G., 2014, *ApJ*, **796**, 23
- Grimm S. L., et al., 2018, *Astronomy & Astrophysics*, **613**, A68
- He M. Y., Triana A. H. M. J., Gillon M., 2016, *Monthly Notices of the Royal Astronomical Society*, **464**, 2687
- Hernandez D. M., Bertschinger E., 2015, *Monthly Notices of the Royal Astronomical Society*, **452**, 1934
- Hernandez D. M., Dehnen W., 2017, *Monthly Notices of the Royal Astronomical Society*, **468**, 2614
- Hirano T., et al., 2020, arXiv e-prints, p. arXiv:2002.05892
- Hirschmann M. M., 2006, *Annual Review of Earth and Planetary Sciences*, **34**, 629
- Hogg D. W., Bovy J., Lang D., 2010, arXiv e-prints, p. arXiv:1008.4686
- Howell S. B., et al., 2014, *Publications of the Astronomical Society of the Pacific*, **126**, 398
- Ida S., Guillot T., Morbidelli A., 2016, *A&A*, **591**, A72
- Inamdar N. K., Schlichting H. E., 2015, *MNRAS*, **448**, 1751
- Ingalls J. G., et al., 2016, *The Astronomical Journal*, **152**, 44
- Izidoro A., Raymond S. N., 2018, in , *Handbook of Exoplanets*. Springer International Publishing, p. 142, doi:10.1007/978-3-319-55333-7_142
- Izidoro A., Ogihara M., Raymond S. N., Morbidelli A., Pierens A., Bitsch B., Cossou C., Hersant F., 2017, *MNRAS*, **470**, 1750
- Izidoro A., Bitsch B., Raymond S. N., Johansen A., Morbidelli A., Lambrechts M., Jacobson S. A., 2019, arXiv e-prints, p. arXiv:1902.08772
- Jehin E., et al., 2011, *The Messenger*, **145**, 2
- Jehin E., et al., 2018, *Published in The Messenger vol. 174*, pp. 2-7, December 2018.
- Jontof-Hutter D., et al., 2016, *The Astrophysical Journal*, **820**, 39
- Jontof-Hutter D., Truong V. H., Ford E. B., Robertson P., Terrien R. C., 2018, *The Astronomical Journal*, **155**, 239
- Juncher D., Jørgensen U. G., Helling C., 2017, *Astronomy & Astrophysics*, **608**, A70
- Khan A., Liebske C., Rozel A., Rivoldini A., Nimmo F., Connolly J. A. D., Plesa A.-C., Giardini D., 2018, *Journal of Geophysical Research: Planets*, **123**, 575
- Kipping D. M., 2012, *Monthly Notices of the Royal Astronomical Society*, **427**, 2487
- Kipping D. M., 2013, *Monthly Notices of the Royal Astronomical Society*, **435**, 2152
- Kipping D., 2018, *Research Notes of the AAS*, **2**, 136
- Kipping D. M., Dunn W. R., Jasinski J. M., Manthri V. P., 2012, *Monthly Notices of the Royal Astronomical Society*, **421**, 1166
- Klein B., Donati J.-F., 2019, *Monthly Notices of the Royal Astronomical Society*, **488**, 5114
- Knutson H. A., Charbonneau D., Allen L. E., Burrows A., Megeath S. T., 2008, *The Astrophysical Journal*, **673**, 526
- Kopparapu R. K., et al., 2013, *ApJ*, **765**, 131

- Krissansen-Totton J., Garland R., Irwin P., Catling D. C., 2018, *The Astrophysical Journal*, 156, 114
- Lambrechts M., Johansen A., 2014, *A&A*, 572, A107
- Lissauer J. J., 2007, *The Astrophysical Journal*, 660, L149
- Lithwick Y., Xie J., Wu Y., 2012, *The Astrophysical Journal*, 761, 122
- Liu B., Lambrechts M., Johansen A., Pascucci I., Henning T., 2020, arXiv e-prints, p. [arXiv:2004.07239](https://arxiv.org/abs/2004.07239)
- Lodders K., Fegley B., 1998, *The planetary scientist's companion* / Katharina Lodders, Bruce Fegley. New York : Oxford University Press
- Lodders K., Palme H., Gail H., 2009, *JE Trümper*, 4, 44
- Luger R., et al., 2017a, *Nature Astronomy*, 1, 0129
- Luger R., Lustig-Yaeger J., Agol E., 2017b, *The Astrophysical Journal*, 851, 94
- Lustig-Yaeger J., Meadows V. S., Lincowski A. P., 2019, *The Astronomical Journal*, 158, 27
- MacDonald M. G., Dawson R. I., 2018, *The Astronomical Journal*, 156, 228
- Mah J., 2018, HKU Theses Online (HKUTO)
- Malhotra R., 2002, *ApJ*, 575, L33
- Mann A. W., et al., 2019, *The Astrophysical Journal*, 871, 63
- Marchi S., et al., 2019, *Nature Astronomy*, 3, 140
- Marcus R. A., Sasselov D., Hernquist L., Stewart S. T., 2010, *ApJ*, 712, L73
- Marty B., 2012, *Earth and Planetary Science Letters*, 313, 56
- McDonough W., 2014, in , *Treatise on Geochemistry*. Elsevier, pp 559–577, doi:10.1016/b978-0-08-095975-7.00215-1, <https://doi.org/10.1016/b978-0-08-095975-7.00215-1>
- McNeil D. S., Nelson R. P., 2010, *MNRAS*, 401, 1691
- McSween H. Y., et al., 2018, *Meteoritics and Planetary Science*, 53, 1793
- Meech K., Raymond S. N., 2019, arXiv e-prints, p. [arXiv:1912.04361](https://arxiv.org/abs/1912.04361)
- Monnahan C. C., Thorson J. T., Branch T. A., 2016, *Methods in Ecology and Evolution*, 8, 339
- Morley C. V., Kreidberg L., Rustamkulov Z., Robinson T., Fortney J. J., 2017, *The Astrophysical Journal*, 850, 121
- Morris B. M., Agol E., Hebb L., Hawley S. L., 2018a, *The Astronomical Journal*, 156, 91
- Morris B. M., Agol E., Davenport J. R. A., Hawley S. L., 2018b, *ApJ*, 857, 39
- Morris B. M., et al., 2018c, *The Astrophysical Journal*, 863, L32
- Murray C. D., Dermott S. F., 1999, *Solar system dynamics*, 1 edn. Cambridge University Press, New York, New York
- Murray C. A., et al., 2020, *Monthly Notices of the Royal Astronomical Society*
- Namouni F., 2005, *AJ*, 130, 280
- Neal R. M., 2011, *Handbook of markov chain monte carlo*, 2, 2
- Öberg K. I., Bergin E. A., 2016, *The Astrophysical Journal Letters*, 831, L19
- Ogihara M., Ida S., 2009, *ApJ*, 699, 824
- Ogihara M., Morbidelli A., Guillot T., 2015, *A&A*, 578, A36
- Ormel C. W., Liu B., Schoonenberg D., 2017, *Astronomy & Astrophysics*, 604, A1
- Owen J. E., Wu Y., 2017, *The Astrophysical Journal*, 847, 29
- Palme H., Lodders K., Jones A., 2014, in , *Treatise on Geochemistry*. Elsevier, pp 15–36, doi:10.1016/b978-0-08-095975-7.00118-2, <https://doi.org/10.1016/b978-0-08-095975-7.00118-2>
- Papaloizou J. C. B., 2014, *International Journal of Astrobiology*, 14, 291
- Papaloizou J. C. B., Szuszkiewicz E., Terquem C., 2017, *Monthly Notices of the Royal Astronomical Society*, 476, 5032
- Pletzer V., Basano L., 2017, *Exponential Distance Relation and Near Resonances in the Trappist-1 Planetary System* ([arXiv:1703.04545](https://arxiv.org/abs/1703.04545))
- Quares B., Quintana E. V., Lopez E., Schlieder J. E., Barclay T., 2017, *The Astrophysical Journal*, 842, L5
- Rackham B. V., Apai D., Giampapa M. S., 2018, *The Astrophysical Journal*, 853, 122
- Raymond S. N., Izidoro A., 2017, *Icarus*, 297, 134
- Raymond S., Nesvorný D., 2020, Submitted
- Raymond S. N., Izidoro A., Morbidelli A., 2018, arXiv e-prints, p. [arXiv:1812.01033](https://arxiv.org/abs/1812.01033)
- Revels J., Lubin M., Papamarkou T., 2016, arXiv:1607.07892 [cs.MS]
- Ronnet T., Mousis O., Vernazza P., Lunine J. I., Crida A., 2018, *AJ*, 155, 224
- Sagear S. A., Skinner J. N., Muirhead P. S., 2019, Upper Limits on Planet Occurrence around Ultracool Dwarfs with K2 ([arXiv:1912.04286](https://arxiv.org/abs/1912.04286))
- Schoonenberg D., Ormel C. W., 2017, *A&A*, 602, A21
- Schoonenberg D., Liu B., Ormel C. W., Dorn C., 2019, *Astronomy & Astrophysics*, 627, A149
- Scora J., Valencia D., Morbidelli A., Jacobson S., 2020, *Monthly Notices of the Royal Astronomical Society*
- Seager S., Mallen-Ornelas G., 2003, *The Astrophysical Journal*, 585, 1038
- Sestovic M., Demory B.-O., 2020, arXiv e-prints, p. [arXiv:2005.01440](https://arxiv.org/abs/2005.01440)
- Siebenmorgen R., Carraro G., Valenti E., Petr-Gotzens M., Brammer G., Garcia E., Casali M., 2011, *The Messenger*, 144, 9
- Spalding C., Adams F. C., 2020, *The Planetary Science Journal*, 1, 7
- Steele I. A., et al., 2004, in Jacobus M. Oschmann J., ed., *Ground-based Telescopes*. SPIE, doi:10.1117/12.551456, <https://doi.org/10.1117/12.551456>
- Stetson P. B., 1987, *Publications of the Astronomical Society of the Pacific*, 99, 191
- Tamayo D., Rein H., Petrovich C., Murray N., 2017, *The Astrophysical Journal*, 840, L19
- Terquem C., Papaloizou J. C. B., 2007, *ApJ*, 654, 1110
- Tinney C. G., et al., 2004, in *Ground-based Instrumentation for Astronomy*. SPIE, doi:10.1117/12.550980, <https://doi.org/10.1117/12.550980>
- Turbet M., et al., 2018, *Astronomy & Astrophysics*, 612, A86
- Turbet M., Ehrenreich D., Lovis C., Bolmont E., Fauchez T., 2019, *A&A*, 628, A12
- Turbet M., Bolmont E., Ehrenreich D., Gratier P., Leconte J., Selsis F., Hara N., Lovis C., 2020, arXiv e-prints, p. [arXiv:1911.08878](https://arxiv.org/abs/1911.08878)
- Unterborn C. T., Desch S. J., Hinkel N. R., Lorenzo A., 2018, *Nature Astronomy*, 2, 297
- Valencia D., Sasselov D. D., O'Connell R. J., 2007, *The Astrophysical Journal*, 665, 1413
- Van Grootel V., et al., 2018, *The Astrophysical Journal*, 853, 30
- Vida K., Kővári Z., Pál A., Oláh K., Kriskovics L., 2017, *The Astrophysical Journal*, 841, 124
- Wakeford H. R., et al., 2018, *The Astronomical Journal*, 157, 11
- Wakeford H. R., et al., 2019, *AJ*, 157, 11
- Walsh K. J., Morbidelli A., Raymond S. N., O'Brien D. P., Mandell A. M., 2011, *Nature*, 475, 206
- Weidenschilling S. J., 1977, *MNRAS*, 180, 57
- Wisdom J., Hernandez D. M., 2015, *Monthly Notices of the Royal Astronomical Society*, 453, 3015
- Wisdom J., Holman M., 1991, *The Astronomical Journal*, 102, 1528
- Wolf E. T., 2017, *ApJ*, 839, L1
- Wunderlich F., et al., 2019, *Astronomy and Astrophysics*, 624, A49
- Zeng L., Sasselov D. D., Jacobsen S. B., 2016, *The Astrophysical Journal*, 819, 127
- de Wit J., et al., 2016, *Nature*, 537, 69
- de Wit J., et al., 2018, *Nature Astronomy*, 2, 214
- ter Braak C., 2006, *Statistics and Computing*, 16, 239

APPENDIX A: APPROXIMATE HESSIAN MATRIX

Here we approximate the posterior probability distribution as a multi-dimensional Gaussian, assuming a uniform prior. The maximum posterior probability also corresponds to the maximum likelihood in this limit, in which case we expand the log likelihood for the i th planet and j th transit as a Taylor series:

$$\log \mathcal{L}_{ij}(\mathbf{x}) \approx \log \mathcal{L}_{ij}(\mathbf{x}_0) + \frac{1}{2} \sum_{k,l} \left. \frac{\partial^2 \log \mathcal{L}_{ij}(\mathbf{x})}{\partial x_k \partial x_l} \right|_{\mathbf{x}_0} (x_k - x_{0,k})(x_l - x_{0,l}), \quad (\text{A1})$$

where we have used the fact that the gradient of the log likelihood vanishes at the maximum likelihood value of the model parameters, \mathbf{x}_0 , and the indices $k, l = 1, \dots, 5N_p + 2$ for x_k and x_l , where the first $5N_p$ parameters are the dynamical parameters, \mathbf{x}_{dyn} , and the last two parameters are the Student's t-distribution likelihood parameters, $\log \nu$ and $V_1 e^{1/2\nu}$. Now, the width of the Gaussian distribution at the maximum likelihood is governed by the Hessian matrix, with elements given by

$$\mathcal{H}_{kl}(\mathbf{x}_0) = - \sum_{i,j} \left. \frac{\partial^2 \log \mathcal{L}_{ij}(\mathbf{x})}{\partial x_k \partial x_l} \right|_{\mathbf{x}_0}, \quad (\text{A2})$$

which involves second derivatives of the log likelihood with respect to the model parameters. The log likelihood for each data point with indices i and j may be written as a function of the observed transit times and uncertainties, the modeled transit times, and the Student's t-distribution model parameters, such that

$$\mathcal{L}_{ij}(\mathbf{x}) = \mathcal{L}_{ij}(t_{ij}(\mathbf{x}_{dyn}); \log \nu, V_1 e^{1/2\nu}; t_{ij,obs}, \sigma_{ij}), \quad (\text{A3})$$

where all of the dependence on the dynamical model parameters enters through $t_{ij}(\mathbf{x}_{dyn})$. The derivatives of t_{ij} with respect to \mathbf{x}_{dyn} we compute with the NbodyGradient code; however, the second derivatives of the transit times with respect to the dynamical model parameters are not computed with our N-body code. We drop these transit time second derivative terms, which we justify as follows.

For the Hessian matrix elements which involve second derivatives with respect to both dynamical model parameters, $1 \leq k, l \leq 5N_p$, we can write:

$$\frac{\partial^2 \log \mathcal{L}_{ij}(\mathbf{x})}{\partial x_k \partial x_l} = \frac{\partial^2 \log \mathcal{L}_{ij}(\mathbf{x})}{\partial^2 t_{ij}} \frac{\partial t_{ij}}{\partial x_k} \frac{\partial t_{ij}}{\partial x_l} + \frac{\partial \log \mathcal{L}_{ij}(\mathbf{x})}{\partial t_{ij}} \frac{\partial^2 t_{ij}}{\partial x_k \partial x_l}, \quad (\text{A4})$$

where $t_{ij} = t_{ij}(\mathbf{x}_{dyn})$ is implied in this and subsequent equations.

Now, at the maximum likelihood there is a balance of residuals which are both positive and negative, such that the second component of this equation has terms with positive and negative signs for different values of i and j . This causes the second term in this equation to average to a small value compared with the first term when the sum is carried out over i and j (the planet and transit indices). So, we drop the second term in this equation.

Adding in the cases of the Hessian matrix elements which involve the likelihood parameters, $(x_{5N_p+1}, x_{5N_p+2}) = (\log \nu, V_1 e^{1/2\nu})$, we compute the Hessian as

$$\mathcal{H}_{k,l}(\mathbf{x}) = - \sum_{i,j} \begin{cases} \frac{\partial^2 \log \mathcal{L}_{ij}(\mathbf{x})}{\partial^2 t_{ij}} \frac{\partial t_{ij}}{\partial x_k} \frac{\partial t_{ij}}{\partial x_l} & 1 \leq k, l \leq 5N_p \\ \frac{\partial^2 \log \mathcal{L}_{ij}(\mathbf{x})}{\partial t_{ij} \partial x_l} \frac{\partial t_{ij}}{\partial x_k} & 1 \leq k \leq 5N_p; l > 5N_p \\ \frac{\partial^2 \log \mathcal{L}_{ij}(\mathbf{x})}{\partial t_{ij} \partial x_k} \frac{\partial t_{ij}}{\partial x_l} & l > 5N_p; 1 \leq k \leq 5N_p \\ \frac{\partial^2 \log \mathcal{L}_{ij}(\mathbf{x})}{\partial x_k \partial x_k} & k, l > 5N_p \end{cases}, \quad (\text{A5})$$

where the partial derivatives with respect to $t_{ij}(\mathbf{x}_{dyn})$, $x_{5N_p+1} = \log \nu$, and $x_{5N_p+2} = V_1 e^{1/2\nu}$ are computed with automatic differentiation.

The inverse of the Hessian matrix is used in the Levenburg-Marquardt optimization, and when evaluated at the maximum likelihood, is used to estimate the covariance matrix, from which the square root of the diagonal components are used to estimate the widths of the posterior distribution for each model parameter, $\mathbf{x} = (\mathbf{x}_{dyn}, \log \nu, V_1 e^{1/2\nu})$, which are plotted in Figures 4, 5, and 6. This approximated Hessian is also used to define the mass matrix for the HMC simulations.

APPENDIX B: TABLES

Tables of the HMC prior (Table B1), the best-fit transit times (Table B2), and the forecast times (Table B3) are given in this appendix.

Parameter	Variable	Lower bound	Lower transition	Upper transition	Upper bound
Mass-ratio	$\log_{10} \mu$	ξ_1	ξ_2	ξ_3	ξ_4
Eccentricity	e	-8	-7	-3	-2
Period of b	P_b [d]	-	-	0.2	0.3
Period of c	P_c [d]	1.49	1.50	1.52	1.53
Period of d	P_d [d]	2.40	2.41	2.43	2.44
Period of e	P_e [d]	4.03	4.04	4.06	4.07
Period of f	P_f [d]	6.08	6.09	6.11	6.12
Period of g	P_g [d]	9.18	9.19	9.22	9.23
Period of h	P_h [d]	12.33	12.34	12.36	12.37
Initial transit time of b	$t_{0,b} - 2, 457, 257$ [d]	18.75	18.76	18.78	18.79
Initial transit time c	$t_{0,c} - 2, 457, 257$ [d]	0.53	0.54	0.56	0.57
Initial transit time d	$t_{0,d} - 2, 457, 257$ [d]	0.57	0.58	0.60	0.61
Initial transit time e	$t_{0,e} - 2, 457, 257$ [d]	0.05	0.06	0.08	0.09
Initial transit time f	$t_{0,f} - 2, 457, 257$ [d]	0.81	0.82	0.84	0.85
Initial transit time g	$t_{0,g} - 2, 457, 257$ [d]	0.05	0.06	0.08	0.09
Initial transit time h	$t_{0,h} - 2, 457, 249$ [d]	0.70	0.71	0.73	0.74
Degrees of freedom	ν	0.58	0.59	0.61	0.62
Log variance factor	$\log V_1$	0.5	1.0	50	100
		-2	-1	5	10

Table B1. Prior probability boundary limits for the TRAPPIST-1 planet parameters. The bounds are chosen so as to not affect the parameters as much as possible.

Planet	Epoch	t_{obs}	σ_{obs}	t_{post}	σ_{post}	Source
b	0	7322.515310	0.000710	7322.517902	0.000127	TS
b	2	7325.539100	0.001000	7325.539172	0.000113	TS
b	4	7328.558600	0.001300	7328.561188	0.000124	TS
b	6	7331.581600	0.001000	7331.582576	0.000113	TS
b	8	7334.604800	0.000170	7334.604787	0.000121	LT + VLT
b	10	7337.626440	0.000920	7337.626038	0.000107	TS
b	12	7340.648200	0.001400	7340.648105	0.000119	TS
b	15	7345.180280	0.000800	7345.180808	0.000116	HCT
b	26	7361.799450	0.000280	7361.799794	0.000095	UK
b	28	7364.821730	0.000770	7364.821958	0.000108	UK
b	78	7440.365180	0.000380	7440.365030	0.000080	Spitzer
b	86	7452.452250	0.000180	7452.451982	0.000077	Spitzer
b	93	7463.028400	0.000240	7463.028310	0.000079	Spitzer
b	124	7509.864600	0.002100	7509.865252	0.000068	TS
b	126	7512.887310	0.000290	7512.886769	0.000061	TS + HST
b	163	7568.788800	0.001000	7568.788974	0.000053	TS
b	175	7586.918240	0.000640	7586.919266	0.000039	TS
b	177	7589.939220	0.000920	7589.941544	0.000047	TS
b	183	7599.006400	0.000210	7599.006277	0.000038	UK
b	185	7602.028130	0.000360	7602.028554	0.000045	UK
b	192	7612.605950	0.000850	7612.604095	0.000036	TN
b	194	7615.627100	0.001600	7615.626397	0.000044	TS
b	200	7624.690940	0.000660	7624.691115	0.000035	TS
b	214	7645.844000	0.001100	7645.843734	0.000036	WHT
b	218	7651.887310	0.000200	7651.887442	0.000038	Spitzer
b	219	7653.398010	0.000330	7653.398070	0.000038	Spitzer
b	220	7654.909080	0.000840	7654.908746	0.000037	TS
b	221	7656.419000	0.000290	7656.419631	0.000036	TS + LT
b	222	7657.931340	0.000240	7657.930773	0.000035	Spitzer
b	223	7659.441440	0.000170	7659.441463	0.000033	TN + Spitzer
b	224	7660.952170	0.000210	7660.952221	0.000033	Spitzer
b	225	7662.463670	0.000400	7662.463586	0.000035	Spitzer
b	226	7663.975297	0.000950	7663.974451	0.000036	Spitzer
b	227	7665.485460	0.000290	7665.485083	0.000037	Spitzer
b	228	7666.995610	0.000130	7666.995739	0.000036	Spitzer
b	229	7668.506660	0.000170	7668.506618	0.000037	Spitzer
b	230	7670.017750	0.000190	7670.017815	0.000035	Spitzer
b	231	7671.527910	0.000680	7671.528519	0.000033	Spitzer

Planet	Epoch	t_{obs}	σ_{obs}	t_{post}	σ_{post}	Source
b	236	7679.082639	0.000190	7679.082739	0.000037	AAT
b	238	7682.104510	0.000220	7682.104861	0.000034	AAT
b	264	7721.387470	0.000350	7721.387492	0.000030	TN
b	276	7739.517699	0.000585	7739.517867	0.000040	K2
b	277	7741.027871	0.000545	7741.028689	0.000041	K2
b	278	7742.539178	0.000580	7742.540140	0.000029	K2
b	279	7744.050894	0.000615	7744.050936	0.000028	K2
b	280	7745.561639	0.000720	7745.561618	0.000029	K2
b	281	7747.072080	0.000845	7747.072579	0.000029	K2
b	282	7748.584465	0.000870	7748.583471	0.000032	K2
b	283	7750.093872	0.000885	7750.094290	0.000038	K2
b	284	7751.605350	0.000825	7751.604921	0.000040	K2
b	285	7753.116227	0.000750	7753.115730	0.000041	K2
b	286	7754.628042	0.000770	7754.627198	0.000029	K2
b	287	7756.138560	0.000605	7756.138009	0.000027	K2
b	288	7757.648398	0.000890	7757.648679	0.000028	K2
b	289	7759.159533	0.000730	7759.159583	0.000029	K2
b	290	7760.671124	0.000820	7760.670477	0.000032	K2
b	291	7762.181196	0.000735	7762.181343	0.000038	K2
b	292	7763.692207	0.000710	7763.691980	0.000040	K2
b	293	7765.202976	0.000770	7765.202779	0.000040	K2
b	294	7766.714792	0.000550	7766.714255	0.000028	K2
b	295	7768.225136	0.001025	7768.225082	0.000026	K2
b	296	7769.737043	0.000635	7769.735744	0.000028	K2
b	297	7771.247782	0.000910	7771.246589	0.000029	K2
b	298	7772.757384	0.000750	7772.757481	0.000032	K2
b	299	7774.268414	0.000800	7774.268402	0.000038	K2
b	300	7775.779949	0.000580	7775.779047	0.000040	K2
b	301	7777.288995	0.000990	7777.289837	0.000040	K2
b	302	7778.801182	0.000620	7778.801315	0.000027	K2
b	303	7780.312968	0.000680	7780.312152	0.000026	K2
b	304	7781.822306	0.001450	7781.822804	0.000027	K2
b	305	7783.334098	0.000710	7783.333598	0.000030	K2
b	306	7784.843722	0.000680	7784.844488	0.000032	K2
b	311	7792.399786	0.001100	7792.399219	0.000025	K2
b	312	7793.909550	0.000635	7793.909863	0.000027	K2
b	313	7795.419875	0.000580	7795.420614	0.000030	K2
b	314	7796.931341	0.000650	7796.931505	0.000032	K2
b	315	7798.442107	0.000615	7798.442543	0.000037	K2
b	316	7799.953195	0.000830	7799.953209	0.000037	K2
b	317	7801.463137	0.001265	7801.463974	0.000037	K2
b	318	7802.975590	0.000180	7802.975423	0.000026	Spitzer + K2
b	319	7804.486376	0.000535	7804.486284	0.000025	K2
b	320	7805.996980	0.000160	7805.996925	0.000027	Spitzer + K2
b	321	7807.507270	0.000170	7807.507636	0.000030	Spitzer + K2
b	322	7809.018340	0.000200	7809.018522	0.000032	Spitzer + K2
b	323	7810.527807	0.001095	7810.529621	0.000035	K2
b	324	7812.040330	0.000160	7812.040298	0.000035	Spitzer + K2
b	325	7813.551230	0.000140	7813.551052	0.000036	Spitzer + K2
b	326	7815.062750	0.000180	7815.062479	0.000026	Spitzer + K2
b	327	7816.573350	0.000180	7816.573348	0.000025	Spitzer + K2
b	328	7818.083830	0.000150	7818.083982	0.000026	Spitzer
b	329	7819.594780	0.000180	7819.594663	0.000030	Spitzer
b	330	7821.105500	0.000160	7821.105545	0.000033	Spitzer
b	332	7824.127300	0.000180	7824.127396	0.000033	Spitzer
b	333	7825.638130	0.000140	7825.638140	0.000035	Spitzer
b	334	7827.149950	0.000130	7827.149528	0.000026	Spitzer
b	335	7828.660330	0.000220	7828.660405	0.000024	Spitzer
b	336	7830.170830	0.000200	7830.171040	0.000026	Spitzer
b	338	7833.192910	0.000210	7833.192577	0.000033	Spitzer
b	339	7834.703980	0.000160	7834.703794	0.000032	Spitzer

Planet	Epoch	t_{obs}	σ_{obs}	t_{post}	σ_{post}	Source
b	340	7836.214390	0.000180	7836.214496	0.000032	Spitzer
b	341	7837.725260	0.000170	7837.725229	0.000034	Spitzer
b	342	7839.236870	0.000280	7839.236575	0.000026	Spitzer
b	386	7905.715190	0.000880	7905.714915	0.000032	LT
b	394	7917.800600	0.001100	7917.802000	0.000032	TS
b	398	7923.845880	0.000430	7923.845887	0.000031	SSO
b	406	7935.932860	0.000230	7935.932936	0.000032	SSO
b	410	7941.976210	0.000380	7941.976186	0.000032	UK
b	417	7952.554500	0.001100	7952.552500	0.000028	TN
b	419	7955.575540	0.000690	7955.574761	0.000036	TN
b	421	7958.596050	0.000360	7958.596257	0.000039	LT
b	425	7964.638850	0.000440	7964.639621	0.000028	LT
b	427	7967.662460	0.000540	7967.661850	0.000036	SSO
b	429	7970.685410	0.000410	7970.683357	0.000038	LT
b	431	7973.705780	0.000530	7973.704979	0.000028	SSO
b	435	7979.748870	0.000220	7979.748938	0.000037	SSO
b	439	7985.792100	0.000310	7985.792035	0.000028	SSO
b	443	7991.835810	0.000420	7991.836022	0.000037	SSO
b	445	7994.857990	0.000550	7994.857550	0.000035	SSO
b	455	8009.966300	0.000220	8009.966166	0.000028	Spitzer
b	456	8011.477390	0.000230	8011.477412	0.000025	Spitzer
b	457	8012.988050	0.000120	8012.988154	0.000028	Spitzer
b	458	8014.498830	0.000170	8014.498884	0.000033	Spitzer
b	459	8016.010300	0.000170	8016.010178	0.000036	Spitzer
b	460	8017.521270	0.000220	8017.521082	0.000034	SSO + Spitzer
b	461	8019.031673	0.000270	8019.031738	0.000032	Spitzer
b	462	8020.542370	0.000150	8020.542375	0.000030	SSO + Spitzer
b	464	8023.564580	0.000150	8023.564537	0.000025	Spitzer
b	465	8025.075390	0.000190	8025.075294	0.000028	Spitzer
b	467	8028.097400	0.000290	8028.097254	0.000035	Spitzer
b	468	8029.608180	0.000160	8029.608161	0.000033	Spitzer
b	469	8031.118920	0.000120	8031.118831	0.000031	Spitzer
b	472	8035.651560	0.000260	8035.651667	0.000026	SSO + Spitzer
b	473	8037.162500	0.000220	8037.162437	0.000029	Spitzer
b	474	8038.672920	0.000160	8038.673143	0.000034	Spitzer
b	475	8040.184110	0.000250	8040.184324	0.000034	Spitzer
b	476	8041.695100	0.000140	8041.695236	0.000032	Spitzer
b	477	8043.205900	0.000190	8043.205925	0.000030	Spitzer
b	478	8044.716480	0.000150	8044.716551	0.000029	Spitzer
b	479	8046.227480	0.000140	8046.227403	0.000028	Spitzer
b	480	8047.737850	0.000610	8047.738794	0.000027	SSO
b	507	8088.532140	0.000220	8088.532589	0.000031	LT + SSO + VLT
b	509	8091.553870	0.000260	8091.554342	0.000034	SSO
b	511	8094.575990	0.000590	8094.575800	0.000030	SSO
b	566	8177.674960	0.000270	8177.674911	0.000043	Spitzer
b	572	8186.740050	0.000300	8186.740040	0.000051	Spitzer
b	573	8188.251350	0.000150	8188.251317	0.000050	Spitzer
b	579	8197.316440	0.000200	8197.316254	0.000051	Spitzer
b	583	8203.360000	0.000170	8203.359933	0.000039	Spitzer
b	627	8269.839058	0.000510	8269.838880	0.000062	SSO
b	651	8306.100460	0.000250	8306.100254	0.000060	UK
b	662	8322.720600	0.000300	8322.720446	0.000055	SSO
b	670	8334.807387	0.000260	8334.807537	0.000055	SSO
b	683	8354.447244	0.001100	8354.448790	0.000056	TS
b	707	8390.709366	0.000300	8390.710196	0.000056	SSO
b	713	8399.774630	0.000510	8399.775095	0.000055	SSO
b	744	8446.612133	0.000470	8446.612679	0.000056	SSO
b	746	8449.635474	0.000480	8449.634963	0.000063	SSO
b	905	8689.864390	0.000900	8689.865331	0.000082	TS
b	950	8757.855090	0.000190	8757.854996	0.000083	Spitzer
b	956	8766.920660	0.000180	8766.920573	0.000087	Spitzer

Planet	Epoch	t_{obs}	σ_{obs}	t_{post}	σ_{post}	Source
b	958	8769.941910	0.000160	8769.942063	0.000084	Spitzer
c	0	7282.805700	0.001400	7282.805840	0.000248	TS
c	21	7333.664000	0.000900	7333.664103	0.000204	TS
c	33	7362.726050	0.000380	7362.726968	0.000159	UK
c	35	7367.570510	0.000330	7367.570357	0.000165	TS + LT + VLT
c	42	7384.523200	0.001300	7384.523448	0.000144	TS
c	70	7452.334670	0.000150	7452.334607	0.000110	Spitzer
c	71	7454.756850	0.000520	7454.756909	0.000101	Spitzer
c	95	7512.880935	0.000910	7512.880552	0.000087	HST
c	109	7546.785870	0.000750	7546.785909	0.000081	TS
c	111	7551.628880	0.000660	7551.630320	0.000078	TS
c	123	7580.691370	0.000310	7580.691624	0.000079	LT
c	125	7585.535770	0.002500	7585.535454	0.000077	TN
c	126	7587.956298	0.000460	7587.957544	0.000076	TS + UK
c	131	7600.066840	0.000360	7600.066581	0.000075	UK
c	133	7604.909750	0.000630	7604.909767	0.000077	TS
c	135	7609.754610	0.000720	7609.753602	0.000076	TS
c	137	7614.597100	0.001300	7614.596743	0.000070	TS
c	142	7626.706100	0.001100	7626.705761	0.000069	TS
c	144	7631.550240	0.000560	7631.549963	0.000076	TS
c	147	7638.815180	0.000480	7638.814775	0.000069	TS
c	152	7650.923940	0.000230	7650.923801	0.000069	Spitzer
c	153	7653.345480	0.000160	7653.346042	0.000077	Spitzer
c	154	7655.768030	0.000400	7655.768151	0.000077	Spitzer
c	155	7658.189640	0.000230	7658.189726	0.000071	Spitzer
c	156	7660.611680	0.000510	7660.611560	0.000068	Spitzer
c	157	7663.033300	0.000370	7663.032819	0.000070	Spitzer
c	158	7665.455390	0.000310	7665.455100	0.000078	Spitzer
c	159	7667.877300	0.000190	7667.877244	0.000077	Spitzer
c	160	7670.298730	0.000210	7670.298705	0.000069	Spitzer
c	161	7672.719440	0.000810	7672.720519	0.000067	SSO
c	177	7711.467780	0.000640	7711.468903	0.000070	TN
c	182	7723.576630	0.000500	7723.577948	0.000070	TS
c	189	7740.533610	0.000875	7740.531326	0.000073	K2
c	190	7742.952761	0.001150	7742.952400	0.000065	K2
c	191	7745.374290	0.000630	7745.374191	0.000068	K2
c	192	7747.796988	0.000555	7747.795989	0.000067	K2
c	193	7750.217734	0.000960	7750.218290	0.000073	K2
c	194	7752.641660	0.000930	7752.640281	0.000071	K2
c	195	7755.058772	0.001650	7755.061330	0.000064	K2
c	196	7757.483127	0.000660	7757.483133	0.000067	K2
c	197	7759.902808	0.000580	7759.905033	0.000066	K2
c	198	7762.328060	0.000805	7762.327246	0.000070	K2
c	199	7764.748315	0.000720	7764.749218	0.000069	K2
c	200	7767.169944	0.001250	7767.170254	0.000063	K2
c	201	7769.592087	0.000815	7769.592110	0.000066	K2
c	202	7772.014828	0.001000	7772.014051	0.000064	K2
c	203	7774.434583	0.000810	7774.436196	0.000068	K2
c	204	7776.858148	0.001015	7776.858137	0.000067	K2
c	205	7779.279113	0.000885	7779.279205	0.000062	K2
c	206	7781.700947	0.000725	7781.701065	0.000064	K2
c	207	7784.123384	0.000540	7784.123071	0.000062	K2
c	210	7791.388008	0.000640	7791.388142	0.000060	K2
c	211	7793.811406	0.000790	7793.810034	0.000061	K2
c	212	7796.231528	0.000520	7796.232101	0.000061	K2
c	213	7798.653661	0.000825	7798.654056	0.000065	K2
c	214	7801.076314	0.000835	7801.075956	0.000065	K2
c	215	7803.497540	0.000180	7803.497079	0.000059	Spitzer + K2
c	216	7805.918840	0.000160	7805.919035	0.000059	Spitzer + K2
c	217	7808.341190	0.000280	7808.341112	0.000060	Spitzer + K2
c	218	7810.762720	0.000180	7810.762968	0.000064	Spitzer + K2

Planet	Epoch	t_{obs}	σ_{obs}	t_{post}	σ_{post}	Source
c	219	7813.184560	0.000320	7813.184840	0.000064	Spitzer + K2
c	220	7815.605850	0.000170	7815.606051	0.000057	Spitzer + K2
c	221	7818.028330	0.000300	7818.028016	0.000057	Spitzer
c	222	7820.450180	0.000180	7820.450120	0.000060	Spitzer
c	223	7822.871880	0.000240	7822.871864	0.000064	Spitzer
c	224	7825.293830	0.000340	7825.293742	0.000065	Spitzer
c	225	7827.715230	0.000190	7827.715004	0.000057	Spitzer
c	226	7830.137250	0.000240	7830.137014	0.000056	Spitzer
c	227	7832.558930	0.000150	7832.559125	0.000061	Spitzer
c	228	7834.981140	0.000200	7834.980766	0.000064	Spitzer
c	229	7837.402750	0.000350	7837.402615	0.000066	Spitzer
c	230	7839.824080	0.000260	7839.823965	0.000056	Spitzer
c	270	7936.696510	0.000350	7936.695869	0.000062	LT
c	284	7970.600440	0.000880	7970.600471	0.000065	LT
c	292	7989.975120	0.000260	7989.975217	0.000066	UK
c	294	7994.818400	0.000340	7994.818368	0.000062	SSO
c	298	8004.504880	0.000530	8004.505249	0.000062	LT
c	301	8011.771410	0.000270	8011.771162	0.000059	SSO + Spitzer
c	302	8014.192690	0.000230	8014.192941	0.000064	Spitzer
c	303	8016.613670	0.000680	8016.614191	0.000061	LT
c	304	8019.036353	0.000270	8019.036294	0.000060	Spitzer
c	305	8021.458460	0.000230	8021.458597	0.000059	Spitzer
c	306	8023.879670	0.000210	8023.880009	0.000058	Spitzer
c	309	8031.145170	0.000150	8031.145256	0.000060	Spitzer
c	310	8033.567520	0.000180	8033.567512	0.000059	SSO + Spitzer
c	311	8035.989110	0.000170	8035.988873	0.000058	Spitzer
c	312	8038.410640	0.000280	8038.410681	0.000061	Spitzer
c	313	8040.832460	0.000340	8040.832099	0.000060	Spitzer
c	314	8043.254040	0.000230	8043.254206	0.000060	Spitzer
c	315	8045.676640	0.000330	8045.676444	0.000059	SSO + Spitzer
c	319	8055.362970	0.000470	8055.363175	0.000061	LT
c	322	8062.627990	0.000370	8062.628430	0.000061	SSO
c	323	8065.047228	0.000710	8065.050039	0.000061	UK
c	329	8079.581300	0.000300	8079.581041	0.000066	LT + SSO + VLT
c	336	8096.533320	0.000300	8096.533092	0.000066	SSO
c	370	8178.874070	0.000150	8178.873958	0.000083	Spitzer
c	375	8190.982600	0.000240	8190.982800	0.000087	Spitzer
c	380	8203.091990	0.000220	8203.091664	0.000091	Spitzer
c	381	8205.512940	0.000250	8205.513134	0.000105	Spitzer
c	443	8355.664482	0.001200	8355.664306	0.000125	TS
c	462	8401.678529	0.000620	8401.678096	0.000130	SSO
c	469	8418.629477	0.000310	8418.630945	0.000123	SSO
c	581	8689.873860	0.000790	8689.873017	0.000106	TS
c	609	8757.683400	0.000190	8757.683356	0.000103	Spitzer
c	612	8764.949450	0.000240	8764.949511	0.000107	Spitzer
c	614	8769.792540	0.000190	8769.792413	0.000104	Spitzer
c	617	8777.058300	0.000210	8777.058543	0.000110	Spitzer
d	0	7560.797300	0.002300	7560.801847	0.000384	TS
d	16	7625.597790	0.000780	7625.595439	0.000258	WHT
d	20	7641.793600	0.002900	7641.793553	0.000233	TS
d	21	7645.843600	0.002100	7645.843203	0.000222	TS
d	23	7653.942690	0.000480	7653.942819	0.000213	Spitzer
d	24	7657.992000	0.000600	7657.992443	0.000204	Spitzer
d	25	7662.042600	0.000690	7662.042585	0.000201	Spitzer
d	26	7666.091830	0.000450	7666.091729	0.000198	Spitzer
d	27	7670.141940	0.000380	7670.141441	0.000190	Spitzer
d	41	7726.839750	0.000290	7726.839907	0.000153	HST
d	44	7738.991690	0.001600	7738.989634	0.000148	K2
d	45	7743.039535	0.001800	7743.039765	0.000145	K2
d	46	7747.089845	0.001450	7747.089898	0.000145	K2
d	47	7751.140219	0.001950	7751.140053	0.000143	K2

Planet	Epoch	t_{obs}	σ_{obs}	t_{post}	σ_{post}	Source
d	48	7755.188942	0.001550	7755.189994	0.000138	K2
d	49	7759.246376	0.002250	7759.239987	0.000138	K2
d	50	7763.288952	0.001500	7763.289994	0.000137	K2 + HST
d	51	7767.338659	0.001900	7767.339855	0.000131	K2
d	52	7771.390771	0.002600	7771.389833	0.000131	K2
d	53	7775.440259	0.001250	7775.440094	0.000129	K2
d	54	7779.488432	0.001900	7779.490241	0.000123	K2
d	55	7783.540232	0.002400	7783.540152	0.000124	K2
d	57	7791.640834	0.001350	7791.640492	0.000118	K2
d	60	7803.790810	0.000480	7803.790422	0.000116	Spitzer + K2
d	61	7807.840320	0.000300	7807.840285	0.000116	Spitzer + K2
d	62	7811.890980	0.000600	7811.890979	0.000119	Spitzer + K2
d	63	7815.940640	0.000300	7815.940945	0.000117	Spitzer + K2
d	64	7819.990500	0.000500	7819.990643	0.000119	Spitzer
d	65	7824.041690	0.000670	7824.041459	0.000124	Spitzer
d	66	7828.090800	0.000380	7828.091016	0.000125	Spitzer
d	67	7832.140430	0.000310	7832.140549	0.000126	Spitzer
d	68	7836.191710	0.000410	7836.191387	0.000134	Spitzer
d	99	7961.737740	0.001300	7961.736841	0.000189	SSO + TS
d	101	7969.836920	0.000700	7969.836583	0.000184	SSO
d	102	7973.885900	0.000660	7973.885485	0.000182	SSO
d	104	7981.987340	0.000850	7981.985545	0.000175	UK
d	105	7986.033802	0.000410	7986.034464	0.000173	UK
d	106	7990.084550	0.000510	7990.084189	0.000168	UK
d	112	8014.379400	0.000970	8014.381008	0.000154	Spitzer
d	113	8018.430710	0.000960	8018.431021	0.000152	LT
d	114	8022.480210	0.000410	8022.480092	0.000152	Spitzer
d	117	8034.628250	0.000420	8034.628207	0.000152	SSO + Spitzer
d	118	8038.679210	0.000310	8038.677588	0.000153	Spitzer
d	119	8042.726810	0.000450	8042.727135	0.000153	Spitzer
d	120	8046.776370	0.000360	8046.776574	0.000157	Spitzer
d	122	8054.875324	0.000330	8054.875654	0.000163	UK
d	154	8184.458010	0.000590	8184.457793	0.000351	Spitzer
d	157	8196.606510	0.000650	8196.606716	0.000360	Spitzer
d	160	8208.756470	0.000500	8208.755432	0.000363	Spitzer
d	180	8289.752463	0.004200	8289.750704	0.000358	SSO
d	185	8309.989670	0.002490	8309.999629	0.000371	UK
d	196	8354.551880	0.001100	8354.547658	0.000431	TS
d	201	8374.794521	0.000710	8374.794724	0.000458	SSO
e	0	7312.713000	0.002700	7312.713920	0.000360	TS
e	9	7367.596830	0.000370	7367.596769	0.000358	TS + LT + VLT
e	49	7611.576200	0.003100	7611.577312	0.000258	TN
e	51	7623.779500	0.001000	7623.779088	0.000251	TS
e	56	7654.278760	0.000440	7654.278196	0.000234	Spitzer
e	57	7660.380280	0.000300	7660.380132	0.000227	Spitzer
e	58	7666.480300	0.001800	7666.479313	0.000222	TS + LT
e	59	7672.579300	0.002600	7672.578247	0.000222	TS
e	67	7721.375140	0.000990	7721.375801	0.000180	TN
e	69	7733.573000	0.001400	7733.574143	0.000172	TS
e	70	7739.670847	0.001350	7739.672881	0.000166	K2
e	71	7745.771600	0.001200	7745.771213	0.000165	K2
e	72	7751.870070	0.000340	7751.870569	0.000159	HST
e	73	7757.967121	0.001600	7757.969761	0.000154	K2
e	74	7764.067000	0.002400	7764.067486	0.000153	K2 + HST
e	75	7770.171091	0.002150	7770.166928	0.000149	K2
e	76	7776.263782	0.001600	7776.265511	0.000145	K2
e	77	7782.362256	0.001750	7782.363740	0.000144	K2
e	79	7794.561592	0.001600	7794.561479	0.000139	K2
e	80	7800.663541	0.001700	7800.659036	0.000140	K2
e	81	7806.757840	0.000460	7806.757887	0.000139	Spitzer + K2
e	82	7812.857460	0.000510	7812.856472	0.000139	Spitzer + K2

Planet	Epoch	t_{obs}	σ_{obs}	t_{post}	σ_{post}	Source
e	83	7818.955100	0.000300	7818.954732	0.000139	Spitzer
e	84	7825.052970	0.000540	7825.052714	0.000140	Spitzer
e	85	7831.152070	0.000280	7831.152083	0.000140	Spitzer
e	86	7837.249690	0.000270	7837.249755	0.000142	Spitzer
e	102	7934.830780	0.000650	7934.830876	0.000154	SSO
e	103	7940.929360	0.000480	7940.930664	0.000154	SSO
e	110	7983.627720	0.000860	7983.630450	0.000140	SSO
e	111	7989.729440	0.000750	7989.729525	0.000138	SSO
e	112	7995.829390	0.000990	7995.829978	0.000136	SSO
e	114	8008.031300	0.000620	8008.030953	0.000132	UK
e	115	8014.130850	0.000200	8014.130929	0.000132	LT + Spitzer
e	116	8020.233200	0.000310	8020.233171	0.000129	Spitzer
e	118	8032.434050	0.001900	8032.433034	0.000128	LT
e	119	8038.535150	0.000330	8038.535031	0.000126	Spitzer
e	142	8178.847320	0.000190	8178.847405	0.000120	Spitzer
e	143	8184.948910	0.000340	8184.948686	0.000123	Spitzer
e	144	8191.048200	0.000510	8191.048074	0.000121	Spitzer
e	145	8197.146550	0.000330	8197.146617	0.000120	Spitzer
e	146	8203.247650	0.000260	8203.247613	0.000122	Spitzer
e	163	8306.926719	0.001200	8306.926045	0.000199	TS
e	164	8313.024650	0.000350	8313.024638	0.000205	UK
e	171	8355.711725	0.002600	8355.712925	0.000266	SSO
e	179	8404.501405	0.001000	8404.500746	0.000342	SSO
e	181	8416.701315	0.001500	8416.699204	0.000354	TN
e	188	8459.395405	0.002100	8459.393430	0.000426	TS
e	237	8758.281250	0.000530	8758.281389	0.000348	Spitzer
e	239	8770.478450	0.000360	8770.478748	0.000355	Spitzer
f	0	7321.525200	0.002000	7321.522338	0.000781	TS
f	5	7367.576290	0.000440	7367.577265	0.000694	TS + LT + VLT
f	34	7634.578090	0.000610	7634.578021	0.000235	TS + LT
f	36	7652.985790	0.000320	7652.985443	0.000217	Spitzer
f	37	7662.187430	0.000500	7662.187436	0.000216	Spitzer
f	38	7671.392680	0.000410	7671.392799	0.000213	Spitzer
f	43	7717.415410	0.000910	7717.412932	0.000221	TN
f	44	7726.619600	0.000260	7726.620534	0.000221	TS
f	46	7745.031155	0.001350	7745.028837	0.000220	K2
f	47	7754.233802	0.001550	7754.233126	0.000221	K2
f	48	7763.443380	0.000240	7763.443908	0.000212	K2 + HST
f	49	7772.647517	0.001600	7772.646770	0.000208	K2
f	50	7781.851416	0.001800	7781.853074	0.000208	K2
f	52	7800.273071	0.001400	7800.271911	0.000197	K2
f	53	7809.475450	0.000490	7809.475386	0.000197	Spitzer + K2
f	54	7818.682620	0.000290	7818.681966	0.000198	Spitzer
f	55	7827.886790	0.000300	7827.886768	0.000212	Spitzer
f	56	7837.103340	0.000470	7837.103831	0.000196	Spitzer
f	69	7956.805490	0.000540	7956.806676	0.000193	SSO + HST
f	70	7966.012617	0.000450	7966.012505	0.000187	UK
f	73	7993.634120	0.000840	7993.633462	0.000165	SSO
f	75	8012.041130	0.000470	8012.041272	0.000160	UK
f	76	8021.250850	0.000230	8021.251054	0.000157	Spitzer
f	78	8039.660140	0.000910	8039.659595	0.000152	SSO
f	79	8048.862350	0.000260	8048.862188	0.000150	UK
f	93	8177.715670	0.000260	8177.715327	0.000132	Spitzer
f	94	8186.918800	0.000240	8186.918823	0.000134	Spitzer
f	95	8196.125640	0.000250	8196.125737	0.000137	Spitzer
f	96	8205.327650	0.000290	8205.327767	0.000147	Spitzer
f	103	8269.777927	0.001000	8269.775969	0.000265	SSO
f	156	8757.762110	0.000270	8757.761780	0.000177	Spitzer
f	157	8766.968130	0.000230	8766.968069	0.000162	Spitzer
f	159	8785.389010	0.000220	8785.389208	0.000167	Spitzer
g	0	7294.786000	0.003900	7294.772215	0.000905	TS

Planet	Epoch	t_{obs}	σ_{obs}	t_{post}	σ_{post}	Source
σ	5	7356.534100	0.002000	7356.535119	0.000783	TS
σ	26	7615.924000	0.001700	7615.926795	0.000333	TS
σ	28	7640.637300	0.001000	7640.637735	0.000308	TS
σ	29	7652.994810	0.000300	7652.994362	0.000273	Spitzer
σ	30	7665.351340	0.000870	7665.351088	0.000249	Spitzer
σ	36	7739.484414	0.001150	7739.484959	0.000164	K2
σ	37	7751.839930	0.000170	7751.840023	0.000155	HST
σ	38	7764.190979	0.001550	7764.190852	0.000152	K2 + HST
σ	39	7776.548998	0.001095	7776.547566	0.000134	K2
σ	41	7801.250003	0.000925	7801.250178	0.000152	K2
σ	42	7813.606850	0.000270	7813.606484	0.000148	Spitzer + K2
σ	43	7825.961140	0.000200	7825.961396	0.000165	Spitzer
σ	44	7838.306590	0.000320	7838.306401	0.000188	Spitzer
σ	51	7924.769180	0.001400	7924.770157	0.000250	SSO
σ	54	7961.826210	0.000530	7961.825510	0.000235	SSO + TS
σ	57	7998.883242	0.000580	7998.883948	0.000203	UK
σ	58	8011.240140	0.000320	8011.240495	0.000203	Spitzer
σ	59	8023.590870	0.000230	8023.590652	0.000191	SSO + Spitzer
σ	60	8035.945510	0.000250	8035.945943	0.000180	Spitzer
σ	62	8060.655790	0.000470	8060.656134	0.000188	SSO
σ	65	8097.725110	0.000310	8097.724451	0.000199	UK
σ	72	8184.219050	0.000510	8184.218700	0.000158	Spitzer
σ	73	8196.572920	0.000310	8196.573216	0.000153	Spitzer
σ	74	8208.930360	0.000180	8208.930295	0.000150	Spitzer
σ	80	8283.052680	0.000930	8283.053541	0.000229	UK
σ	82	8307.754299	0.001400	8307.753666	0.000272	SSO
σ	90	8406.570377	0.000260	8406.569304	0.000334	SSO
σ	119	8764.827510	0.000320	8764.827523	0.000286	Spitzer
σ	120	8777.173950	0.000260	8777.174338	0.000312	Spitzer
h	0	7662.554360	0.002000	7662.550913	0.001498	Spitzer
h	5	7756.387400	0.001300	7756.384234	0.000845	K2
h	6	7775.153900	0.001600	7775.154903	0.000735	K2
h	7	7793.923000	0.002500	7793.923801	0.000644	K2
h	8	7812.698700	0.004500	7812.694932	0.000597	K2
h	9	7831.466140	0.000580	7831.465731	0.000575	Spitzer
h	16	7962.862710	0.000830	7962.863059	0.000504	SSO
h	17	7981.631470	0.001200	7981.632648	0.000472	LT + SSO
h	19	8019.168490	0.000860	8019.168285	0.000474	Spitzer
h	20	8037.932840	0.000850	8037.932396	0.000519	Spitzer
h	28	8188.050690	0.000530	8188.051154	0.000546	Spitzer
h	29	8206.819150	0.000670	8206.819966	0.000544	Spitzer
h	39	8394.513659	0.001400	8394.512234	0.001137	LT + SSO
h	59	8769.838090	0.000560	8769.837148	0.001176	Spitzer

Table B2: Observed transit times with uncertainties, along with the mean, t_{post} , and standard deviation, σ_{post} of the times from the posterior sample. Times are in $BJD - 2,450,000$ while uncertainties are in days.

Planet	Epoch	t_{post}	σ_{post}
b	1	7259.061221	0.000148
b	2	7260.572664	0.000161
b	3	7262.083454	0.000157
b	4	7263.594101	0.000148
b	5	7265.104975	0.000148
b	6	7266.615847	0.000149
b	7	7268.126699	0.000151
b	8	7269.637315	0.000144
b	9	7271.148093	0.000142
b	10	7272.659545	0.000155
b	11	7274.170346	0.000151
b	12	7275.680982	0.000142
b	13	7277.191801	0.000141
b	14	7278.702671	0.000142
b	15	7280.213582	0.000146
b	16	7281.724209	0.000139
b	17	7283.234973	0.000136
b	18	7284.746422	0.000148
b	19	7286.257236	0.000145
b	20	7287.767864	0.000136
b	21	7289.278633	0.000134
b	22	7290.789505	0.000135
b	23	7292.300473	0.000140
b	24	7293.811108	0.000134
b	25	7295.321860	0.000130
b	26	7296.833298	0.000142
b	27	7298.344127	0.000139
b	28	7299.854750	0.000130
b	29	7301.365472	0.000127
b	30	7302.876340	0.000128

Table B3: Mean, t_{post} , and standard deviation, σ_{post} of forecast times from the posterior sample. Times are in $JD - 2,450,000$ while uncertainties are in days. Thirty lines are previewed; full table is available electronically.

This paper has been typeset from a \TeX/L\AA\TeX file prepared by the author.